Lineage frequency time series reveal elevated levels of genetic drift in SARS-CoV-2 transmission in England

QinQin Yu[1,9,*], Joao Ascensao[2,‡], Takashi Okada[1,3,4,5,‡], The COVID-19 Genomics UK (COG-UK) consortium[6†], Olivia Boyd[7], Erik Volz[6,7], and Oskar Hallatschek[1,3,8,*]

[1]Department of Physics, University of California, Berkeley, California, United States
[2]Department of Bioengineering, University of California, Berkeley, California, United States
[3]Department of Integrative Biology, University of California, Berkeley, California, United States
[4]Institute for Life and Medical Sciences, Kyoto University, Kyoto, Japan
[5]RIKEN iTHEMS, Wako, Saitama, Japan
[6]https://www.cogconsortium.uk
[7]MRC Centre for Global Infectious Disease Analysis, Department of Infectious Disease Epidemiology, Imperial College London, London, United Kingdom
[8]Peter Debye Institute for Soft Matter Physics, Leipzig University, Leipzig, Germany
[9]Current address: Department of Immunology and Infectious Diseases, Harvard T.H. Chan School of Public Health, Boston, Massachusetts, United States
[‡]These authors contributed equally.
[†]See full list of consortium names and affiliations in the appendix
[*]Co-corresponding authors: qinqinyu@berkeley.edu, ohallats@berkeley.edu

January 13, 2024

Abstract

Genetic drift in infectious disease transmission results from randomness of transmission and host recovery or death. The strength of genetic drift for SARS-CoV-2 transmission is expected to be high due to high levels of superspreading, and this is expected to substantially impact disease epidemiology and evolution. However, we don't yet have an understanding of how genetic drift changes over time or across locations. Furthermore, noise that results from data collection can potentially confound estimates of genetic drift. To address this challenge, we develop and validate a method to jointly infer genetic drift and measurement noise from time-series lineage frequency data. Our method is highly scalable to increasingly large genomic datasets, which overcomes a limitation in commonly used phylogenetic methods. We apply this method to over 490,000 SARS-CoV-2 genomic sequences from England collected between March 2020 and December 2021 by the COVID-19 Genomics UK (COG-UK) consortium and separately infer the strength of genetic drift for pre-B.1.177, B.1.177, Alpha, and Delta. We find that even after correcting for measurement noise, the strength of genetic drift is consistently, throughout time, higher than that expected from the observed number of COVID-19 positive individuals in England by 1 to 3 orders of magnitude, which cannot be explained by literature values of superspreading. Our estimates of genetic drift will be informative for parameterizing evolutionary models and studying potential mechanisms for increased drift.

Author Summary

The transmission of pathogens like SARS-CoV-2 is strongly affected by chance effects in the contact process between infected and susceptible individuals, collectively referred to as random genetic drift. We have an incomplete understanding of how genetic drift changes across time and locations. To address this gap, we developed a computational method that infers the strength of genetic drift from time series genomic data that corrects for non-biological noise and is computationally scalable to the large numbers of sequences available for SARS-CoV-2, overcoming a major challenge of existing methods. Using this method, we quantified the strength of genetic drift for SARS-CoV-2 transmission in England throughout time and across locations. These estimates constrain potential mechanisms and help parameterize models of SARS-CoV-2 evolution. More generally, the computational scalability of our method will become more important as increasingly large genomic datasets become more common.

Introduction

Random genetic drift is the change in the composition of a population over time due to the randomness of birth and death processes. In pathogen transmission, births occur as a result of transmission of the pathogen between hosts and deaths occur as a result of infected host recovery or death. The strength of genetic drift in pathogen transmission is determined by the disease prevalence, the disease epidemiology parameters [1], the variance in offspring number (the number of secondary infections that result from an infected individual) [2], as well as host contact patterns [3]. Many diseases have been found to exhibit high levels of genetic drift, such as SARS, MERS, tuberculosis, and measles [2, 4, 5]. The strength of genetic drift affects how the disease spreads through the population [2, 3, 6] how new variants emerge [7, 8, 9, 10, 11], and the effectiveness of interventions [12], making it an important quantity to accurately estimate for understanding disease epidemiology, evolution, and control.

The effective population size is often used to quantify the strength of genetic drift; it is the population size in an idealized Wright-Fisher model (with discrete non-overlapping generations, a constant population size, and offspring determined by sampling with replacement from the previous generation) that would reproduce the observed dynamics [13]. In a neutral population, if the effective population size is lower than the true population size, it is an indication that there are additional sources of stochasticity beyond random sampling with replacement; thus, a lower effective population size indicates a higher level of genetic drift.

Transmission of SARS-CoV-2 has been shown to exhibit high levels of superspreading (high variance in offspring number) [14, 15, 16] and high levels of genetic drift (low effective population sizes) [17, 18, 19] (see also Supplementary table S1). However, studies have focused on particular times and locations, and we lack systematic studies over time and space (see Ref. [20] for a recent first study that uses contact tracing data

to infer changes in SARS-CoV-2 superspreading over time in Hong Kong). Performing a systematic study may be most feasible with a large-scale surveillance dataset, such as that from the COVID-19 Genomics UK (COG-UK) consortium, which has sequenced almost 3 million cases of SARS-CoV-2 in both surveillance and non-surveillance capacities as of October 5, 2022. We focus specifically on this dataset, and specifically on England, due to its consistently large number of sequenced SARS-CoV-2 cases since early in the pandemic.

A challenge to performing a systematic study of the strength of genetic drift for SARS-CoV-2 and other pathogens is how to handle measurement noise, or noise from the data collection process [21]. Measurement noise can arise from a variety of factors, including variability in the testing rate across time, geographic locations, demographic groups, and symptom status, and biases in contact tracing. Methods exist to infer measurement noise from time-series lineage or allele frequencies [22, 23, 24] (see the Supplementary information for a summary of other methods used for inferring genetic drift and additional references). Intuitively, in time-series frequency data, genetic drift leads to frequency fluctuations whose magnitudes scale with time, whereas measurement noise leads to frequency fluctuations whose magnitudes do not scale with time (Figure 1a). Thus, this system has been mapped onto a Hidden Markov Model (HMM) where the processes of genetic drift and measurement noise determine the transition and emission probabilities, respectively [25, 26]. Methods often assume uniform sampling of infected individuals from the population [27, 22, 23], but this assumption does not usually hold outside of surveillance studies. A recent study accounted for overdispersed sampling of sequences in the inference of fitness coefficients of SARS-CoV-2 variants, but assumes constant overdispersion over time [28]; in reality, the observation process may change over time due to changes in testing intensity between locations and subpopulations. Thus, to achieve the goal of systematically assessing the strength of genetic drift over time and space, there is a need to develop methods that account for time-varying overdispersed measurement noise to more accurately capture the noise generated from the observation process.

In this study, we develop a method to jointly infer genetic drift and measurement noise that allows measurement noise to be overdispersed (rather than uniform) and for the strength of overdispersion to vary over time (rather than stay constant). This method makes use of all sequencing data, which is difficult to do with existing phylogenetic methods. By fitting this model to observed lineage frequency trajectories from simulations, we show that the effective population size and the strength of measurement noise can be accurately determined in most situations, even when both quantities are varying over time. We then apply our validated method to estimate the strengths of genetic drift and measurement noise for SARS-CoV-2 in England across time (from March 2020 until December 2021) and space using over 490,000 SARS-CoV-2 genomic sequences from COG-UK. We find high levels of genetic drift for SARS-CoV-2 consistently throughout time that cannot be explained by literature values of superspreading. We discuss how community structure in the host contact network may partially explain these results. Additionally, we observe that sampling of infected individuals from the population is mostly uniform for this dataset, and we also find evidence of spatial structure in the transmission dynamics of B.1.177, Alpha, and Delta.

Results

Scalable method for jointly inferring genetic drift and measurement noise from time-series lineage frequency data

We first summarize the statistical inference method that we developed to infer time-varying effective population sizes from neutral lineage frequency time series that are affected by overdispersed measurement noise (more variable than uniform sampling). We explain the method more extensively in the Methods. We infer the effective population size that a well-mixed population would have to have to generate the magnitude of the fluctuations that are observed, which is the classical definition of effective population size [13]. Briefly, we use a Hidden Markov Model (HMM) with continuous hidden and observed states (a Kalman filter), where the hidden states are the true frequencies (f_t, where t is time), and the observed states are the observed frequencies (f_t^{obs}) (Figure 1b) (see Methods).

The transition probability between hidden states of the HMM is set by genetic drift, where the mean true frequency is the true frequency at the previous time $\mathrm{E}(f_{t+1}|f_t) = f_t$, and when the frequencies are rare the variance in frequency is proportional to the mean, $\mathrm{Var}(f_{t+1}|f_t) = \frac{f_t}{\tilde{N}_e(t)}$. $\tilde{N}_e(t) = N_e(t)\tau(t)$ where

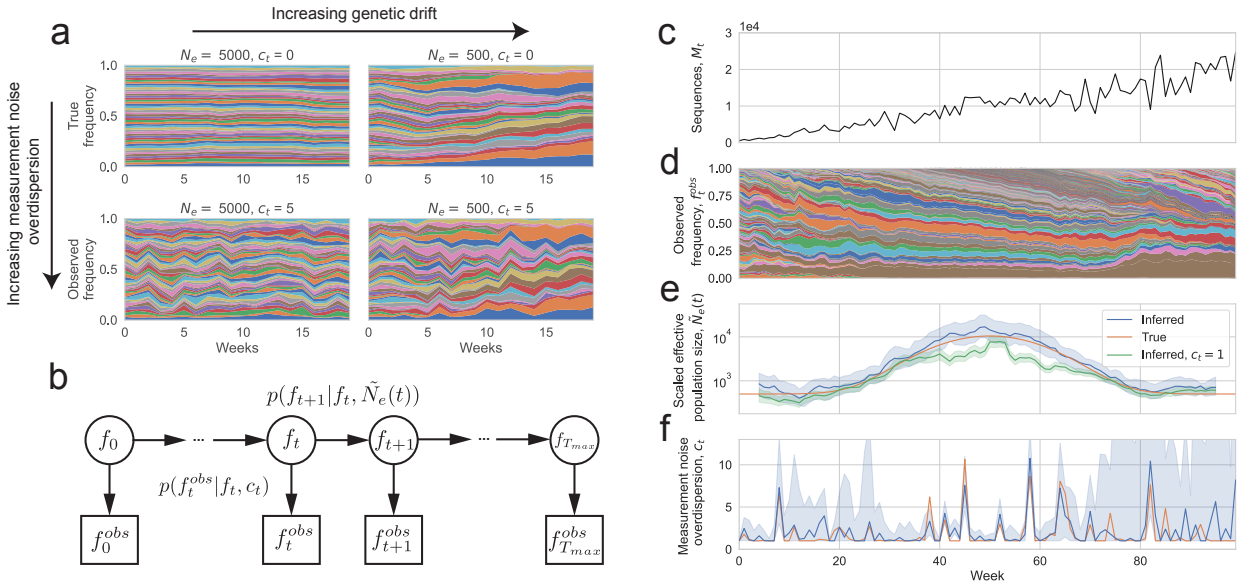

Figure 1: A Hidden Markov Model with continuous hidden and observed states (a Kalman filter) for inferring genetic drift and measurement noise from lineage frequency time series. (a) Illustration of how genetic drift and measurement noise affect the observed frequency time series. Muller plot of lineage frequencies from Wright-Fisher simulations with effective population size 500 and 5000, with and without measurement noise. In simulations with measurement noise, 100 sequences were sampled per week with the measurement noise overdispersion parameter $c_t = 5$ (parameter defined in text). All simulations were initialized with 50 lineages at equal frequency. A lower effective population size leads to larger frequency fluctuations whose variances add over time, whereas measurement noise leads to increased frequency fluctuations whose variances do not add over time. (b) Schematic of Hidden Markov Model describing frequency trajectories. f_t is the true frequency at time t (hidden states) and f_t^{obs} is the observed frequency at time t (observed states). The inferred parameters are $\tilde{N}_e(t) \equiv N_e(t)\tau(t)$, the effective population size scaled by the generation time, and c_t, the overdispersion in measurement noise ($c_t = 1$ corresponds to uniform sampling of sequences from the population). (c-f) Validation of method using Wright-Fisher simulations of frequency trajectories with time-varying effective population size and measurement noise. (c) Simulated number of sequences. (d) Simulated lineage frequency trajectories. (e) Inferred scaled effective population size ($\tilde{N}_e(t)$) on simulated data compared to true values. (f) Inferred measurement noise (c_t) on simulated data compared to true values. In (e) the shaded region shows the 95% confidence interval calculated using the posterior, and in (f) the shaded region shows the 95% confidence interval calculated using bootstrapping (see Methods).

$N_e(t)$ is the effective population size and $\tau(t)$ is the generation time, and both quantities can vary over time; however, we are only able to infer the compound parameter $N_e(t)\tau(t)$.

The emission probability between hidden and observed states of the HMM is set by measurement noise, where the mean observed frequency is the true frequency $\mathrm{E}(f_t^{obs}|f_t) = f_t$ and when the frequencies are rare the variance in the observed frequency is proportional to the mean, $\mathrm{Var}(f_t^{obs}|f_t) = c_t \frac{f_t}{M_t}$. M_t is the number of sequences at time t. c_t is the variance over the mean of the observed number of positive cases of each lineage at time t given the true number of cases of each lineage at time t (see Materials and Methods). c_t is expected to equal one if a random subsample of cases are sequenced, so that the observed number of cases of each lineage is approximately given by a Poisson distribution with the mean being the true number of cases of that lineage. In our analyses, we constrain $c_t \geq 1$ because realistically there must be at least Poisson sampling of cases for sequencing. Note that the constraint of $c_t \geq 1$ is still applicable when the number of sequenced cases is large as the variance already accounts for the number of sequences in the denominator. Our model assumes that the number of individuals and frequency of a lineage is high enough such that the central limit theorem applies (at least about 20 counts or frequency of 0.01); to meet this condition, we

created "coarse-grained lineages" where we randomly and exclusively grouped lineages together such that the sum of their abundances and frequencies was above this threshold (see Methods). Note that there are still sufficiently many coarse-grained lineages defined in the simulations and empirical analyses such that the assumption of the coarse-grained lineages being rare is true (needed for the defined transition and emission probabilities).

Using the transition and emission probability distributions (see Methods) and the HMM structure, we determine the likelihood function (Equation 13 in Methods) describing the probability of observing a particular set of lineage frequency time-series data given the unknown parameters, namely the scaled effective population size across time $\tilde{N}_e(t)$ and the strength of measurement noise across time c_t. We then maximize the likelihood over the parameters to determine the most likely parameters that describe the data. Because we are relying on a time-series signature in the data for the inference, we need to use a sufficiently large number of timesteps of data; on the other hand, the longer the time series, the more parameters would need to be inferred (since both $\tilde{N}_e(t)$ and c_t are allowed to change over time). To balance these two factors, we assumed that the effective population size stays constant over a time period of 9 weeks (a form of "regularization"). We then shift this window of 9 weeks across time to determine how $\tilde{N}_e(t)$ changes over time (see Methods), but this effectively averages the inferred $\tilde{N}_e(t)$ over time. c_t is still allowed to vary weekly.

To validate our model, we ran Wright-Fisher simulations with time-varying effective population size and time-varying measurement noise (Figure 1c-f). Because a substantial number of lineages would go extinct over the simulation timescale of 100 weeks, we introduced new lineages with a small rate (a rate of 0.01 per week per individual of starting a new lineage) to prevent the number of lineages from becoming too low. We then did inference on the simulated time-series frequency trajectories (Figure 1d). The inferred $\tilde{N}_e(t)$ and c_t closely follow the true values (Figure 1e-f), and the 95% confidence intervals (see Methods for how they are calculated) include the true value in a median (across timepoints) of 95% of simulation realizations (Figure S5). The error in c_t is higher when the variance contributed to the frequency trajectories by measurement noise is lower than that of genetic drift, which occurs when the effective population size is low or number of sequences is high (more clearly seen in Figure S6, where the effective population size is held constant). However, the error on $\tilde{N}_e(t)$ seems to be unchanged or even slightly decrease when the error on c_t is increased because the contribution to the variance due to genetic drift is higher. We also observe that the inferred $\tilde{N}_e(t)$ is smoothed over time due to the assumption of constant $\tilde{N}_e(t)$ over 9 weeks (Figure S7); this is a potential drawback when there are sharp changes in the effective population size over time. Importantly, we observed that the inferred $\tilde{N}_e(t)$ will be underestimated if sampling is assumed to be uniform when it is actually overdispersed (Figure 1e). This is because variance in the frequency trajectories due to measurement noise is incorrectly being attributed to genetic drift. The underestimation is strongest when the variance contributed due to measurement noise is high, either due to high measurement noise overdispersion, a low number of sampled sequences, or a high effective population size. In this situation, joint inference of measurement noise and $\tilde{N}_e(t)$ from the data is necessary for accurate inference of $\tilde{N}_e(t)$.

In summary, we developed a method to infer the strength of genetic drift and measurement noise from lineage frequency time series data and validated the accuracy of the method with simulations. This method has the potential to scale well with large amounts of genomic data as it only relies on lineage frequency time series data.

Inference of genetic drift in SARS-CoV-2 transmission in England

We next applied this method to study the effective population size and strength of measurement noise for SARS-CoV-2 in England, where hundreds of thousands of SARS-CoV-2 genomes have been sequenced. Because our method assumes that lineages are neutral with respect to one another (no selection), we performed separate analyses on groups of lineages that have been shown to exhibit fitness differences or deterministic changes in frequency: lineages pre-B.1.177, B.1.177, Alpha, and Delta [28, 17, 32, 33]. We checked that the assumption of neutrality within each of these groups does not significantly affect our results, and this is described below.

To obtain lineage frequency time series data for SARS-CoV-2 in England, we downloaded genomic metadata from the COVID-19 Genomics UK Consortium (COG-UK) [34] (Figure 2b) and the associated phylogenetic trees that were created at different points in time. To minimize potential bias, we used only surveillance data (labeled as "pillar 2"). For sequences pre-B.1.177, we used the pangolin lineages assign-

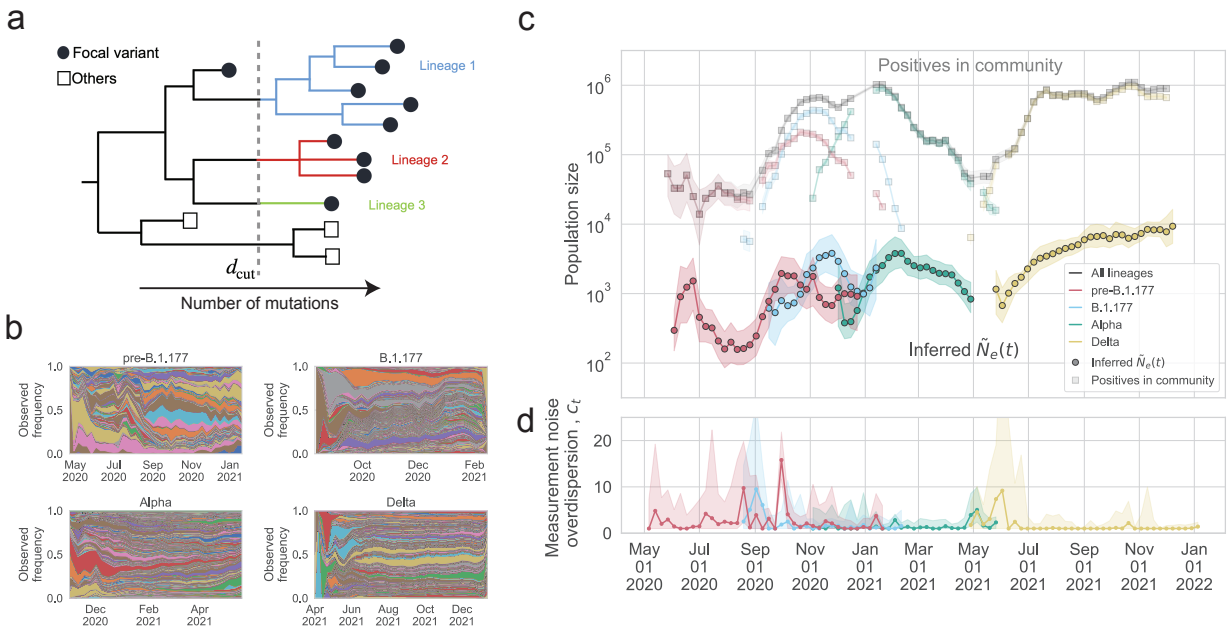

Figure 2: The inferred effective population size and overdispersion of measurement noise in England compared with the number of positive individuals. (a) Schematic of lineage construction for B.1.177, Alpha, and Delta from the COG-UK phylogenetic tree. The filled circles represent the sequences of a focal variant sampled in England, while the unfilled squares represent other sequences, which are of other variants or sampled in other countries. The phylogenetic tree is cut at a certain depth $d = d_{\text{cut}}$, and each branch cut by the line $d = d_{\text{cut}}$ defines a lineage. Lineages pre-B.1.1.7 are defined using the pango nomenclature [29, 30]. (b) Muller plot of lineage frequency time series for lineages pre-B.1.177, of B.1.177, of Alpha, of Delta. (c) Inferred scaled effective population size ($\tilde{N}_e(t) \equiv N_e(t)\tau(t)$) for pre-B.1.177 sequences, B.1.177, Alpha, and Delta, compared to the estimated number of people testing positive for SARS-CoV-2 in England at the community level, as measured by the COVID-19 Infection Survey [31], for all lineages and by variant or group of lineages. To simplify the plot, only data where the number of positive individuals for a given variant or group of lineages was higher than 10^3 in a week are shown. The inferred $\tilde{N}_e(t)$ is considerably lower than the number of positive individuals for all times and for all variants or group of lineages. (d) Inferred measurement noise overdispersion (c_t) for pre-B.1.177 sequences, B.1.177, Alpha, and Delta.

ments from COG-UK [29, 30]. However, B.1.177, Alpha, and Delta were subdivided into only one or a few pangolin lineages, since a new lineage is defined by sufficiently many mutations and evidence of geographic importation. However, for our purposes we only need resolution of neutral lineages within a variant. Thus, we created additional neutral lineages by cutting the phylogenetic tree at a particular depth and grouping sequences downstream of the branch together into a lineage (see Figure 2a and Methods). Note that as a result, the "lineages" that we define here are not necessarily the same as the lineages defined by the Pango nomenclature. The trees were created by COG-UK and most sequenced samples were included in the trees (Figure S8). However, in some instances downsampling was necessary when the number of sequences was very large. In these situations, any downsampling (performed by COG-UK) was done by trying to preserve genetic diversity. Most sequences in the tree were assigned to lineages (see Methods), and we corrected for the fraction of sequences that were not assigned to lineages in our inference of $\tilde{N}_e(t)$ (see Methods). This yielded 486 lineages for pre-B.1.177, 4083 lineages for B.1.177, 6225 lineages for Alpha, 24867 lineages for Delta.

The inferred scaled effective population size ($\tilde{N}_e = N_e\tau$, effective population size times generation time, where the generation time is the time between infections in infector-infectee pairs) is shown in Figure 2c. The generation time is around 4-6 days (0.6-0.9 weeks) depending on the variant [35, 36], but we leave the results

in terms of the scaled effective population size (rather than effective population size) because the generation time may change over time [35], has a high standard deviation [35], and is close to one week so is expected to not drastically change the result; additionally, as we show below, the null model estimate that we compare to is also multiplied by the generation time, which cancels when we look at the ratio (described below). The scaled inferred effective population size was lower than the number of positive individuals in the community (estimated by surveillance testing from the COVID-19 Infection Survey [31] and see Methods) by a factor of 20 to 1060 at different points in time. The most notable differences between the changes over time in the number of positives in the community and that of the scaled effective population size were: the inferred scaled effective population size of lineages pre-B.1.177 peaked slightly before the number of pre-B.1.177 positives peaked, the inferred scaled effective population size of Alpha decreased slower than the number of positives decreased after January 2021, and the shoulder for the inferred scaled effective population size of Delta occurred earlier than in the number of positives. We checked that the inferred scaled effective population size is not sensitive to the depth at which the trees are cut to create lineages (Figure S9, S10, S11), the threshold counts for creating coarse-grained lineages (Figure S12), or the number of weeks in the moving time window (Figure S13). Additionally, we checked that the gaussian form of the transition and emission probabilities in the HMM are a good fit to the data (Figure S14).

The inferred measurement noise for each group of lineages is shown in Figure 2d. The inferred measurement noise overdispersion was mostly indistinguishable from 1 (uniform sampling), but at times was above 1 (sampling that is more variable than uniform sampling). There were also at times differences in the strength of measurement noise between variants when they overlapped in time. In particular, measurement noise for lineages pre-B.1.177 peaked in October 2020 despite measurement noise being low for B.1.177 at that time.

To better interpret the observed levels of genetic drift, we compared the inferred $\tilde{N}_e(t)$ to that of an SIR null model, which includes a susceptible, infectious, and recovered class. The $\tilde{N}_e(t)$ for an SIR model was derived in Ref. [37, 38, 39] and is given by

$$\tilde{N_e}^{\mathrm{SIR}}(t) = \frac{I(t)}{2R_t\gamma_I} \tag{1}$$

where $I(t)$ is number of infectious individuals, R_t is the effective reproduction number, and γ_I is the rate at which infectious individuals recover. For the number of infectious individuals, we used the number of positive individuals estimated from the UK Office for National Statistics' COVID-19 Infection Survey [31], which is a household surveillance study that reports positive PCR tests, regardless of symptom status. We used the measured effective reproduction number in England reported by the UK Health Security Agency [40]. We used $\gamma_I^{-1} = 5.5$ days [41, 42], and our results are robust to varying γ_I within a realistic range of values (Figure S15). We found that $\tilde{N_e}^{\mathrm{SIR}}(t)$ is very similar to the number of positives because the effective reproduction number in England was very close to 1 across time and γ_I is also very close to 1 in units of weeks^{-1}. To calculate $\tilde{N_e}^{\mathrm{SIR}}(t)$ for each variant or group of lineages, we rescaled the population-level $I(t)$ and R_t based on the fraction of each variant in the population and the relative differences in reproduction numbers between variants (see Methods). We then calculated the scaled true population size, $\tilde{N}(t) \equiv N(t)\tau(t)$, for the SIR model by multiplying by the variance in offspring number, σ^2, for the SIR model [43]

$$\tilde{N}^{\mathrm{SIR}}(t) = \tilde{N_e}^{\mathrm{SIR}}(t)\{\sigma^2\}^{\mathrm{SIR}} \tag{2}$$

$$\{\sigma^2\}^{\mathrm{SIR}} = 2. \tag{3}$$

Overall, the inferred $\tilde{N}_e(t)$ is lower than $\tilde{N}^{\mathrm{SIR}}(t)$ by a time-dependent factor that varies between 20 and 590 (Figures 3c and S16), suggesting high levels of genetic drift in England across time. We find similar results when using an SEIR rather than an SIR model which additionally includes an exposed class and may be more realistic (Methods, Supplementary information, and Figure S17). The ratio of $\tilde{N}^{\mathrm{SIR}}(t)$ to the inferred $\tilde{N}_e(t)$ was similar across variants and across time, except that for Alpha the ratio initially peaked and then decreased over time.

Because non-neutral lineages could potentially bias the inferred effective population size to be lower in a model that assumes all lineages are neutral, we checked the assumption that lineages are neutral with respect to one another within a group or variant (pre-B.1.177, B.1.177, Alpha, and Delta) by detecting deterministic changes in lineage frequency. We used a conservative, deterministic method that ignores genetic drift, which

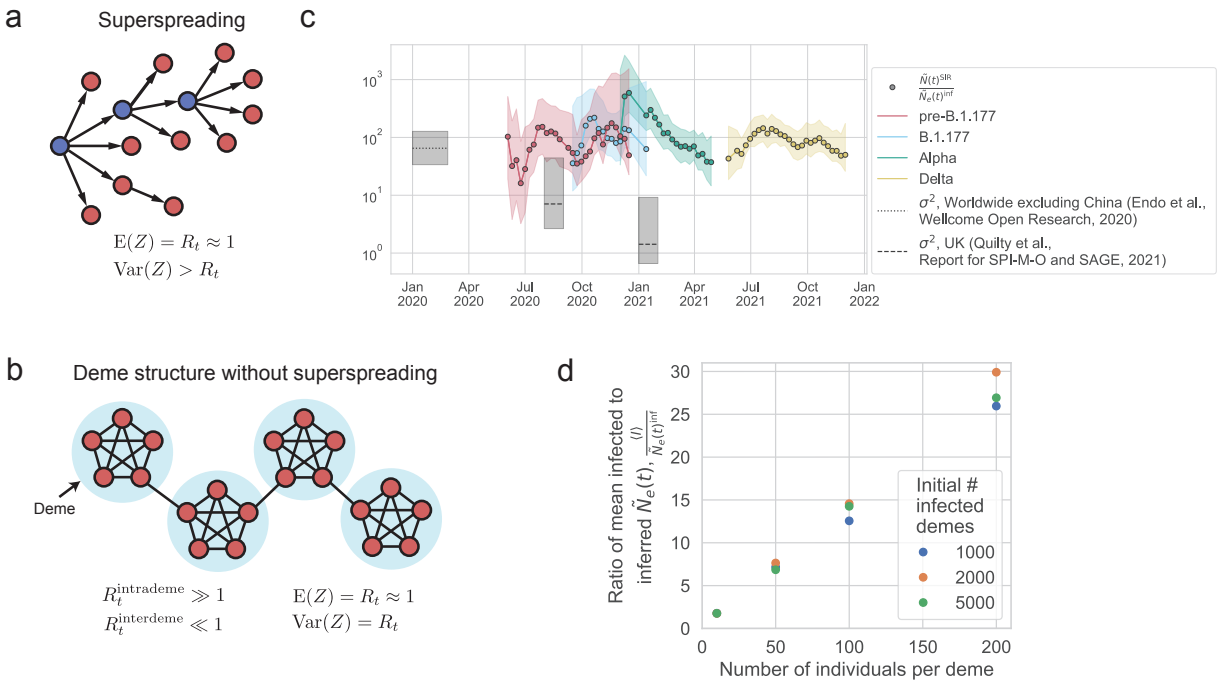

Figure 3: Potential mechanisms that can generate a low effective population size. (a) Superspreading, where the distribution of the number of secondary cases (Z) from a single infected individual is broadly distributed (variance greater than mean). The superspreading individuals are indicated in blue. (b) Deme structure without superspreading, due to heterogeneity in the host network structure, where the distribution of the number of secondary cases is not broadly distributed (variance approximately equal to mean). (c) The ratio between the $\tilde{N}^{\text{SIR}}(t)$ (the scaled population size calculated from an SIR model using the number of observed positive individuals and the observed effective reproduction number) and the inferred $\tilde{N}_e(t)$ for each variant. Only data where the error in the SIR model $\tilde{N}^{\text{SIR}}(t)$ is less than 3 times the value are shown, because larger error bars make it challenging to interpret the results. The inferred $\tilde{N}_e(t)$ is lower than the $\tilde{N}^{\text{SIR}}(t)$ (which assumes well-mixed dynamics and no superspreading) by a factor of 16 to 589, indicating high levels of genetic drift. The variance in offspring number from the literature [44, 45] does not entirely explain the discrepancy between the true and effective population sizes. (d) Simulations of deme structure without superspreading can generate high levels of genetic drift via jackpot events. SEIR dynamics are simulated within demes (with $R_t = 10$, i.e. deterministic transmission) and Poisson transmission is simulated between demes ($R_t \ll 1$, i.e. stochastic transmission) such that the population $R_t \sim 1$ (see Methods). Simulation parameters are: mean transition rate from exposed to infected $\gamma_E = (2.5 \text{ days})^{-1}$, mean transition rate from infected to recovered $\gamma_I = (6.5 \text{ days})^{-1}$, total number of demes $D_{total} = 5.6 \times 10^5$. The ratio between the number of infected individuals and the inferred effective population size is found to scale linearly with the deme size and not with the number of infected demes. This scaling results because of jackpot events where a lineage that happens to infect a susceptible deme grows rapidly until all susceptible individuals in the deme are infected.

is expected to overestimate the number of non-neutral lineages. We found that 50% of lineages had absolute fitness above 0.09 (above the 50th percentile) and 10% of lineages had absolute fitness above 0.27 (above the 90th percentile). Very likely, some of these lineages are detected as having non-zero fitness simply because the model does not correctly account for strong genetic drift which would also lead to changes in lineage frequency. Excluding non-neutral lineages with absolute fitness values above the 50th ($|s| > 0.09$), 75th ($|s| > 0.16$), and 90th ($|s| > 0.27$) percentiles, leads to only slight changes in the inferred effective population size (Figure S18). This result shows that conservatively excluding lineages that could be non-neutral does

not change the result that the inferred effective population size is one to two order of magnitudes lower than the SIR or SEIR model effective population size.

We also tested whether background selection (selection against deleterious mutants) in SARS-CoV-2 could be responsible for a substantial fraction of the reduction in effective population size. We simulated the lineage frequency dynamics using the empirically estimated distribution of deleterious fitness effects from Ref. [46] (Figure S19 and Methods) and found that the inferred effective population size is consistent with the true effective population size to within the error bars (Figure S20) and lower than the inferred effective population size in a simulation with only neutral mutations (Figure S21) by no more than a factor of 2 (Figure S22). Analytical estimates for the expected decrease in effective population size due to the empirical distribution of deleterious fitness effects also predict at most a factor of at most 2 decrease in effective population size that is not sufficient to explain the two orders of magnitude lower effective population size that we observe compared to the expectation (Supplementary Information).

We also probed the spatial structure of transmission by inferring the scaled effective population size separately for each region within England. We find that the scaled effective population size in the regions of England is substantially smaller than that in England as a whole for B.1.177, Alpha, and Delta (Figure S1), suggesting that the transmission was not well-mixed at that time. Additionally, the discrepancy between the inferred regional scaled effective population size and the observed number of positive individuals in a region was comparable to that seen in England as a whole (Figure S3), which is consistent with spatially segregated dynamics with similar levels of genetic drift in each region. We further describe these results in the Supplementary Information.

Discussion

Here, we systematically studied the strength of genetic drift of SARS-CoV-2 in England across time and spatial scales. To do this, we developed and validated a method for jointly inferring time-varying genetic drift and overdispersed measurement noise using lineage frequency time series data (Figure 1), allowing these two effects to be disentangled, which overcomes a major challenge in the ability to infer the strength of genetic drift from time-series data. Additionally, this method makes use of all sequencing data, overcoming the need to subsample data, which is a challenge with current phylogenetic methods. Our approach was able to reproduce the expected decrease in effective population size during the decline of pre-B.1.177, B.1.177, and Alpha, as well as the increase in effective population size during the emergence of B.1.177, Alpha, and Delta (Figure 2c). We did not have enough sequences during the time when Delta was going extinct to infer the effective population size during that time period.

We find that the effective population size of SARS-CoV-2 in England was lower than that of an SIR null model true population size (using the observed number of positives) by a time-dependent factor ranging from 20 to 590 (Figure 3c), suggesting that there were higher levels of genetic drift than expected from uniform transmission. We also find evidence for spatial structure in the transmission dynamics during the B.1.177, Alpha, and Delta waves, as the inferred $\tilde{N}_e(t)$ was substantially lower in regions compared to that of all England (Figure S1). These findings are consistent with other studies that have found spatial structure in transmission of B.1.177 [47], Alpha [48], and Delta [49].

We observed that with a few exceptions, the amount by which genetic drift was elevated compared to the number of positives did not change substantially over time or across variants outside the range of the error bars (Figure 3c), despite changes in lockdowns and restrictions (which we may expect to decrease behavior that leads to superspreading). This may be due to not having enough statistical power due to the dataset size. On the other hand, we note that restrictions affect the mobility network structure in a complex way, decreasing some types of mobility while increasing others [50], so lockdowns and restrictions may not affect the effective population size in a predictable way. One exception was that Alpha had significantly higher genetic drift compared to Delta and the strength of genetic drift in Alpha first peaked then slowly decreased over time. This may be either due to differences in the properties of the virus or differences in host behavior. For instance, it may suggest that the stochasticity in the transmission of Alpha sharply increased then slowly decreased over time. Alternatively, this may be driven by Alpha's expanding geographic range combined with reimported cases of Alpha into the UK (observed from February 2021 onwards), which could both also decrease the effective population size [51].

It is important to distinguish measurement noise from genetic drift as measurement noise is a function of the observation process and will not affect disease spread, extinction, and establishment of new mutations. We observe that measurement noise of SARS-CoV-2 is mostly indistinguishable from uniform sampling, but data from some variants at some times do exhibit more elevated measurement noise than uniform sampling. Thus, we expect that assuming uniform sampling, as many methods do, or constant overdispersion will lead to accurate estimates for this dataset [27, 22, 23, 28]. The number of SARS-CoV-2 sequences from England is extremely high and sampling biases are expected to be low, because of efforts to reduce sampling biases by sampling somewhat uniformly from the population through the COVID-19 Infection Survey [31] (from which a subset of positives are sequenced and included in the COG-UK surveillance sequencing data that we use). On the other hand, other countries may have higher sampling biases, so jointly estimating measurement noise and genetic drift may be more crucial in those settings. It may also be interesting to use this method to test whether genomics data taken from wastewater has lower levels of measurement noise as compared to sequenced cases.

We find that constant selection is unlikely to explain our results, as liberally excluding potentially non-neutral lineages does not significantly change the inferred effective population size. Our method is not able to precisely pinpoint how many lineages are under selection, but it appears that there is relatively little within-variant selection in the time period we investigated, and our method is robust to slight deviations from neutrality. Additionally, background selection is unlikely to explain our results as the empirically estimated distribution of deleterious fitness effects for SARS-CoV-2 decreased the effective population size by at most a factor of 2 from that of the completely neutral scenario.

Accurately estimating the strength of genetic drift allows us to better understand disease spread and extinction, as well as to better parameterize evolutionary models and understand how mutations will establish in the population. The establishment probability is the probability that a new mutation will rise to a high enough frequency to escape stochastic extinction. For weakly beneficial mutations, the establishment probability is linearly related to the effective population size [52]. For strongly beneficial mutations, the impact of the effective population size on the establishment probability is quantitatively less straightforward and depends on the host network structure [3]. In the absence of clonal interference, the fixation probability, or the probability that the mutation will fix in a population, is the same as the establishment probability; if there is clonal interference, the fixation probability will depend on additional factors like the mutation rate [53, 54]. The low effective population sizes that we observe suggest low establishment probabilities; the probability that any newly arisen beneficial mutant rises to a significant frequency will be small. More generally, our results give an order of magnitude estimate for the effective population sizes that can be used to more accurately parameterize evolutionary models for SARS-CoV-2 as well as an approach to infer the effective population size in more specific contexts.

Potential mechanisms that can contribute to the high levels of genetic drift

Two potential mechanisms that can contribute to the observed high levels of genetic drift are: (1) variability at the individual level through superspreading (Figure 3a), and (2) host population structure (Figure 3b). We investigate each of these mechanisms in turn and compare it to our results. While in reality, both mechanisms (and others not explored here) are likely at play, it is challenging to tease them apart given our limited data. Therefore, in order to gain intuition about how each of these phenomena drives the strength of genetic drift in this system, we consider each in turn.

Infected individuals that cause an exceptional numbers of secondary cases (superspreaders) are one reason for an increased level of allele frequency fluctuations. The expected decrease in effective population size is given by the per-generation variance in secondary cases, which is sensitive to superspreaders broadening the tail of the offspring distribution. Direct measurements of the offspring distribution through contact tracing yield variances substantially smaller than our inferred reduction in effective population size [55, 56, 57, 58] (Table S1). This could indicate that the tail of the offspring distribution is not well measured by contact tracing efforts or that other factors are at play that could decrease the effective population size.

Primary factors that could further increase fluctuations are selection and spatial structure. While both positive and background selection have some effect, we estimate their contribution to not exceed a factor of 2 (see above and Supplementary information). We now show that, by contrast, a pronounced host deme structure can easily decrease the effective population size by orders of magnitude, even without individual

super spreaders.

Consider a model in which individuals within a deme are very well-connected to one another (i.e. households or friend groups, also known as "communities" in network science [59]), but there are few connections between demes (Figure 3b). It is possible for deme structure to occur without superspreading. Because individuals are very well-connected within a deme, once the pathogen spreads to a susceptible deme, it will spread rapidly in a deme until all individuals are infected (a jackpot event). In this way, deme structure can lower the effective population size by lowering the effective number of stochastic transmissions events. For instance, in the example in Figure 3b, there are 20 individuals, but only 3 potential stochastic transmissions events. Deme structure may also arise from correlations in the number of secondary infections over a series of hosts (i.e. a series of high numbers of secondary infections in a transmission chain, or conversely low numbers of secondary infections in a transmission chain) [60]. This may arise, for instance, if individuals in a transmission chain have similar behavior, due to geographical proximity, or similar value systems on risk aversion. A recent study has found that individuals infected by superspreading tend to be superspreaders themselves more often than expected by chance [61], which would be consistent with this phenomenon.

To check our intuition that deme structure can decrease the effective population size and increase genetic drift, we ran simulations of a simplified deme model (see Methods): all demes have the same number of individuals, and there is a sufficiently large enough number of demes that the total number of demes does not matter. Initially a certain number of demes are infected, and transmission occurs such that the overall effective reproduction number in the population is around 1. From our simulations, we find that when the number of individuals in a deme increases, the ratio between the number of infected individuals and the inferred effective population size increases (Figure 3d); in other words, the more individuals there are in a deme, the higher the level of genetic drift we observe compared what is expected from the number of infected individuals. This is because while the number of infected individuals increases when the deme size increases (Figure S24a), the inferred effective population size (and thus the level of stochasticity) stays the same as a function of deme size (it is more dependent on the number of infected demes) (Figure S24b). However, the exact ratio of the number of infected individuals to the inferred effective size depends on the parameters of the model.

Studies that inferred the overdispersion parameter for the offspring number distribution using modeling rather than direct contact tracing and found a high variance in offspring number (see Table S1; for example, Ref. [44]) may actually be consistent with our results as the high variance may be partly due to superspreading events from, for example, host deme structure.

In reality, both superspreading and host structure are likely at play. Additionally, they could interact with each other. For instance, there could be superspreading within a deme. Future work can try to tease apart the contribution of these two mechanisms, which for instance may be possible with better transmission network data, building on previous work on transmission networks [62], or with time-resolved contact tracing data [20]. This will be important because the relative contributions of the two mechanisms of superspreading and host population structure to genetic drift can affect the establishment of new variants in the population in different ways [3]. If our interpretation is correct that deme structure and jackpot events strongly affect the effective population size, then managing superspreading events will be important to decrease the strength of genetic drift; nonpharmaceutical interventions should try to reduce these types of events.

Limitations of the study and opportunities for future directions

First, the quantity of effective population size is a summary statistic that is influenced by many factors, making its interpretation challenging. The effective population size describes the population size under a well-mixed Wright-Fisher model, whereas in reality, this assumption is broken by selection, migration, host structure, broad offspring number distributions, mutation, within-host evolution, and many other evolutionary and demographic processes. While many of these processes jointly contribute to the strength of genetic drift at the transmission level (broad offspring number distributions, host structure), which is what we are interested in inferring in this study, some other processes may confound the inference of genetic drift at the transmission level (selection, migration, within-host evolution, etc). While it would have been computationally intractable to jointly infer all possible processes, we addressed the processes that we thought were most likely to affect the effective population size in this system besides genetic drift at the transmission level.

We checked that constant selection could not lower the effective population size as much as we observed.

We did not test for more complex forms of selection, such as fluctuating selection, because including more complex forms of selection quickly increases the number of parameters in the model such that it becomes intractable. However, we note that fluctuating selection that occurs on a fast enough time scale will act effectively like genetic drift in increasing stochasticity in transmission. We ignored importation of SARS-CoV-2 into England and exportation of SARS-CoV-2 out of England. Migration can substantially change frequencies that are locally rare, but we expect importations to only weakly influence the frequency fluctuations of abundant variants, on which we have focused in this work. Host migration within the population can lead to gene flow; however, this will only affect the effective population size if it results in jackpot events [13]. Our model of host deme structure does indeed incorporate gene flow within the population with jackpot events, and we find that this type of host deme structure can substantially decrease the effective population size.

Empirically measured SARS-CoV-2 offspring distributions that take into account superspreaders (see references in Table S1) have been described by a negative binomial distribution, which has a finite mean and variance and thus can be described by the Wright-Fisher model. We focused on standing variation that existed at a particular depth in the phylogenetic tree and ignored de novo mutations subsequently arising during the time series. However, we don't think this should substantially affect our results because introducing mutations in the form of new lineages with a small rate in the simulations did not have a large effect on the method performance (Figure 1e). While within-host dynamics may in principle impact the lineage frequency trajectories, this effect is likely small for our analysis because we focus on acute infections (infections in the community rather than in hospitals and nursing homes). Acute infections of SARS-CoV-2 are thought to generate little within-host diversity that is passed on due to the short infection duration and small bottleneck size between hosts [63, 64]; while new mutations arising within acute hosts have been observed to be transmitted, these events are rare [63].

Thus, we think to the best of our knowledge that the low effective population sizes that we observe are due to increased levels of genetic drift at the transmission level, which can be due to a variety of mechanisms, including the two that we highlight above, superspreading and host deme structure. However, future work should explore joint inference of selection, migration, and/or mutation in the model, as is appropriate for the pathogen of interest, building on previous work in this area [65, 66, 26, 67].

Second, there may be biases in the way that data are collected that are not captured in our model. While our method does account for sampling biases that are uncorrelated in time, sampling biases that remain over time cannot be identified as such (i.e. if one geographical region was dominated by a particular lineage and it consistently had higher sequencing rates compared to another geographical region), and this can potentially bias the inferred effective population size; although, this is also a problem in phylogenetic methods. One approach to this problem that was utilized by some early methods during the pandemic is to develop sample weights based on geography, time, and number of reported cases. Future work should study the effect of different sampling intensities between regions on uncorrelated and correlated sampling noise. Additionally, we assume that the measurement noise overdispersion is identical for all lineages within a variant; in reality, there may be differences in sampling between lineages. However, we do not expect this to have a large effect on our results as we observed that measurement noise overdispersion was close to 1 for most timepoints in this dataset. Future work can test the effect of lineage-specific measurement noise overdispersion on overall method performance across different datasets.

Third, the use of a sliding window of 9 weeks on the lineage frequency data will lead to smoothing of sharp changes in effective population size. In our analysis, shortening the time window did not substantially affect our results. It may be interesting in future work to develop a continuous method that uses a prior to condition on changes in effective population size, similar to those that have been developed for coalescence-based methods [1, 68]. This would allow us to infer continuous changes in effective population size without needing to use a sliding window.

Fourth, we have defined lineages by cutting the phylogenetic tree at a particular depth; we chose this approach because a tree available for these sequences from COG-UK and we wanted to be somewhat consistent with the existing pango nomenclature for SARS-CoV-2 lineages, which were defined using a tree. One concern is that errors in the constructed tree may introduce additional fluctuations to the lineage frequencies. This may particularly be a problem for SARS-CoV-2 given the low mutation rate. As one check, we tested that cutting the tree at different depths did not affect the results (Figure S9), suggesting that our results were not sensitive to differences in lineage definitions at those depths. However, lineages defined using the two cut depths may both have errors in the groupings, so to be more robust, future work could systematically

investigate the sensitivity of our method to errors in the tree or compare the results using lineage frequencies and allele frequencies (defined using mutations). Recent advances have made building trees for large datasets more tractable [69], but we can potentially increase the scalability of our approach even further by making the method tree-free. For example, one idea is to cluster the sequences based on a distance metric and use cluster frequencies over time or another idea is to use allele frequencies (the frequencies of individual mutations). Future work should evaluate the feasibility and accuracy of using these different approaches to process the data for inferring the effective population size.

While we have focused on SARS-CoV-2 in this study, our simulations point to the generalizability of our approach, and the method developed here can be extended to study genetic drift in other natural populations that are influenced by measurement noise and where genomic frequency data are available. We think that this approach would be best suited for large datasets with a long period of sampling, and for pathogens this includes HIV, Ebola, and potentially seasonal influenza. It may also be interesting to adapt this approach to study data from field studies and ancient DNA [70, 71, 72]. More generally, ongoing methods development that integrates genomics, epidemiological, and other data sources is crucial for being able to harness the large amounts of data that have been generated to better understand and predict evolutionary dynamics.

Materials and Methods

Data sources and processing

We downloaded sequence data from the COVID-19 Genomics UK Consortium (COG-UK) [34]. We only used surveillance data (labeled as "pillar 2"); this dataset is composed of a random sample of the positive cases from the COVID-19 Infection Survey, which is a surveillance study of positive individuals in the community administered by the Office for National Statistics (see below). For lineages that appeared before B.1.177, we downloaded the metadata from the COG-UK Microreact dashboard [73], which included the time and location of sample collection (at the UTLA level), as well as the lineage designation using the Pango nomenclature [29, 30]. For B.1.177, Alpha, and Delta sequences, because the Pango nomenclature classified them into very few lineages, we created our own lineages from the phylogenetic trees (see below). We downloaded the publicly available COG-UK tree on February 22, 2021 for B.1.177; June 20, 2021 for Alpha; and January 25, 2022 for Delta. Additionally sensitively analyses shown in the Supplementary Figures used trees downloaded on June 1, 2021 for Alpha and March 25, 2022 for Delta. The publicly available trees were created by separating sequences into known clades, running fasttree [74] separately for each clade, grafting together the trees of different clades, and then using usher [69] to add missing samples (code available at `https://github.com/virus-evolution/phylopipe`). We also downloaded the COG-UK metadata for all lineages on January 16, 2022, which included the time and location (at the UTLA level) of sample collection. Additional sensitivity analyses shown in the Supplementary Figures used metadata downloaded on March 25, 2022. For the data of B.1.177, Alpha, and Delta, the data was deduplicated to remove reinfections in the same individual by the same lineage, but reinfections in the same individual by a different lineage were allowed. This yielded a total of 490,291 sequences.

The lineage frequency time-series is calculated separately for each variant or group of lineages (pre-B.1.177, B.1.177, Alpha, and Delta). First, the sequence metadata are aggregated by epidemiological week (Epiweek) to average out measurement noise that may arise due to variations in reporting within a week. Then, the lineage frequency is calculated by dividing the number of sequences from that lineage in the respective tree by the total number of sequences of that variant (or group of lineages) that were assigned to any lineage in the respective tree.

Because our model describes birth-death processes when the central limit theorem can be applied, we need the lineage frequencies to be sufficiently high. Thus, we randomly combine rare lineages into "coarse-grained lineages" that are above a threshold number of counts and threshold frequency in the first and last timepoint of each trajectory. The motivation of having a cutoff for both counts and frequency is to account for the fact that the total number of counts (number of sequences) varies over time. For the threshold, we chose 20 counts and frequency of 0.01. The motivation for combining lineages together randomly was to further remove any potential effects due to selection. We also tested that creating lineages by cutting the tree closer to the root of the tree did not substantially affect the results (Figure S9, S10); this shows that grouping lineages together based on genetic similarilty would not have had a substantial affect on our results. Sensitivity analyses showed that the choice of the coarse-grained lineage count threshold does not substantially affect the results (Figure S12). Coarse-grained lineages are non-overlapping (i.e. each sequence belongs to exactly one coarse-grained lineage).

The estimated number of people testing positive for COVID-19 in England and each region of England was downloaded from the UK Office for National Statistics' COVID-19 Infection Survey [31]. The COVID-19 Infection Survey includes households that are semi-randomly chosen, and individuals are tested regardless of whether they are reporting symptoms. Infections reported in hospitals, care homes, and other communal establishments are excluded. Thus the dataset provides a representative number of positive individuals in the community setting. The reported date of positive cases is the date that the sample was taken. The error on the number of positive individuals from April 17, 2020 to July 5, 2020 is reported as the 95% confidence interval, and after July 5, 2020 is reported as the 95% credible interval. The regional data reported the positivity rate over two week intervals. To get the number of positives, we multiplied by the number of individuals in the community setting in the region (excluding hospitals, care homes, and other communal establishments). As the data was reported over two week intervals, we obtained the number of positives for each week using linear interpolation.

The observed effective reproduction numbers for England and each region of England were downloaded

from the UK Health Security Agency [40]. Only times where the certainty criteria are met and the inference is not based on fewer days or lower quality data are kept. The error on the effective reproduction number is reported as the 90% confidence interval. Although not reported in the dataset, we choose the point estimate of the effective reproduction number to be the midpoint between the upper and lower bounds of the 90% confidence interval.

Creating lineages in B.1.177, Alpha, and Delta

For B.1.177, Alpha, and Delta, we divided each of them into neutral lineages based on phylogenetic distance. Specifically, for B.1.177 and Alpha, we cut a phylogenetic tree (in units of number of mutations from the root of the tree) at a certain depth, $d = d_{\text{cut}}$. Each of the internal or external branches that are cut by the line $d = d_{\text{cut}}$ defines a lineage (Figure 2a). The (observed) frequency of a lineage at a given time point in England was computed by counting the number of England sequences (leaf nodes) belonging to the lineage and by normalizing it by the total number of sequences in all assigned lineages of the focal variant in England at that time point. Lineage frequencies at the regional level were similarly computed by counting the number of sequences separately for each region.

The choice of d_{cut} is arbitrary to some extent. Because we wanted a sufficiently high resolution of lineages from the early phase of spreading of a variant and because the evolutionary distance correlates with the actual sample date (Figure S25), for each focal variant, we chose the depth d_{cut} that roughly corresponds to the time point when it began to spread over England.

For the Delta variant, the sequences form two distinct groups along the depth direction, as seen from the last panel of Figure S25. Therefore, to divide the Delta variant into lineages with small frequencies, we cut the phylogenetic tree at two depths sequentially; we first cut the tree at $d_{\text{cut}}^{(1)}$, which resulted in lineages with small frequencies plus a lineage with $\mathcal{O}(1)$ frequency. Then, to divide the latter lineage further, we took the subtree associated with this lineage and cut the subtree at $d_{\text{cut}}^{(2)}$.

For the results presented in the main text, we used (in units of substitutions per site, with the reference d=0 being the most recent common ancestor) $d_{\text{cut}} = 2.323 \cdot 10^{-2}$ for B.1.177, $d_{\text{cut}} = 2.054 \cdot 10^{-3}$ for Alpha, and $d_{\text{cut}}^{(1)} = 1.687 \cdot 10^{-3}$ and $d_{\text{cut}}^{(2)} = 1.954 \cdot 10^{-3}$ for Delta. We confirmed that our results are robust to the choice of d_{cut} as well as the choice of the phylogenetic tree data we used (Figure S9, S10, S11).

Model for inferring effective population size from lineage frequency time series

We use a Hidden Markov Model with continuous hidden and observed states to describe the processes of genetic drift and sampling of cases for sequencing (a Kalman filter) (Figure 1A). The hidden states describe the true frequencies of the lineages and the observed states describe the observed frequencies of the lineages as measured via sequenced cases. We adopt Gaussian approximations for the transmission and emission probabilities developed in [75] in order to get analytically tractable forms for the likelihood function, which will greatly speed up our computations.

The transition probability between the true frequencies f_t (the hidden states) due to genetic drift when $\frac{1}{\tilde{N}_e(t)} \ll f \ll 1$ has been shown in [75] to be well-described by the following expression, which we use as our transition probability,

$$p(f_{t+1}|f_t, \tilde{N}_e(t)) = \frac{1}{2}\sqrt{\frac{2f_t^{1/2}}{\pi f_{t+1}^{3/2}(\tilde{N}_e(t))^{-1}}}\exp\left(-\frac{2(\sqrt{f_{t+1}}-\sqrt{f_t})^2}{(\tilde{N}_e(t))^{-1}}\right). \tag{4}$$

$\tilde{N}_e(T) \equiv N_e(t)\tau(t)$ where $N_e(t)$ is the time-dependent effective population size and $\tau(t)$ is the time-dependent generation time, which is defined as the mean time between two subsequent infections per individual (i.e. the time between when an individual becomes infected and infects another individual, or the time between two subsequent infections caused by the same individual). This transition probability gives the correct first and second moments describing genetic drift when $f \ll 1$, $\mathrm{E}(f_{t+1}|f_t) = f_t$ and $\mathrm{Var}(f_{t+1}|f_t) = \frac{f_t}{\tilde{N}_e(t)}$, and is a good approximation when the central limit theorem can be applied, which is the case when $f \gg 0$. By assuming that $f_{t+1} \approx f_t$, and defining $\phi_t \equiv \sqrt{f_t}$, Equation 4 can be approximated as a simple normal

distribution

$$p(\phi_{t+1}|\phi_t, \tilde{N}_e(t)) = \mathcal{N}\Big(\phi_t, \frac{1}{4\tilde{N}_e(t)}\Big). \tag{5}$$

We describe the emission probability from the true frequency f_t to the observed frequency f_t^{obs} (the observed states), defining $\phi_t^{obs} \equiv \sqrt{f_t^{obs}}$, as

$$p(\phi_t^{obs}|\phi_t, c_t) = \mathcal{N}\Big(\phi_t, \frac{c_t}{4M_t}\Big) \tag{6}$$

where M_t is the number of input sequences. Again, this distribution is generically a good description when the number of counts is sufficiently large such that the central limit theorem applies (above approximately 20). The first and second moments of this emission probability are $\mathrm{E}(f_t^{obs}|f_t) = f_t$ and $\mathrm{Var}(f_t^{obs}|f_t) = \frac{c_t}{M_t} f_t$, or equivalently considering the number of sequences $n_t^{obs} = f_t^{obs} M_t$ and the true number of positive individuals n_t, $\mathrm{E}(n_t^{obs}|n_t) = n_t$ and $\mathrm{Var}(n_t^{obs}|n_t) = c_t n_t$. Thus, c_t describes the strength of measurement noise at time t. When $c_t = 1$, the emission probability approaches that describing uniform sampling of sequences from the population of positive individuals (i.e. can be described by a Poisson distribution in the limit of a large number of sequences), namely $\mathrm{Var}(n_t^{obs}|n_t) = n_t$ or equivalently $\mathrm{Var}(f_t^{obs}|f_t) = \frac{f_t}{M_t}$. This is the realistic minimum amount of measurement noise. When $c_t > 1$, it describes a situation where there is bias (that is uncorrelated in time) in the way that sequences are chosen from the positive population. The case of $0 < c_t < 1$ describes underdispersed measurement noise, or noise that is less random than uniform sampling. The case of $c_t = 0$ describes no measurement noise (for instance, when all cases are sampled for sequencing). These last two situations are unlikely in our data, and thus as we describe below, we constrain $c_t \geq 1$ in the inference procedure. In addition to being a good description of measurement noise, defining the emission probability in the same normal distribution form as the transmission probability allows us to easily derive an analytical likelihood function, described below (Note: see Ref. [26] for a method to derive an analytical likelihood function for arbitrary forms of the transition and emission probabilities).

We derive the likelihood function (up to a constant) for the Hidden Markov Model using the forward algorithm, although it can alternatively be derived by marginalizing over all hidden states. We assume an (improper) uniform prior on ϕ_0 (i.e. no information about the initial true frequency of the lineage).

$$p(\phi_0, \phi_0^{obs}, \theta_0) = p(\phi_0^{obs}|\phi_0, c_0)p(\phi_0) \tag{7}$$

$$p(\phi_0) \propto 1 \tag{8}$$

$$p(\phi_t, \phi_{0:t}^{obs}, \theta_{0:t}) = p(\phi_t^{obs}|\phi_t, c_t) \int_{-\infty}^{\infty} p(\phi_t|\phi_{t-1}, \tilde{N}_e(t)) p(\phi_{t-1}, \phi_{0:t-1}^{obs}, \theta_{0:t-1}) d\phi_{t-1}, \quad 0 < t \leq T \tag{9}$$

$$p(\phi_{0:T}^{obs}, \theta_{0:T}) = \int_{-\infty}^{\infty} p(\phi_T, \phi_{0:T}^{obs}, \theta_{0:T}) d\phi_T \tag{10}$$

$$\mathcal{L}(\vec{\phi}_{0:T}^{obs}|\theta_{0:T}) = \prod_{\alpha} p(\{\phi_{0:T}^{obs}\}_\alpha, \theta_{0:T}) p(\theta_{0:T}) \tag{11}$$

$$p(\theta_{0:T}) \propto 1 \tag{12}$$

$$\mathcal{L}(\vec{\phi}_{0:T}^{obs}|\theta_{0:T}) = \prod_{\alpha} p(\{\phi_{0:T}^{obs}\}_\alpha, \theta_{0:T}) \tag{13}$$

where $\phi_{0:t}^{obs} \equiv \{\phi_0^{obs}, ..., \phi_t^{obs}\}$, $\theta_{0:t} \equiv \{\tilde{N}_e(0), ..., \tilde{N}_e(t), c_0, ..., c_t\}$, and the subscript α indicates a particular lineage. We use a uniform prior on the parameters. The parameters $\theta_{0:T}$ are inferred by maximizing the likelihood (described below).

The forward algorithm has an analytical form for the simple case of Gaussian transition and emission probabilities. We use the identity for the product of two normal distributions $N(x, \mu, v)$, where μ is the mean and v is the variance:

$$N(x, \mu_1, v_1)N(x, \mu_2, v_2) = N(\mu_1, \mu_2, v_1 + v_2)N(x, \mu_{12}, v_{12}) \tag{14}$$

$$\mu_{12}(\mu_1, \mu_2, v_1, v_2) = \frac{\mu_1 v_2 + \mu_2 v_1}{v_1 + v_2} \tag{15}$$

$$v_{12}(v_1, v_2) = \frac{1}{\frac{1}{v_1} + \frac{1}{v_2}}. \tag{16}$$

Solving the forward algorithm recursively, we have

$$p(\phi_{0:T}^{obs}, \theta_{0:T}) = \prod_{i=1}^{T} N(\phi_i^{obs}, \mu_i, \frac{c_i}{4M_i} + v_i) \tag{17}$$

where

$$\mu_1 = \phi_0^{obs} \tag{18}$$

$$v_1 = \frac{\frac{1}{\tilde{N}_e(t)} + \frac{c_0}{M_0}}{4} \tag{19}$$

$$\mu_{i+1} = \mu_{12}(\mu_i, \phi_i^{obs}, v_i, \frac{c_i}{4M_i}) \tag{20}$$

$$v_{i+1} = v_{12}(\frac{c_i}{4M_i}, v_i) + \frac{1}{4\tilde{N}_e(t)}. \tag{21}$$

Equation 17 can be substituted into Equation 13 to obtain the full analytical likelihood function.

Fitting the model to data

We split the time series data into overlapping periods of 9 Epiweeks, over which the effective population size is assumed to be constant. We first use the moments of the probability distributions combined with least squares minimization to get an initial guess for the parameters. Then, we perform maximum likelihood estimation using the full likelihood function. To capture uncertainties that arise from the formation of coarse-grained lineages from lineages, we create coarse-grained lineages randomly 100 times (except where indicated otherwise). We infer the strength of measurement noise and the effective population size for each coarse-grained lineage combination (described below).

Determining the initial guess for the parameters using method of moments approach

Combining the transition and emission probabilities, and marginalizing over the hidden states we have

$$p(f_j^{obs}|f_i^{obs}) \propto \sqrt{\frac{1}{(f_j^{obs})^{3/2}}} \exp\left(- \frac{2\left(\sqrt{f_j^{obs}} - \sqrt{f_i^{obs}}\right)^2}{4\kappa_{i,j}} \right) \tag{22}$$

$$p(\phi_j^{obs}|\phi_i^{obs}) = \mathcal{N}(\phi_i^{obs}, \kappa_{i,j}) \tag{23}$$

$$\kappa_{i,j} \equiv \frac{c_i}{4M_i} + \frac{c_j}{4M_j} + \frac{(j-i)}{4\tilde{N}_e(t)}. \tag{24}$$

The first two terms of $\kappa_{i,j}$ are the contribution to the variance from measurement noise at times i ad j, and the third term is the contribution to the variance from genetic drift.

We calculate the maximum likelihood estimate of $\kappa_{i,j}$, $\hat{\kappa}_{i,j}$, which is simply the mean squared displacement

$$\hat{\kappa}_{i,j} = \left\langle (\phi_j^{obs} - \phi_i^{obs})^2 \right\rangle. \tag{25}$$

The standard error is given by

$$\Delta\hat{\kappa}_{i,j} = \sqrt{\frac{\left\langle \left[(\phi_j^{obs} - \phi_i^{obs})^2 - \hat{\kappa}_{i,j} \right]^2 \right\rangle}{Z}} \tag{26}$$

where Z is the number of coarse-grained lineages.

By looking across all pairs of timepoints i and j, we get a system of linear equations in $\kappa_{i,j}$ that depend on the parameters c_t and $\tilde{N}_e(t)$. To determine the most likely values of the parameters, we minimize

$$\ln \sum_{i,j} \frac{(\hat{\kappa}_{i,j} - \kappa_{i,j})^2}{\Delta\hat{\kappa}_{i,j}} \tag{27}$$

using scipy.optimize.minimize with the L-BFGS-B method and the bounds $1 \leq c_t \leq 100$ and $1 \leq \tilde{N}_e(t) \leq 10^7$. While underdispersed measurement noise ($c_t < 1$) is in principle possible, we constrain $c_t \geq 1$ because realistically, the lowest amount of measurement noise will be from uniform sampling of sequences. An example of inferred parameters using the methods of moments approach on simulated data is shown in Figure S26.

Maximum likelihood estimation of the parameters

For each set of coarse-grained lineages, we use the inferred measurement noise values (c_t) and inferred scaled effective population size from above ($\tilde{N}_e(t)$) as initial guesses in the maximization of the likelihood function in Equation 13 over the parameters. For the optimization, we use scipy.optimize.minimize_scalar with the Bounded method and the bounds $1 \leq c_t \leq 100$ and $1 \leq \tilde{N}_e(t) \leq 10^{11}$. The time t in the inferred $\tilde{N}_e(t)$ is taken to be the midpoint of the 9 Epiweek period. The reported $\tilde{N}_e(t)$ is the median inferred $\tilde{N}_e(t)$ across all coarse-grained lineage combinations where $\tilde{N}_e(t) < 10^5$ (values above 10^5 likely indicate non-convergence of the optimization, because most values above 10^5 are at 10^{11}, see Figure S27). The reported errors on $\tilde{N}_e(t)$ are the 95% confidence intervals (again taking the median across all coarse-grained lineage combinations where $\tilde{N}_e(t) < 10^5$) which are calculated by using the likelihood ratio to get a p-value [76, 77]. We replace the likelihood with the profile likelihood, which has the nuisance parameters $c_{0:T}$ profiled out:

$$p > 0.05 \tag{28}$$

$$p = \int I\left[\frac{\mathcal{L}_{\tilde{N}_e}(\hat{c}_{0:T}|\vec{\phi}^{obs}_{0:T})}{\mathcal{L}_{\tilde{N}'_e}(\hat{c}_{0:T}|\vec{\phi}^{obs}_{0:T})} > 1\right] P_{\tilde{N}'_e}(\hat{c}_{0:T}|\vec{\phi}^{obs}_{0:T}) d\tilde{N}'_e \tag{29}$$

$$\hat{c}_{0:T} = \arg\max_{c_{0:T}} \mathcal{L}_{\tilde{N}_e}(c_{0:T}|\vec{\phi}^{obs}_{0:T}) \tag{30}$$

$$P_{\tilde{N}'_e}(\hat{c}_{0:T}|\vec{\phi}^{obs}_{0:T}) \propto \mathcal{L}_{\tilde{N}'_e}(\hat{c}_{0:T}|\vec{\phi}^{obs}_{0:T}) p(\tilde{N}_e) \tag{31}$$

$$p(\tilde{N}_e) \propto 1 \tag{32}$$

where I is an indicator function that equals one when the argument is true and zero otherwise, $\mathcal{L}_{\tilde{N}_e}(\hat{c}_{0:T}|\vec{\phi}^{obs}_{0:T})$ is the profile likelihood with the nuisance parameters (in this case) $c_{0:T}$ profiled out, $P_{\tilde{N}'_e}(\hat{c}_{0:T}|\vec{\phi}^{obs}_{0:T})$ is the posterior where we have used a uniform prior. We also tried a Jeffreys prior which is used for variance parameters, but it gave similar results on simulated data because it looked relatively flat over the values of $\tilde{N}_e(t)$ of interest. As the Jeffreys prior was more computationally expensive than the uniform prior and the two priors gave similar results, we used the uniform prior for the analyses.

The reported values of c_t are the median across all coarse-grained lineage combinations and across all time series segments where the timepoint appears. The reported errors on c_t are the 95% confidence intervals as calculated by the middle 95% of values across coarse-grained lineage combinations and time series segments.

We checked that if we allow $c_t \geq 0$, the results are similar to if we constrain $c_t \geq 1$ (compare Figure 2 and S28).

An example of inferred parameters on simulated data using the maximum likelihood estimation approach, compared to the initial guesses of the parameters from the methods of moments approach, is shown in Figure S26.

Correcting for the number of sequences assigned to lineages

Because some sequences occur before the cut point in the tree that is used for creating lineages, they are not included in any lineages. As a result, the number of sequences assigned to lineages is lower than the number of sequences in the tree (Figure S29). This will bias the inferred $\tilde{N}_e(t)$ to be lower than in reality when the omitted sequences are from a particular part of the tree even when the dynamics are neutral (i.e. a certain part of the population is being left out of the analysis). To correct for the bias in inferred effective

population size that results from leaving out sequences from parts of the tree, we divide the inferred effective population size by the fraction of sequences in the tree that are assigned to a lineage. We note that while the number of sequences in the tree is less than the total number of sampled sequences, the sequences in the tree were chosen to be a representative fraction of the total sampled sequences. Thus, we do not need to additionally correct for the downsampling of sequences that were included in the tree. To test that randomly subsampling sequences for the analysis does not affect the results, we randomly subsampled half of the Delta sequences, and reran the analyses; the inferred effective population size was very similar to that from the full number of sequences (Figure S30).

Simulations for validating method

For the model validation, we perform simulations of the lineage trajectories using a discrete Wright-Fisher model. 500 lineages are seeded initially, and the initial frequency of lineages is taken to be the same across all lineages. In each subsequent Epiweek, the true number of counts for a lineage is drawn from a multinomial distribution where the probabilities of different outcomes are the true frequencies of the lineages in the previous Epiweek and the number of experiments is the effective population size. The true frequency is calculated by dividing the true number of counts by N. The observed counts are drawn from a negative binomial distribution,

$$p(n_t^{obs}|f_t) = NB(r,q) \equiv \binom{n_t^{obs}+r-1}{r-1} q^r (1-q)^{n_t^{obs}} \tag{33}$$

$$r = \frac{f_t M_t}{c_t - 1} \tag{34}$$

$$q = \frac{1}{c_t} \tag{35}$$

which has the same mean and variance as the emission probability in Equation 6. The total number of observed sequences in each timepoint is calculated empirically after the simulation is completed, as it may not be exactly M_t. The simulation is run for 10 weeks of "burn-in" time before recording to allow for equilibration. Coarse-grained lineages are created in the same way as described above.

For long time series simulations, some lineages will go extinct due to genetic drift, making it challenging to have sufficient data for the analysis. To be able to have a high enough number of lineages for the entire time series, we introduce mutations that lead to the formation of a new lineage with a small rate $\mu = 0.01$ per generation per individual.

Simulations for testing the effect of balancing selection

For the simulations that test for the effect of balancing selection, the simulations described above were modified as follows. Initially, each individual has a fitness drawn from the empirical distribution of deleterious fitness effects. Additionally, each individual forms a single lineage. To model selection, the probability of being drawn in the multinomial distribution is weighted by e^s, where s is the fitness coefficient. Mutations occur on the background of each individual in each generation with probability 0.01 and the mutants have a fitness that is the sum of that of the parent and a newly drawn fitness from the distribution of deleterious fitness effects. The burn-in period ends when the number of lineages reaches the threshold of 100 lineages, and recording begins. No new lineages are created in the simulation, so lineages are defined as the descendants of the individuals that are initially in the simulation.

Calculating the effective population size for an SIR or SEIR model

The effective population size times the generation time in an SIR model is given by Refs. [43, 37]

$$\tilde{N_e}^{\text{SIR}}(t) \equiv N_e^{\text{SIR}}(t)\tau(t) = \frac{I(t)}{2R_t\gamma_I}. \tag{36}$$

The variance in offspring number for an SIR model is approximately 2.

For an SEIR model, we calculated $\tilde{N}_e(t)$ following the framework from Ref. [38]. Using this framework, we were only able to consider a situation where the epidemic is in equilibrium. We test how well this approximates the situation out of equilibrium using simulations (see Supplementary Information).

We first considered how the mean number of lineages, A, changes going backwards in time, s, which is given by

$$\frac{dA}{ds} = -fp_c \tag{37}$$

where f is the number of transmissions per unit time and p_c is the probability that a transmission results in a coalescence being observed in our sample. p_c is given by the number of ways of choosing two lineages divided by the number of ways of choosing two infectious individuals

$$p_c = \frac{\binom{A(s)}{2}}{\binom{N(s)}{2}} \underset{\lim_{N(s)\to\infty}}{=} \binom{A(s)}{2} \frac{2}{N(s)^2}. \tag{38}$$

where the limit assumes that the number of infectious individuals, $N(s)$, is large. In the Kingman coalescent we also have

$$\frac{dA}{ds} = -\binom{A(s)}{2} \frac{1}{\tilde{N}_e(t)}. \tag{39}$$

Combining Equations 37, 38, and 39, we have

$$\tilde{N}_e(t) = \frac{N(s)^2}{2f}. \tag{40}$$

Thus by determining the number of transmissions per unit time, f, and the number of infectious individuals, $N(s)$, in an SEIR model, we can find an expression for $\tilde{N}_e(t)$.

These quantities can be derived from the equations describing the number of susceptible (S), exposed (E), infectious (I), and recovered (R) individuals in an SEIR model

$$\frac{dS}{dt} = -\beta I \frac{S}{N_H} \tag{41}$$

$$\frac{dE}{dt} = \frac{\beta I S}{N_H} - \gamma_E E - \delta_E E \tag{42}$$

$$\frac{dI}{dt} = \gamma_E E - \gamma_I I - \delta_I I \tag{43}$$

$$\frac{dR}{dt} = \gamma_I I \tag{44}$$

where β is the number of transmissions per infectious individual per unit time (the number of contacts made by an infectious individual per unit time multiplied by the probability that a contact results in a transmission), N_H is the total population size ($N_H = S + E + I + R$), γ_E is the rate that an exposed individual becomes infectious, δ_E is the rate of death for an exposed individual, γ_I is the rate than an infectious individual recovers, and δ_I is the rate of death for an infectious individual.

The number of infectious individuals in a generation, $N(s)$, is given by the instantaneous number of infectious individuals plus the number of exposed individuals that will become infectious in that generation [43]. Thus,

$$N(s) = \frac{\gamma_E}{\gamma_E + \delta_E} E + I. \tag{45}$$

The number of transmissions per unit time is given by

$$f = \beta I \frac{S}{N_H}. \tag{46}$$

We rewrite f in terms of the effective reproduction number (for which data are available) which is given by the number of transmissions per unit time (f) divided by the number of recoveries and deaths per unit time

$$R_t = \frac{f}{(\gamma_I + \delta_I)I + \delta_E E}. \tag{47}$$

Putting everything together, we have that $\tilde{N_e}(t)$ for an SEIR model in equilibrium is given by

$$\tilde{N_e}^{\text{SEIR,eq}}(t) = \frac{\left[\left(\frac{\gamma_E}{\gamma_E+\gamma_I}\right)E + I\right]^2}{2R_t[(\gamma_I+\delta_I)I + \delta_E E]}. \tag{48}$$

For SARS-CoV-2, the death rates are much lower than the rate at which exposed individuals become infectious and the rate at which infectious individuals recover ($\delta_E, \delta_I \ll \gamma_E, \gamma_I$). In this limit, Equation 48 simplifies to

$$\tilde{N_e}^{\text{SEIR,eq}}(t) = \frac{(E+I)^2}{2R_t\gamma_I I}. \tag{49}$$

To calculate the $\tilde{N_e}$ for an SIR or SEIR model, we use the estimated number of positives from the COVID-19 Infection Survey for $I(t)$. This number is an estimate of the number of positive individuals in the community as measured by surveillance and includes both symptomatic and asymptomatic individuals. While the estimated number of positives does not include cases from hospitals, care homes, and other communal establishments, community cases likely contribute the most to transmission. We used the measured effective reproduction number from the UK Health Security Agency for R_t.

To calculate the number of exposed individuals for the SEIR model, we solved for E in Equation 43 (taking $\delta_E \ll \gamma_E$)

$$E = \frac{1}{\gamma_E}\left(\frac{dI}{dt} + \gamma_I I\right). \tag{50}$$

$\frac{dI}{dt}$ was calculated numerically as $\frac{I(t+\Delta t)-I(t-\Delta t)}{2\Delta t}$ where $\Delta t = 1$ week. The parameter values used were γ_E^{-1} = 3 days and γ_I^{-1} = 5.5 days [41, 42]. We checked that varying the value used for γ_I does not substantially affect the results (Figure S15). The error on E was calculated by taking the minimum and maximum possible values from the combined error intervals of $I(t+\Delta t)$ and $I(t-\Delta t)$ (note that this does not correspond to a specific confidence interval size).

The error on $\tilde{N_e}(t)$ for the SIR or SEIR model was calculated similarly by taking the minimum and maximum possible values from the combined error intervals of E, I, and R_t. Only time points where the error interval of $\tilde{N_e}(t)$ was less than 3 times the point estimate were kept.

Calculating the effective population size for an SIR or SEIR model by variant

To calculate the effective population size for an SIR or SEIR model by variant, we needed to determine the variant-specific: number of infectious individuals $I(t)$, number of exposed individuals $E(t)$, effective reproduction number R_t, and rate than an infectious individual recovers γ_I. We assumed that γ_I is constant between variants. We calculated the number of infectious individuals $I(t)$ by multiplying the total number of positives by the fraction of each variant in the reported sequences. This should be a good representation of the fraction of the variant in the population as the sequences are a random sample of cases detected via surveillance. We calculated the number of variant-specific exposed individuals $E(t)$ in the same way as described above using the variant-specific number of infectious individuals. We assumed that the rate an exposed individual becomes infectious γ_E is constant between variants.

We calculated the variant-specific effective reproduction number by rescaling the measured effective reproduction number for the whole population

$$R_t^v = R_t \frac{R_0^v}{\sum_w R_0^w f^w} \tag{51}$$

where R_0^w is the basic reproduction number of the variant w and f^w is the fraction of the infectious population with variant w. The values of R_0 when rescaled to $R_0^{pre-B.1.177}$ that are used for the data presented in the main text are $\frac{R_0^{\text{pre-B.1.177}}}{R_0^{\text{pre-B.1.177}}} = \frac{R_0^{\text{B.1.117}}}{R_0^{\text{pre-B.1.177}}} = 1$, $\frac{R_0^{\text{Alpha}}}{R_0^{\text{pre-B.1.177}}} = 1.7$ (Ref. [17]), $\frac{R_0^{\text{Delta}}}{R_0^{\text{pre-B.1.177}}} = 1.97$ (Ref. [78]). We assumed the same R_0 for pre-B.1.177 and B.1.177 since the B.1.177 variant was shown to have increased in frequency due to importations from travel rather than increased transmissibility [47]. Varying the variant R_0 within the ranges reported in the literature does not substantially affect the results (Figure S31).

Inference of fitness from lineage frequency time series

We sought to infer the fitness effects of individual lineages, so that we could then determine if putatively selected lineages are influencing the estimation of the time-varying effective population sizes. We first used a deterministic method to estimate lineage fitness effects, similar to the method described in [79].

On average, when the frequency of lineage i is sufficiently small $f_{t,i} \ll 1$, the frequency dynamics will exponentially grow/decay according to the lineage fitness effect, s_i,

$$\langle f_{t,i} \rangle = f_{0,i} e^{s_i t}$$

The two sources of noise–genetic drift and measurement noise–both arise from counting processes, so the combined noise will follow $\mathrm{var}\left(f_{t,i}\right) \propto \langle f_{t,i} \rangle$. To account for the inherent discreteness of the number of cases in a lineage–especially important to accurately model lineages at low frequencies–we modeled the observed counts at Epiweek t of lineage i, $r_{t,i}$, as a negative binomial random variable,

$$r_{t,i} | s_i, f_{0,i} \sim \mathrm{NB}\left(\mu_{t,i}, \zeta_t\right) \tag{52}$$
$$\langle r_{t,i} \rangle = \mu_{t,i} \tag{53}$$
$$\mathrm{var}\left(r_{t,i}\right) = \zeta_t \langle r_{t,i} \rangle \tag{54}$$
$$\mu_{t,i} = M_t f_{0,i} e^{s_i t} \tag{55}$$

Where M_t is the total number of sequences, and ζ_t is a dispersion parameter. We took ζ_t as the total marginal variance at a given time-point, i.e. $\zeta_t = c_t + M_t / N_e(t)$, where we computed estimates of c_t and N_e as previously described (section "Maximum likelihood estimation of the parameters"). The final likelihood for the fitness, s_i, of lineage i is obtained by combining the data from all the relevant the time-points,

$$P(\boldsymbol{r}_i | s_i, f_{0,i}) = \prod_t \frac{\Gamma\left(r_{t,i} + \frac{\mu_{t,i}}{\zeta_t - 1}\right)}{\Gamma\left(\frac{\mu_{t,i}}{\zeta_t - 1}\right) \Gamma\left(r_{t,i} + 1\right)} \frac{(\zeta_t - 1)^{r_{t,i}}}{\zeta_t^{r_{t,i} + \frac{\mu_{t,i}}{\zeta_t - 1}}} \tag{56}$$

The point estimate of the lineage fitness, $\hat{s}_i$, is then numerically computed as the maximum likelihood,

$$\hat{s}_i = \underset{s_i}{\mathrm{argmax}} \log P(\boldsymbol{r}_i | s_i, f_{0,i}). \tag{57}$$

Stochastic simulations of SEIR model

The stochastic simulations of an SEIR model were performed using a Gillespie simulation with 4 states: susceptible, exposed, infectious, and recovered, where the number of individuals in each state are denoted by $S(t)$, $E(t)$, $I(t)$, and $R(t)$ respectively. There are 3 types of events that lead to the following changes in the number of individuals in each state

1. Infection of an susceptible individual with probability $\frac{\beta I(t) S(t)}{N(t)}$

$$S(t) = S(t) - 1 \tag{58}$$
$$E(t) = E(t) + 1 \tag{59}$$

2. Transition of an exposed individual to being infectious with probability $\gamma_E E(t)$

$$E(t) = E(t) - 1 \tag{60}$$
$$I(t) = I(t) + 1 \tag{61}$$

3. Recovery of an infectious individual with probability $\gamma_I I(t)$

$$I(t) = I(t) - 1 \tag{62}$$
$$R(t) = R(t) + 1 \tag{63}$$

where $\beta \equiv R_0\gamma_I$, R_0 is the basic reproduction number, γ_E is the rate that exposed individuals become infectious, and γ_I is the rate that infectious individuals recover. As in the rest of this work, we assume that the birth rate of susceptible individuals, background death rate, and the death rate due to disease are much slower compared to the rates of the above processes and thus can be neglected from the dynamics.

The time until the next event is drawn from an exponential distribution with rate given by the inverse of the sum of the above probabilities, and the type of event is randomly drawn weighted by the respective probabilities.

Because the time of the events occurs in continuous time, but the inference method of the effective population size works in discrete time, we must convert from continuous to discrete time. To perform this conversion, we calculate the net number of events of each type in each chosen unit of discrete time (1 week) and perform the changes in the number of individuals of each state as described above. Thus, for example, if within the same week an individual becomes exposed and then becomes infectious, it will cause the number of susceptible individuals to decrease by 1, no change in the number of exposed individuals, and the number of infectious individuals to increase by 1.

The infected (or infected and exposed) individuals are randomly assigned a lineage at a given time after the start of the epidemic. For our simulations, we chose the lineage labeling time as 75 days or 10.7 weeks since the approximate number of infectious individuals was high enough at that time to generate sufficient diversity in lineages, and we chose the number of different types of lineages as 100. The other parameters that we used for the simulations were $R_0 = 2$, $\gamma_E^{-1} = 3$ days, $\gamma_I^{-1} = 5.5$ days, $N(t) = S(t)+E(t)+I(t)+R(t) = 10^6$. The initial condition of the simulation is $S(t) = N(t) - 1$, $E(t) = 1$, and $I(t) = R(t) = 0$.

To test the sensitivity of the results to whether the reported PCR positive individuals are infectious or whether they can also be from the exposed class, we recorded the results in two ways. In the first case, only the infectious individuals we recorded as positive (Figure S32), and in the second case both the exposed and infectious individuals were recorded as positive (Figure S33). Inference of $\tilde{N}_e(t)$ was subsequently done on the lineage frequency trajectories of the recorded positive individuals. The SIR or SEIR model $\tilde{N}_e(t)$ were calculated analytically using the true numbers of infectious and exposed individuals and numerically using the number of positive individuals as described above in "Calculating the effective population size for an SIR or SEIR model".

Deme simulations

To better understand the effect of host population structure on the effective population size, we simulated a simple situation where there are "demes", or groups, of individuals with very high rates of transmission between individuals in that deme, but the rate of transmission between individuals from different demes is very low. In a given simulation, all demes have the same number of individuals (10, 50, 100, or 200). The total number of demes is chosen to be very high (5.6×10^6). Initially, a certain number of demes (100, 1000, 2000, or 5000) are each seeded by a single infectious individual infected by a randomly chosen lineage (200 different lineages). We simulated deterministic SEIR dynamics within demes with $R_0 = 10$, $\gamma_E = (2.5 \text{ days})^{-1}$, $\gamma_I = (6.5 \text{ days})^{-1}$. We simulated Poisson transmission dynamics between demes. In order to calibrate the overall population dynamics to be roughly in equilibrium (the number of infectious individuals is not deterministically growing or shrinking), we draw the number of between-deme infections caused by a given deme from a Poisson distribution with mean 1. The time of the between-deme infection event is randomly chosen, weighted by the number of infected individuals within a deme at a given time. The number of infectious individuals in each lineage is recorded every 1 week, and the frequency of the lineage is calculated by dividing by the total number of infectious individuals from all lineages in that week. The lineage frequency data from a period of 9 weeks starting in week 42 is used for the inference of effective population size. In this time period, only a small number of demes have been infected such that the total number of demes did not matter. The effective population size inference is performed as above except in the absence of measurement noise, so there is no emission step in the HMM.

Data and code availability

Data and code to reproduce the analyses in this manuscript are available at https://github.com/qinqin-yu/sars-cov-2_genetic_drift.

Acknowledgements

We are grateful to the Hallatschek lab for helpful discussions, feedback, and comments on earlier versions of this manuscript, particularly Giulio Issachini and Valentin Slepukhin. We are grateful to Aditya Prasad for advice on computing. We thank Mike Boots, Vince Buffalo, Katia Koelle, Priya Moorjani, Rasmus Nielsen, Daniel Reeves, and Daniel Weissman for helpful discussions and feedback. We thank Hernan G. Garcia and Yun S. Song for helpful comments on earlier versions of this manuscript. We are grateful to Daniel Weissman and two additional annonymous reviewers for generous feedback that greatly improved this manuscript. This material is based upon work supported by the National Science Foundation Graduate Research Fellowship under Grant No. DGE 1106400 (to QY), and JSPS KAKENHI (#22K03453, #JP22K06347, to TO). JAA acknowledges support from an NSF Graduate Research Fellowship and a Berkeley Fellowship. OH acknowledges support by a Humboldt Professorship of the Alexander von Humboldt Foundation. This research used resources of the National Energy Research Scientific Computing Center (NERSC), a U.S. Department of Energy Office of Science User Facility located at Lawrence Berkeley National Laboratory, operated under Contract No. DE-AC02-05CH11231 using NERSC BER-ERCAP0019907. COG-UK is supported by funding from the Medical Research Council (MRC) part of UK Research & Innovation (UKRI), the National Institute of Health Research (NIHR) [grant code: MC_PC_19027], and Genome Research Limited, operating as the Wellcome Sanger Institute. The authors acknowledge use of data generated through the COVID-19 Genomics Programme funded by the Department of Health and Social Care. The views expressed are those of the author and not necessarily those of the Department of Health and Social Care or UKHSA. We thank the COG-UK consortium and all partners and contributors who are listed at https://www.cogconsortium.uk/about/.

References

1. Volz EM and Didelot X. Modeling the growth and decline of pathogen effective population size provides insight into epidemic dynamics and drivers of antimicrobial resistance. Systematic Biology 2018; 67:719–28
2. Lloyd-Smith JO, Schreiber SJ, Kopp PE, and Getz WM. Superspreading and the effect of individual variation on disease emergence. Nature 2005; 438:355–9
3. Alexander H and Day T. Risk factors for the evolutionary emergence of pathogens. Journal of The Royal Society Interface 2010; 7:1455–74
4. Kucharski A and Althaus CL. The role of superspreading in Middle East respiratory syndrome coronavirus (MERS-CoV) transmission. Eurosurveillance 2015; 20:21167
5. Melsew YA, Gambhir M, Cheng AC, McBryde ES, Denholm JT, Tay EL, and Trauer JM. The role of super-spreading events in Mycobacterium tuberculosis transmission: evidence from contact tracing. BMC Infectious Diseases 2019; 19:1–9
6. Pastor-Satorras R, Castellano C, Van Mieghem P, and Vespignani A. Epidemic processes in complex networks. Reviews of Modern Physics 2015; 87:925
7. Otto SP, Day T, Arino J, Colijn C, Dushoff J, Li M, Mechai S, Van Domselaar G, Wu J, Earn DJ, et al. The origins and potential future of SARS-CoV-2 variants of concern in the evolving COVID-19 pandemic. Current Biology 2021; 31:R918–R929
8. Goyal A, Reeves DB, and Schiffer JT. Early super-spreader events are a likely determinant of novel SARS-CoV-2 variant predominance. medRxiv 2021
9. Day T, Gandon S, Lion S, and Otto SP. On the evolutionary epidemiology of SARS-CoV-2. Current Biology 2020; 30:R849–R857
10. Tasakis RN, Samaras G, Jamison A, Lee M, Paulus A, Whitehouse G, Verkoczy L, Papavasiliou FN, and Diaz M. SARS-CoV-2 variant evolution in the United States: High accumulation of viral mutations over time likely through serial Founder Events and mutational bursts. PloS ONE 2021; 16:e0255169
11. Ghafari M, Liu Q, Dhillon A, Katzourakis A, and Weissman DB. Investigating the evolutionary origins of the first three SARS-CoV-2 variants of concern. Frontiers in Virology 2022 :76

12. Sneppen K, Nielsen BF, Taylor RJ, and Simonsen L. Overdispersion in COVID-19 increases the effectiveness of limiting nonrepetitive contacts for transmission control. Proceedings of the National Academy of Sciences 2021; 118

13. Charlesworth B. Effective population size and patterns of molecular evolution and variation. Nature Reviews Genetics 2009; 10:195–205

14. Lakdawala SS and Menachery VD. Catch me if you can: superspreading of COVID-19. Trends in Microbiology 2021; 29:919–29

15. Althouse BM, Wenger EA, Miller JC, Scarpino SV, Allard A, Hébert-Dufresne L, and Hu H. Superspreading events in the transmission dynamics of SARS-CoV-2: Opportunities for interventions and control. PLoS Biology 2020; 18:e3000897

16. Goyal A, Reeves DB, Cardozo-Ojeda EF, Schiffer JT, and Mayer BT. Viral load and contact heterogeneity predict SARS-CoV-2 transmission and super-spreading events. eLife 2021; 10:e63537

17. Volz E, Mishra S, Chand M, Barrett JC, Johnson R, Geidelberg L, Hinsley WR, Laydon DJ, Dabrera G, O'Toole Á, et al. Assessing transmissibility of SARS-CoV-2 lineage B.1.1.7 in England. Nature 2021; 593:266–9

18. Ragonnet-Cronin M, Boyd O, Geidelberg L, Jorgensen D, Nascimento FF, Siveroni I, Johnson RA, Baguelin M, Cucunubá ZM, Jauneikaite E, et al. Genetic evidence for the association between COVID-19 epidemic severity and timing of non-pharmaceutical interventions. Nature Communications 2021; 12:1–7

19. Du Plessis L, McCrone JT, Zarebski AE, Hill V, Ruis C, Gutierrez B, Raghwani J, Ashworth J, Colquhoun R, Connor TR, et al. Establishment and lineage dynamics of the SARS-CoV-2 epidemic in the UK. Science 2021; 371:708–12

20. Adam D, Gostic K, Tsang T, Wu P, Lim WW, Yeung A, Wong J, Lau E, Du Z, Chen D, et al. Time-varying transmission heterogeneity of SARS and COVID-19 in Hong Kong (preprint). 2022

21. Frost SD, Pybus OG, Gog JR, Viboud C, Bonhoeffer S, and Bedford T. Eight challenges in phylodynamic inference. Epidemics 2015; 10:88–92

22. Bollback JP, York TL, and Nielsen R. Estimation of $2N_e s$ from temporal allele frequency data. Genetics 2008; 179:497–502

23. Buffalo V and Coop G. The linked selection signature of rapid adaptation in temporal genomic data. Genetics 2019; 213:1007–45

24. Levy SF, Blundell JR, Venkataram S, Petrov DA, Fisher DS, and Sherlock G. Quantitative evolutionary dynamics using high-resolution lineage tracking. Nature 2015; 519:181–6

25. Williamson EG and Slatkin M. Using maximum likelihood to estimate population size from temporal changes in allele frequencies. Genetics 1999; 152:755–61

26. Steinrücken M, Bhaskar A, and Song YS. A novel spectral method for inferring general diploid selection from time series genetic data. The Annals of Applied Statistics 2014; 8:2203

27. Stadler T. On incomplete sampling under birth–death models and connections to the sampling-based coalescent. Journal of Theoretical Biology 2009; 261:58–66

28. Dorp CHv, Goldberg EE, Hengartner N, Ke R, and Romero-Severson EO. Estimating the strength of selection for new SARS-CoV-2 variants. Nature Communications 2021; 12:1–13

29. O'Toole Á, Scher E, Underwood A, Jackson B, Hill V, McCrone JT, Colquhoun R, Ruis C, Abu-Dahab K, Taylor B, et al. Assignment of epidemiological lineages in an emerging pandemic using the pangolin tool. Virus Evolution 2021; 7:veab064

30. Rambaut A, Holmes EC, O'Toole Á, Hill V, McCrone JT, Ruis C, Plessis L du, and Pybus OG. A dynamic nomenclature proposal for SARS-CoV-2 lineages to assist genomic epidemiology. Nature microbiology 2020; 5:1403–7

31. UK Office for National Statistics. Coronavirus (COVID-19) Infection Survey: England. `https://www.ons.gov.uk/peoplepopulationandcommunity/healthandsocialcare/conditionsanddiseases/datasets/coronaviruscovid19infectionsurveydata`. Accessed: 2021-12-10

32. Challen R, Dyson L, Overton CE, Guzman-Rincon LM, Hill EM, Stage HB, Brooks-Pollock E, Pellis L, Scarabel F, Pascall DJ, et al. Early epidemiological signatures of novel SARS-CoV-2 variants: establishment of B.1.617.2 in England. medRxiv 2021

33. Davies NG, Abbott S, Barnard RC, Jarvis CI, Kucharski AJ, Munday JD, Pearson CA, Russell TW, Tully DC, Washburne AD, et al. Estimated transmissibility and impact of SARS-CoV-2 lineage B.1.1.7 in England. Science 2021; 372:eabg3055

34. The COVID-19 Genomics UK (COG-UK) consortium. An integrated national scale SARS-CoV-2 genomic surveillance network. The Lancet Microbe 2020; 1:e99

35. Hart WS, Abbott S, Endo A, Hellewell J, Miller E, Andrews N, Maini PK, Funk S, and Thompson RN. Inference of the SARS-CoV-2 generation time using UK household data. ELife 2022; 11:e70767

36. Hart WS, Miller E, Andrews NJ, Waight P, Maini PK, Funk S, and Thompson RN. Generation time of the alpha and delta SARS-CoV-2 variants: an epidemiological analysis. The Lancet Infectious Diseases 2022; 22:603–10

37. Volz EM, Kosakovsky Pond SL, Ward MJ, Leigh Brown AJ, and Frost SD. Phylodynamics of infectious disease epidemics. Genetics 2009; 183:1421–30

38. Frost SD and Volz EM. Viral phylodynamics and the search for an 'effective number of infections'. Philosophical Transactions of the Royal Society B: Biological Sciences 2010; 365:1879–90

39. Volz EM. Complex population dynamics and the coalescent under neutrality. Genetics 2012; 190:187–201

40. UK Health Security Agency. The R value and growth rate. `https://www.gov.uk/guidance/the-r-value-and-growth-rate#:~:text=The%20R%20range%20for%20the,as%20of%2019%20March%202021.&text=The%20R%20range%20for%20the,as%20of%2012%20March%202021.`. Accessed: 2021-12-10

41. Miller D, Martin MA, Harel N, Tirosh O, Kustin T, Meir M, Sorek N, Gefen-Halevi S, Amit S, Vorontsov O, et al. Full genome viral sequences inform patterns of SARS-CoV-2 spread into and within Israel. Nature Communications 2020; 11:1–10

42. He X, Lau EH, Wu P, Deng X, Wang J, Hao X, Lau YC, Wong JY, Guan Y, Tan X, et al. Temporal dynamics in viral shedding and transmissibility of COVID-19. Nature medicine 2020; 26:672–5

43. Koelle K and Rasmussen DA. Rates of coalescence for common epidemiological models at equilibrium. Journal of the Royal Society Interface 2012; 9:997–1007

44. Endo A et al. Estimating the overdispersion in COVID-19 transmission using outbreak sizes outside China. Wellcome Open Research 2020; 5

45. Quilty BJ, Chapman LA, Wong KL, Gimma A, Pickering S, JD S, Neil RPG, Jarvis CI, and Kucharski AJ. Reconstructing the secondary case distribution of SARS-CoV-2 from heterogeneity in viral load trajectories and social contacts. Report for SPI-M-O and SAGE 2021

46. Bloom JD and Neher RA. Fitness effects of mutations to SARS-CoV-2 proteins. bioRxiv 2023 :2023–1

47. Hodcroft EB, Zuber M, Nadeau S, Vaughan TG, Crawford KH, Althaus CL, Reichmuth ML, Bowen JE, Walls AC, Corti D, et al. Spread of a SARS-CoV-2 variant through Europe in the summer of 2020. Nature 2021; 595:707–12

48. Kraemer MU, Hill V, Ruis C, Dellicour S, Bajaj S, McCrone JT, Baele G, Parag KV, Battle AL, Gutierrez B, et al. Spatiotemporal invasion dynamics of SARS-CoV-2 lineage B.1.1.7 emergence. Science 2021; 373:889–95

49. McCrone JT, Hill V, Bajaj S, Pena RE, Lambert BC, Inward R, Bhatt S, Volz E, Ruis C, Dellicour S, et al. Context-specific emergence and growth of the SARS-CoV-2 Delta variant. Nature 2022; 610:154–60

50. Edsberg Møllgaard P, Lehmann S, and Alessandretti L. Understanding components of mobility during the COVID-19 pandemic. Philosophical Transactions of the Royal Society A 2022; 380:20210118

51. Wakeley J. Coalescent theory. Roberts & Company 2009

52. Kimura M. On the probability of fixation of mutant genes in a population. Genetics 1962; 47:713
53. Good BH, Rouzine IM, Balick DJ, Hallatschek O, and Desai MM. Distribution of fixed beneficial mutations and the rate of adaptation in asexual populations. Proceedings of the National Academy of Sciences 2012; 109:4950–5
54. Schiffels S, Szöllősi GJ, Mustonen V, and Lässig M. Emergent neutrality in adaptive asexual evolution. Genetics 2011; 189:1361–75
55. Laxminarayan R, Wahl B, Dudala SR, Gopal K, Mohan B C, Neelima S, Jawahar Reddy K, Radhakrishnan J, and Lewnard JA. Epidemiology and transmission dynamics of COVID-19 in two Indian states. Science 2020; 370:691–7
56. Adam DC, Wu P, Wong JY, Lau EH, Tsang TK, Cauchemez S, Leung GM, and Cowling BJ. Clustering and superspreading potential of SARS-CoV-2 infections in Hong Kong. Nature Medicine 2020; 26:1714–9
57. Sun K, Wang W, Gao L, Wang Y, Luo K, Ren L, Zhan Z, Chen X, Zhao S, Huang Y, et al. Transmission heterogeneities, kinetics, and controllability of SARS-CoV-2. Science 2021; 371:eabe2424
58. Bi Q, Wu Y, Mei S, Ye C, Zou X, Zhang Z, Liu X, Wei L, Truelove SA, Zhang T, et al. Epidemiology and transmission of COVID-19 in 391 cases and 1286 of their close contacts in Shenzhen, China: a retrospective cohort study. The Lancet Infectious Diseases 2020; 20:911–9
59. Obadia T, Silhol R, Opatowski L, Temime L, Legrand J, Thiébaut AC, Herrmann JL, Fleury E, Guillemot D, Boelle PY, et al. Detailed contact data and the dissemination of Staphylococcus aureus in hospitals. PLoS Computational Biology 2015; 11:e1004170
60. Steiner MC and Novembre J. Population genetic models for the spatial spread of adaptive variants: A review in light of SARS-CoV-2 evolution. PLoS Genetics 2022; 18
61. Taube JC, Miller PB, and Drake JM. An open-access database of infectious disease transmission trees to explore superspreader epidemiology. PLoS Biology 2022; 20:e3001685
62. Nande A, Adlam B, Sheen J, Levy MZ, and Hill AL. Dynamics of COVID-19 under social distancing measures are driven by transmission network structure. PLoS computational biology 2021; 17:e1008684
63. Lythgoe KA, Hall M, Ferretti L, Cesare M de, MacIntyre-Cockett G, Trebes A, Andersson M, Otecko N, Wise EL, Moore N, et al. SARS-CoV-2 within-host diversity and transmission. Science 2021; 372:eabg0821
64. Martin MA and Koelle K. Comment on "Genomic epidemiology of superspreading events in Austria reveals mutational dynamics and transmission properties of SARS-CoV-2". Science translational medicine 2021; 13:eabh1803
65. Feder AF, Kryazhimskiy S, and Plotkin JB. Identifying signatures of selection in genetic time series. Genetics 2014; 196:509–22
66. Mathieson I and McVean G. Estimating selection coefficients in spatially structured populations from time series data of allele frequencies. Genetics 2013; 193:973–84
67. Johri P, Aquadro CF, Beaumont M, Charlesworth B, Excoffier L, Eyre-Walker A, Keightley PD, Lynch M, McVean G, Payseur BA, et al. Recommendations for improving statistical inference in population genomics. PLoS biology 2022; 20:e3001669
68. Gill MS, Lemey P, Faria NR, Rambaut A, Shapiro B, and Suchard MA. Improving Bayesian population dynamics inference: a coalescent-based model for multiple loci. Molecular biology and evolution 2013; 30:713–24
69. Turakhia Y, Thornlow B, Hinrichs AS, De Maio N, Gozashti L, Lanfear R, Haussler D, and Corbett-Detig R. Ultrafast Sample placement on Existing tRees (UShER) enables real-time phylogenetics for the SARS-CoV-2 pandemic. Nature Genetics 2021; 53:809–16
70. Green RE, Krause J, Briggs AW, Maricic T, Stenzel U, Kircher M, Patterson N, Li H, Zhai W, Fritz MHY, et al. A draft sequence of the Neandertal genome. Science 2010; 328:710–22

71. Dehasque M, Ávila-Arcos MC, Díez-del-Molino D, Fumagalli M, Guschanski K, Lorenzen ED, Malaspinas AS, Marques-Bonet T, Martin MD, Murray GG, et al. Inference of natural selection from ancient DNA. Evolution Letters 2020; 4:94–108

72. Reich D, Green RE, Kircher M, Krause J, Patterson N, Durand EY, Viola B, Briggs AW, Stenzel U, Johnson PL, et al. Genetic history of an archaic hominin group from Denisova Cave in Siberia. Nature 2010; 468:1053–60

73. COG-UK and Microreact. UK SARS-CoV-2. `https://microreact.org/project/mxgBucHEZCZgsSWNrnQQRo-%20uk-sars-cov-2-2020-02-052021-04-20`. Accessed: 2021-04-20

74. Price MN, Dehal PS, and Arkin AP. FastTree 2-approximately maximum-likelihood trees for large alignments. PloS one 2010; 5:e9490

75. Ba ANN, Cvijović I, Echenique JIR, Lawrence KR, Rego-Costa A, Liu X, Levy SF, and Desai MM. High-resolution lineage tracking reveals travelling wave of adaptation in laboratory yeast. Nature 2019; 575:494–9

76. Aitkin M, Boys RJ, and Chadwick T. Bayesian point null hypothesis testing via the posterior likelihood ratio. Statistics and Computing 2005; 15:217–30

77. Smith I and Ferrari A. Equivalence between the posterior distribution of the likelihood ratio and a p-value in an invariant frame. Bayesian Analysis 2014; 9:939–62

78. Campbell F, Archer B, Laurenson-Schafer H, Jinnai Y, Konings F, Batra N, Pavlin B, Vandemaele K, Van Kerkhove MD, Jombart T, et al. Increased transmissibility and global spread of SARS-CoV-2 variants of concern as at June 2021. Eurosurveillance 2021; 26:2100509

79. Ascensao JA, Wetmore KM, Good BH, Arkin AP, and Hallatschek O. Quantifying the local adaptive landscape of a nascent bacterial community. Nature Communications 2023 14:1 2023 Jan; 14:1–19

80. Pybus OG, Rambaut A, and Harvey PH. An integrated framework for the inference of viral population history from reconstructed genealogies. Genetics 2000; 155:1429–37

81. Ho SY and Shapiro B. Skyline-plot methods for estimating demographic history from nucleotide sequences. Molecular Ecology Resources 2011; 11:423–34

82. Zinger T, Gelbart M, Miller D, Pennings PS, and Stern A. Inferring population genetics parameters of evolving viruses using time-series data. Virus Evolution 2019; 5:vez011

83. Ferrer-Admetlla A, Leuenberger C, Jensen JD, and Wegmann D. An approximate Markov model for the Wright–Fisher diffusion and its application to time series data. Genetics 2016; 203:831–46

84. Lumby CK, Zhao L, Breuer J, and Illingworth CJ. A large effective population size for established within-host influenza virus infection. eLife 2020; 9:e56915

85. Sobel Leonard A, Weissman DB, Greenbaum B, Ghedin E, and Koelle K. Transmission bottleneck size estimation from pathogen deep-sequencing data, with an application to human influenza A virus. Journal of Virology 2017; 91:e00171–17

86. Charlesworth B and Jensen JD. Effects of selection at linked sites on patterns of genetic variability. Annual review of ecology, evolution, and systematics 2021; 52:177–97

87. Nicolaisen LE and Desai MM. Distortions in genealogies due to purifying selection and recombination. Genetics 2013; 195:221–30

88. Dadonaite B, Crawford KH, Radford CE, Farrell AG, Timothy CY, Hannon WW, Zhou P, Andrabi R, Burton DR, Liu L, et al. A pseudovirus system enables deep mutational scanning of the full SARS-CoV-2 spike. Cell 2023; 186:1263–78

89. Starr TN, Greaney AJ, Stewart CM, Walls AC, Hannon WW, Veesler D, and Bloom JD. Deep mutational scans for ACE2 binding, RBD expression, and antibody escape in the SARS-CoV-2 Omicron BA. 1 and BA. 2 receptor-binding domains. PLoS pathogens 2022; 18:e1010951

90. Iketani S, Hong SJ, Sheng J, Bahari F, Culbertson B, Atanaki FF, Aditham AK, Kratz AF, Luck MI, Tian R, et al. Functional map of SARS-CoV-2 3CL protease reveals tolerant and immutable sites. Cell Host & Microbe 2022; 30:1354–62

1072 91. Flynn JM, Huang QYJ, Zvornicanin SN, Schneider-Nachum G, Shaqra AM, Yilmaz NK, Moquin SA,
1073 Dovala D, Schiffer CA, and Bolon DN. Systematic analyses of the resistance potential of drugs targeting
1074 SARS-CoV-2 main protease. ACS Infectious Diseases 2023; 9:1372–86

1075 92. Lau MS, Grenfell B, Thomas M, Bryan M, Nelson K, and Lopman B. Characterizing superspreading
1076 events and age-specific infectiousness of SARS-CoV-2 transmission in Georgia, USA. Proceedings of the
1077 National Academy of Sciences 2020; 117:22430–5

1078 93. Kirkegaard JB and Sneppen K. Variability of individual infectiousness derived from aggregate statistics
1079 of COVID-19. medRxiv 2021

1080 94. Riou J and Althaus CL. Pattern of early human-to-human transmission of Wuhan 2019 novel coron-
1081 avirus (2019-nCoV), December 2019 to January 2020. Eurosurveillance 2020; 25:2000058

Supplementary Information

Summary of existing methods for inferring the strength of genetic drift

There are currently four main types of methods for estimating the strength of genetic drift in pathogen transmission, which we summarize here for giving context to this study.

1. **Contact tracing** can directly measure superspreading by following the close contacts of infected individuals to measure the distribution of the number of secondary cases (the offspring number distribution) [2]. However, some secondary cases may be missed which can lead to measurement bias [20]. Additionally, it is challenging to trace multiple generations of transmission, so we miss important information on host contact network structure.

2. Another type of method fits disease prevalence over time to **branching process models** [44]. These models assume a particular distribution for the offspring number distribution (often a negative binomial distribution) and estimate the combination of parameters of the offspring number distribution along with growth rate that best fit the observed disease prevalence. External information about the growth rate can be used to constrain the parameters of the offspring number distribution.

3. **Phylogenetics** methods arrange genomics sequences into a tree based on genomic distance and either measure the distribution of lineage sizes (number of sequences in different parts of the tree) [19] or fit the rate at which branches in the tree coalescence to determine the effective population size [27, 80, 1, 81]. The effective population size is the population size that would reproduce the observed population dynamics under the idealized conditions of Wright-Fisher dynamics (discrete non- overlapping generations, a constant population size, and offspring determined by sampling with replacement from the previous generation). In neutral populations, a lower effective population size indicates a higher level of genetic drift.

4. **Time series frequency methods** make use of a signature that genetic drift leaves in time series data, which is that it causes fluctuations in the lineage abundances. Higher amounts of genetic drift (lower effective population size) lead to larger fluctuations, and the magnitude of the fluctuations can be fit to determine the effective population size [82, 24] (Figure 1a). Time series methods have also been used extensively in population genetics [22, 83, 65, 23, 26, 25] and to estimate within-host effective population size [84] and between-host transmission bottleneck sizes [85].

Comparison to SEIR null model

In the main text, we compared the inferred $\tilde{N}_e(t)$ to an SIR model. However, there are likely more complex epidemiological dynamics describing SARS-CoV-2. Here we check the results for an SEIR model which includes a susceptible, exposed, infectious, and recovered class. The SEIR model is a good representation of the epidemiology of SARS-CoV-2 when PCR test positivity is closely associated with an infected host being infectious; the literature suggests that this is a good assumption for SARS-CoV-2 [16], but we also test this assumption below. The exposed class thus represents individuals before they are infectious and test positive. $\tilde{N}_e(t)$ for an SEIR model in equilibrium (number of infectious individuals is constant over time) is given by (see Methods for derivation):

$$\tilde{N_e}^{\text{SEIR,eq}}(t) \equiv \{N_e(t)\tau(t)\}^{\text{SEIR,eq}} = \frac{(E(t)+I(t))^2}{2R_t\gamma_I(t)}. \tag{64}$$

where $E(t)$ is the number of exposed individuals, $I(t)$ is the number of infectious individuals, R_t is the effective reproduction number, and γ_I is the rate at which infectious individuals stop being infectious. While this equation is derived under equilibrium conditions, we show using simulations that this equation accurately estimates $\tilde{N}_e(t)$ in non-equilibrium conditions after the peak of the pandemic (Figure S32); before the pandemic peak, this equation overestimates $\tilde{N}_e(t)$ but by less than one order of magnitude. Additionally, we show that calculating the $\tilde{N}_e(t)$ using the equation for an SIR model (Equation 1) when the dynamics are actually described by an SEIR model provides a lower bound on the actual $\tilde{N}_e(t)$. Thus, if the true dynamics

of SARS-CoV-2 in England are actually SEIR dynamics, then the inference results shown in Figure 3c using the SIR model should be an underestimate of the level of genetic drift; thus our main result that the literature values of superspreading do not sufficiently explain our results should still hold.

In reality, it may also be the case that some people test positive in a PCR test before they become infectious. To test the impact of this possibility on our results, in our simulations we recorded both exposed and infectious individuals as testing positive. We then calculated the SEIR model $\tilde{N}_e(t)$ numerically as described in "Calculating the effective population size for an SIR or SEIR model" assuming that $I(t)$ includes both infectious and exposed individuals (Figure S33). We find that the numerical solutions give slightly higher $\tilde{N}_e(t)$ as compared with the true analytical solutions; however, the numerical solutions to the SEIR and SIR models bound the inferred $\tilde{N}_e(t)$. Thus we also expect that our main result that the literature values of superspreading do not sufficiently explain our results should still hold in this scenario.

To calculate the SEIR model $\tilde{N}_e(t)$ for the actual data, for the number of infectious individuals, we used the number of positive individuals estimated from the UK Office for National Statistics' COVID-19 Infection Survey [31], which is a household surveillance study that reports positive PCR tests, regardless of symptom status. We used the measured effective reproduction number in England reported by the UK Health Security Agency [40]. We found that $\tilde{N}_e{}^{\text{SEIR}}(t)$ is very similar to the number of positives because the effective reproduction number in England was very close to 1 across time. To calculate $\tilde{N}_e{}^{\text{SEIR}}(t)$ for each variant or group of lineages, we rescaled the population-level $I(t)$ and R_t based on the fraction of each variant in the population and the relative differences in reproduction numbers between variants (see Methods). We then calculated the scaled true population size, $\tilde{N}(t) \equiv N(t)\tau(t)$, for the SEIR model by multiplying by the variance in offspring number, σ^2, for the SEIR model [43]

$$\tilde{N}^{\text{SEIR}}(t) = \tilde{N}_e{}^{\text{SEIR}}(t)\{\sigma^2\}^{\text{SEIR}} \tag{65}$$

$$\{\sigma^2\}^{\text{SEIR}} = 2. \tag{66}$$

Overall, the inferred $\tilde{N}_e(t)$ is lower than $\tilde{N}^{\text{SEIR}}(t)$ by a time-dependent factor that varies between 70 and 2000 (Figure S17), suggesting high levels of genetic drift in England across time, which is consistent with what we find with an SIR model (Figures 2 and S16). Also similarly to in the case with an SIR model, the ratio of $\tilde{N}^{\text{SEIR}}(t)$ to the inferred $\tilde{N}_e(t)$ for Alpha decreased over time, suggesting that the stochasticity in the transmission of Alpha decreased over time.

The effect of background selection on effective population size

We estimated the magnitude by which we expect the effective population size to be decreased due to background selection given the empirically estimated distribution of fitness effects using both simulations (described in the main text) and analytical theory (described here). Most studies on background selection consider strongly deleterious mutations with a single negative fitness value and assume that deleterious mutants quickly die out so that multiple mutations do not occur in the same background [86]. However, in this case we need to consider a distribution of fitness effects and the possibility of mutants with different fitnesses existing simultaneously. As such, we used Equation 8 derived from Ref. [87] for the effective population size in the presence of deleterious mutations with a distribution of fitness effects, assuming a constant mutation rate and no recombination

$$N_e \approx N\text{exp}\Big[-\int_{\frac{1}{N}}^{\infty}\frac{\mu}{s}(1-e^{-st})^2\rho(s)ds\Big] \tag{67}$$

where μ is the deleterious mutation rate per generation per genome, $\rho(s)$ is the deleterious distribution of fitness effects (i.e. the fitness effect is $-s$), t is time in generations into the past, and N is the census population size. Assuming no recombination is a conservative assumption, as recombination mitigates the effects of background selection [86].

Using the empirically estimated distribution of fitness effects from Ref. [46] (which are consistent with experimental measurements, see Refs. [88, 89, 90, 91]) and the clock rate of 31 substitutions per year (Nextstrain SARS-CoV-2 GISAID build on August 7, 2023), a generation time of 5.1 days [35], and a population size of 10^4 (order of magnitude of true population size), we estimate that the effective population

size will be decreased by at most a factor of 2 at times far into the past, and less in more recent times (see Figure S34). The above formula was derived assuming strong selection ($s \gg \frac{1}{N}$) for the bulk of deleterious mutations, which we see from the distribution of fitness effects does hold (Figure S19). Thus, while background selection will in general decrease the effective population size, in this system it can only explain a small fraction of the observed reduction of two orders of magnitude. This result is consistent with what we found in the simulations (Figure S22).

Application to COG-UK data by regions in England

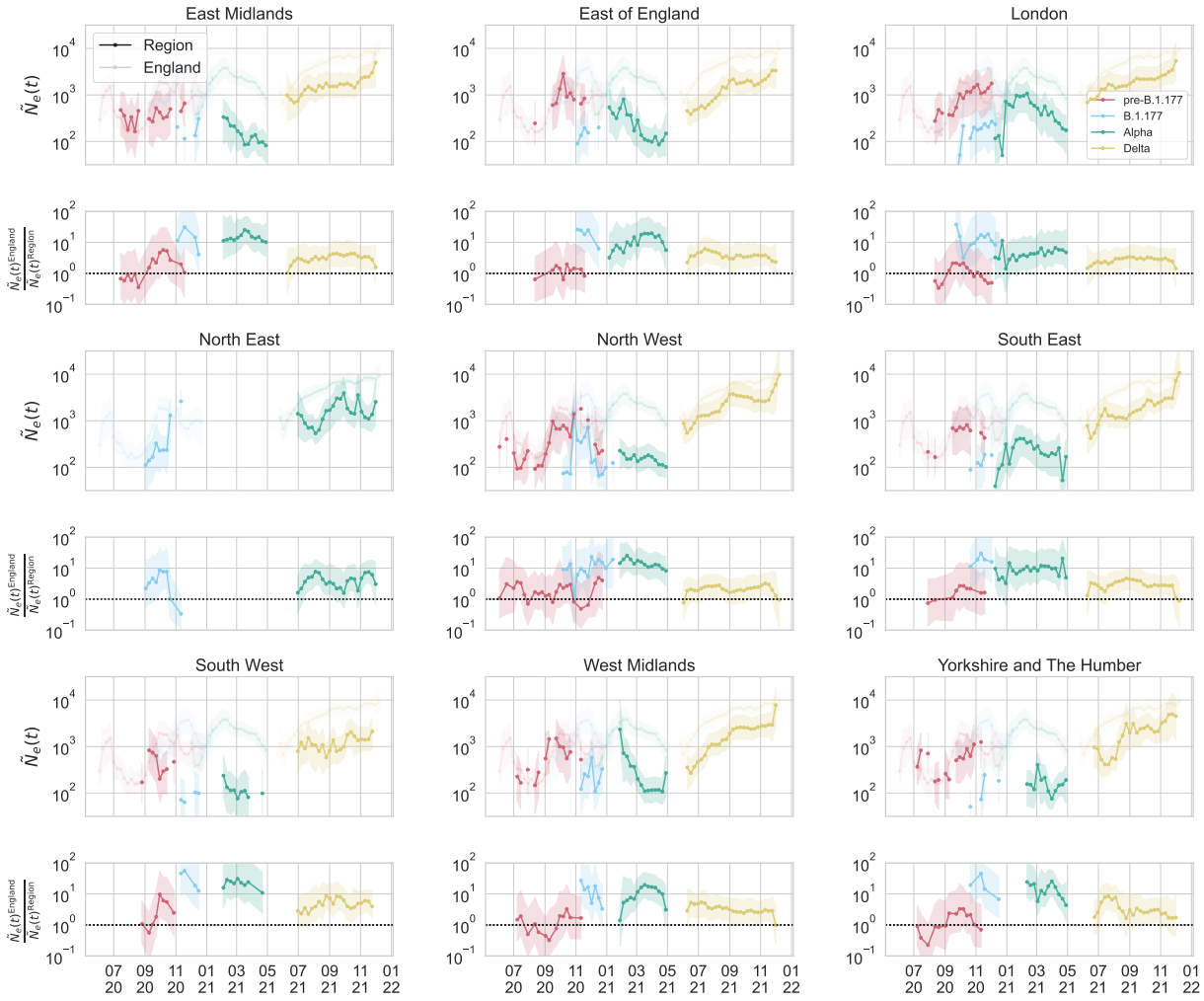

Figure S1: Inferred effective population size in regions of England. (Top panels) Inferred $\tilde{N}_e(t)$ of pre-B.1.177 lineages, B.1.177, Alpha, and Delta for each region of England. The inferred $\tilde{N}_e(t)$ for England as a whole is shown for reference. Shaded regions show 95% confidence intervals (see Methods). (Bottom panels) The ratio between the inferred $\tilde{N}_e(t)$ of England and that of the region for each variant. A horizontal dashed line indicates a ratio of 1 (i.e. $\tilde{N}_e(t)$ is the same in that region of England and England as a whole). Shared regions show the minimum and maximum possible values of the ratio from the combined error intervals of the numerator and denominator (thus, not corresponding to a specific confidence interval range).

The inference of effective population size can also reveal information about the well-mixed or spatially-structured nature of transmission dynamics within England. This can be done by inferring effective pop-

ulation size at smaller geographical scales within England. If the transmission dynamics were completely well-mixed, then we would expect $\tilde{N}_e(t)$ to be the same across regions and compared to England. On the other hand, if the transmission dynamics were completely spatially segregated (i.e. transmission only occurs within the defined geographical areas, but not between them) and the dynamics were the same in each region, we would expect that the ratio $\tilde{N_e}^{\text{SIR}}(t)/\tilde{N_e}^{\text{inf}}(t)$ to be the same across regions.

The geographical areas that we used were the 9 regions of England: East Midlands, East of England, London, North East, North West, South East, South West, West Midlands, and Yorkshire and The Humber. We looked at sequences from each region, repeating the analysis described above, and inferred the scaled effective population size (Figure S1). We observe a lower $\tilde{N}_e(t)$ for in the region than in England for Delta in all regions, for Alpha in all regions except North East (where there was not enough data), and for B.1.177 in all regions except North East. For lineages pre-B.1.177, the inferred $\tilde{N}_e(t)$ is not significantly diffent in the region than in England. These results suggest that the dynamics are not well-mixed during the B.1.177, Alpha, and Delta waves.

The calculated SIR model $\tilde{N_e}^{\text{SIR}}(t)$ (Figure S2) and the number of positive individuals in each region (Figure S3) were 1-2 orders of magnitude higher than the inferred $\tilde{N}_e(t)$, suggesting high levels of genetic drift. The ratios of the SIR model $\tilde{N}_e(t)$ and the number of positives to the inferred $\tilde{N}_e(t)$ in the regions were similar to one another and to that seen in England as a whole, consistent with a scenario where the dynamics are spatially-structured and the extent of stochasticity in transmission is similar across regions.

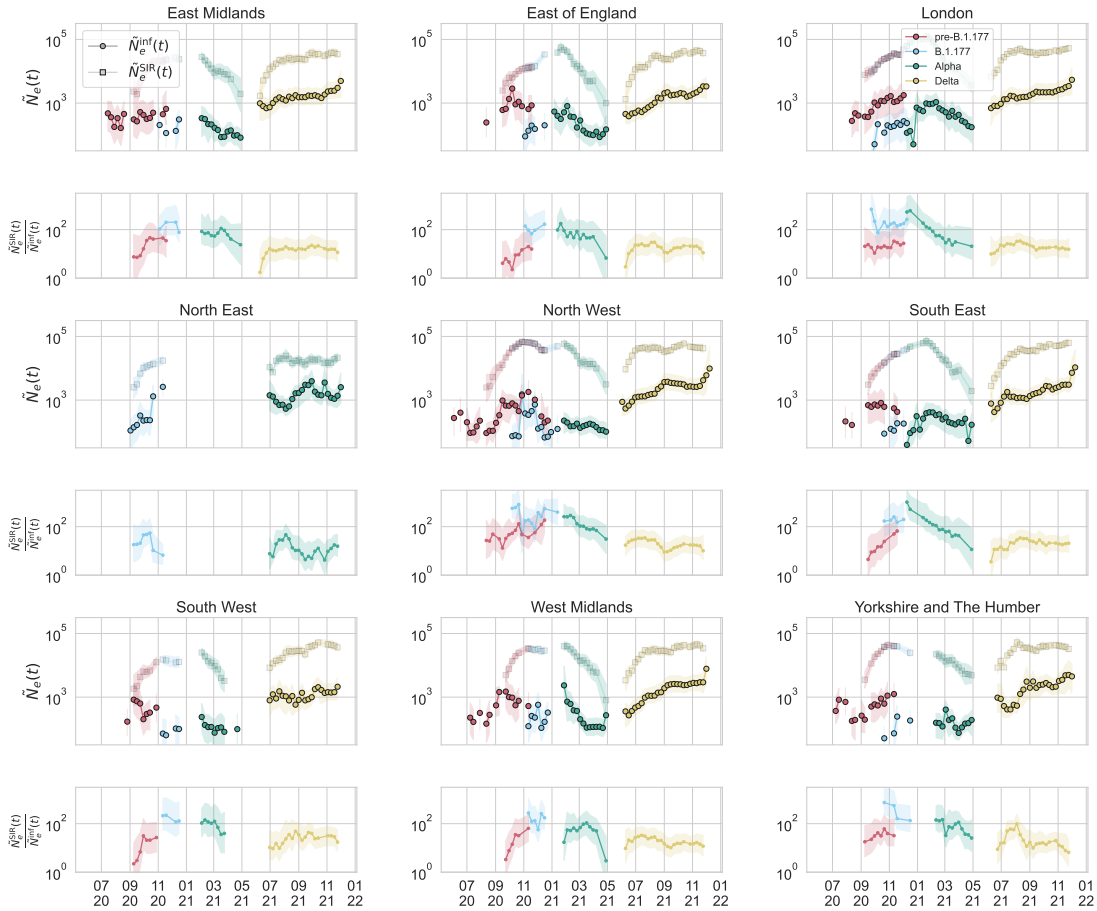

Figure S2: Inferred scaled effective population size by region in England, compared to that of an SIR model as calculated using the observed number of positives at the community level in that region reported by the COVID-19 Infection Survey [31] and the observed effective reproduction number in that region reported by the UK Health Security Agency [40].

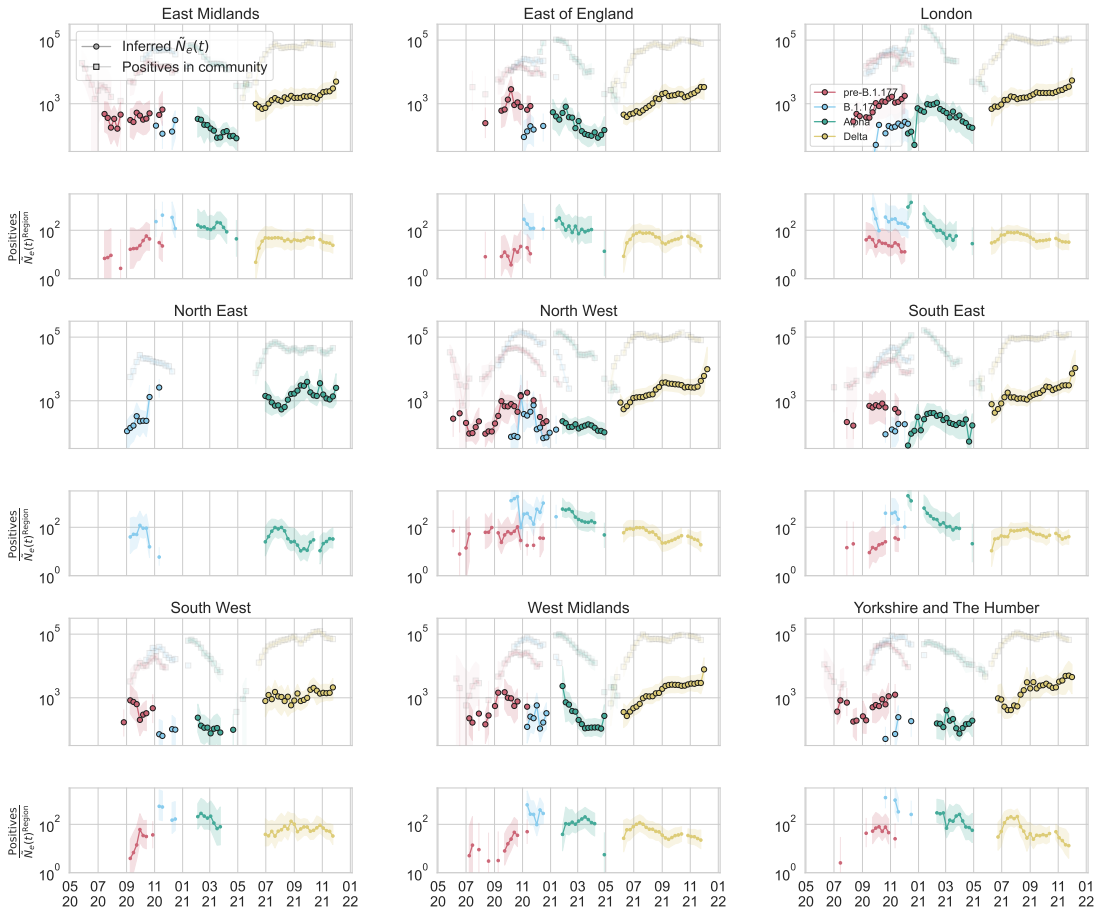

Figure S3: Inferred scaled effective population size by region in England, compared to number of positives at the community level in that region reported by the COVID-19 Infection Survey [31].

Similarly to in England as a whole, the inferred measurement noise in each region was mostly indistinguishable from uniform sampling except for in a few timepoints (Figure S4).

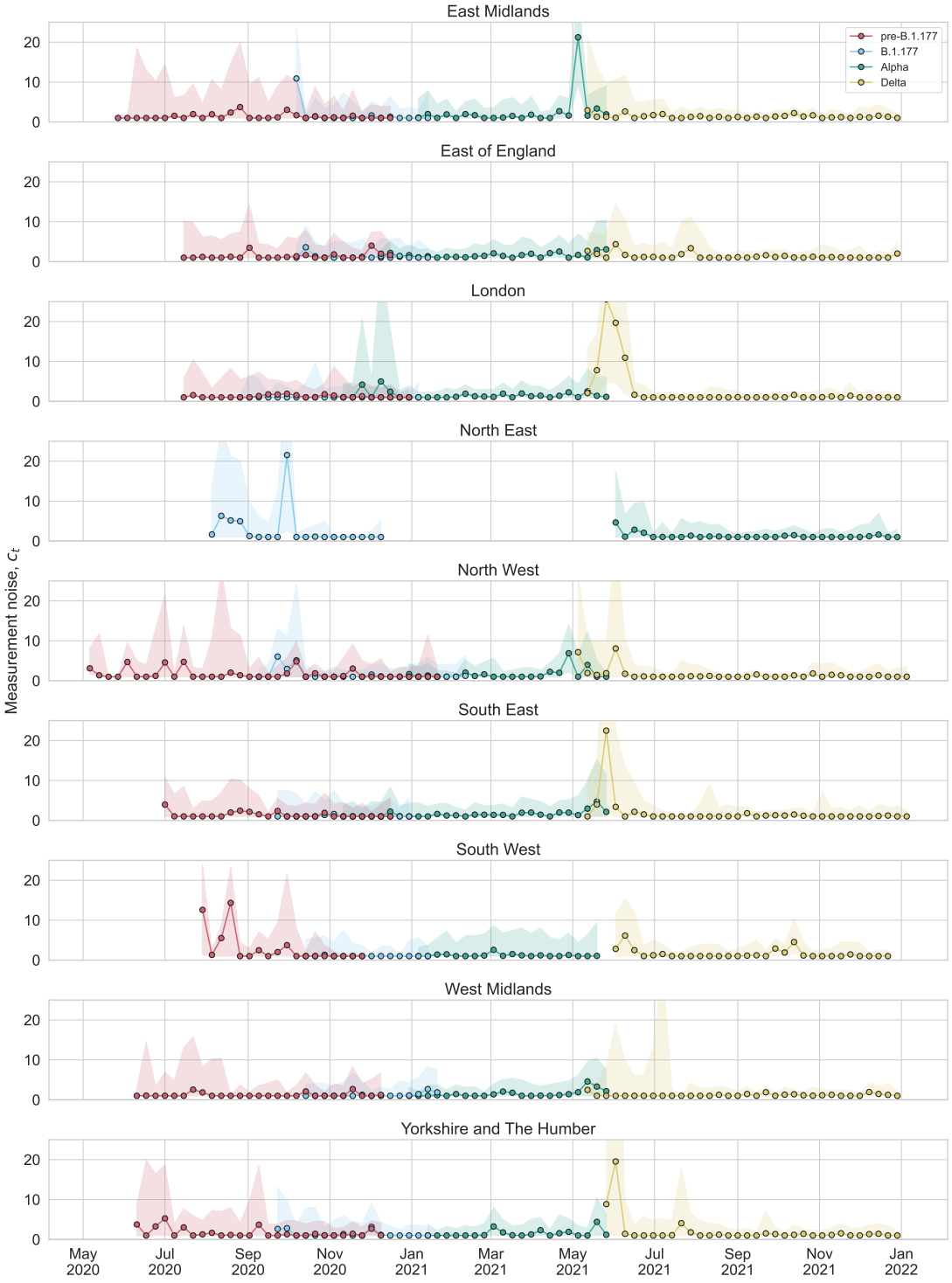

Figure S4: Inferred measurement noise by region in England.

Additional supplementary tables and figures

Date	**Location**	**Method**	$\langle Z \rangle$	**Var(Z)**	k	**Reference**
February 23 to April 22 2020	Israel	Phylodynamics	2.5 (2, 3)	(65, 627.5)	(0.02, 0.1)	[41]
Beginning of pandemic to February 27 2020	Worldwide excluding China	Branching process model of number of imported and local cases	2.5 (,)	65 (33.75, 127.5)	0.1 (0.05, 0.2)	[44]
March 1 to May 3 2020	Georgia (USA)	Spatiotemporal transmission model fit to multiple data sources	2 (0.5, 3.5)	12.26 (0.88, 101.5)	0.39 (0.125, 0.65)	[92]
March 1 to November 1 2020	Denmark	Model fitting the case numbers across multiple regions	1.1 (0.8, 1.4)	12.1 (4.36, 25.9)	0.11 (0.08, 0.18)	[93]
Beginning of pandemic until January 18 2020	China (Wuhan)	Stochastic simulations fit to infected cases	2.2 (1.4, 3.8)	11.16 (1.68, 1035.2)	0.54 (0.014, 6.95)	[94]
August to September 2020	UK	Model using empirical viral load trajectories and contact numbers	1.21 (0.84, 2.51)	7.07 (2.65, 44.51)	0.25 (0.15, 0.39)	[45]
May 15 to August 1 2020	Tamil Nadu and Andhra Pradesh (India)	Contact tracing and incidence	1.25 (1.1, 1.4)	4.31 (3.43, 5.4)	0.51 (0.49, 0.52)	[55]
January to February 2021	UK	Model using empirical viral load trajectories and contact numbers	0.54 (0.4, 1.03)	1.42 (0.66, 9.19)	0.33 (0.13, 0.61)	[45]
January 23 to April 28 2020	Hong Kong	Contact tracing	0.58 (,)	1.36 (,)	0.43 (,)	[56]
January 16 to April 3 2020	Hunan (China)	Contact tracing	0.4 (0.35, 0.47)	0.93 (0.66, 1.43)	0.3 (0.23, 0.39)	[57]
January 14 to February 12 2020	Shenzhen (China)	Contact tracing	0.4 (0.3, 0.5)	0.68 (0.38, 1.21)	0.58 (0.35, 1.18)	[58]

Table S1: Overdispersion values from the literature ordered from highest to lowest variance in offspring number. Any error intervals that are reported are taken from the reference (sometimes defined differently). The estimate taken from Ref. [45] assumes no self-isolation upon symptom onset and no testing; lifting these assumptions leads to similar or lower overdispersion.

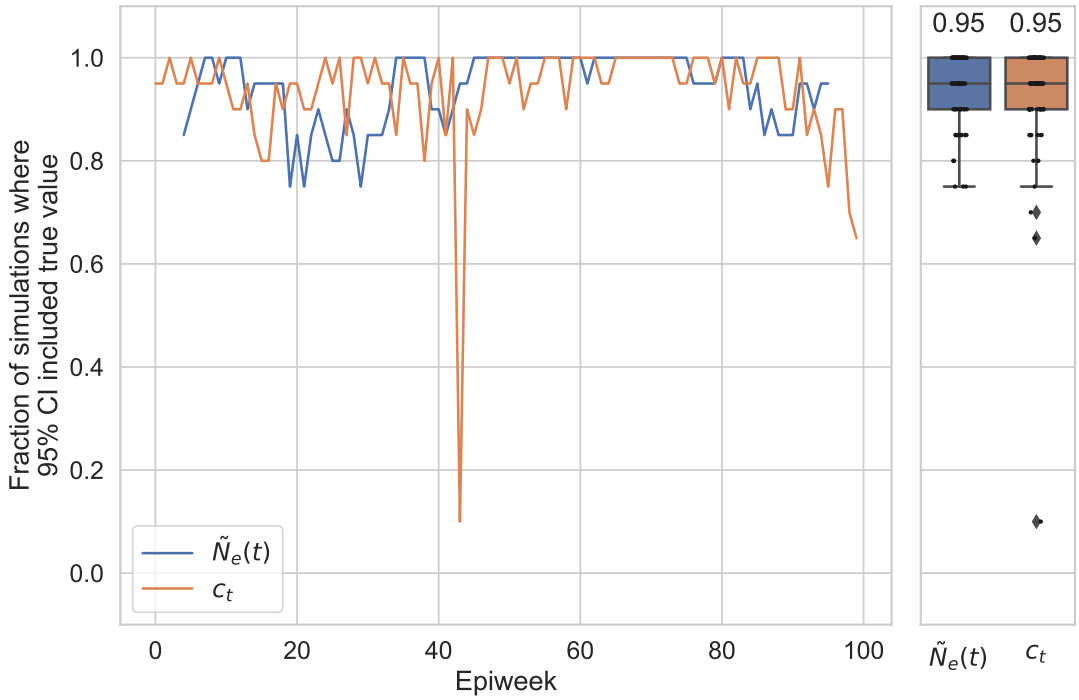

Figure S5: The fraction of simulations (20 total) where the inferred 95% confidence interval for $\tilde{N}_e(t)$ or c included the true value (left) by timepoint and (right) for all timepoints. (Right) Boxes indicate the quartiles and the line inside the box (and number above) indicates the median. Whiskers indicate the extreme values excluding outliers. Simulation parameters are specified in the Methods and Figure 1, which shows a single simulation instance. For the inference, we created coarse-grained lineages randomly 20 times.

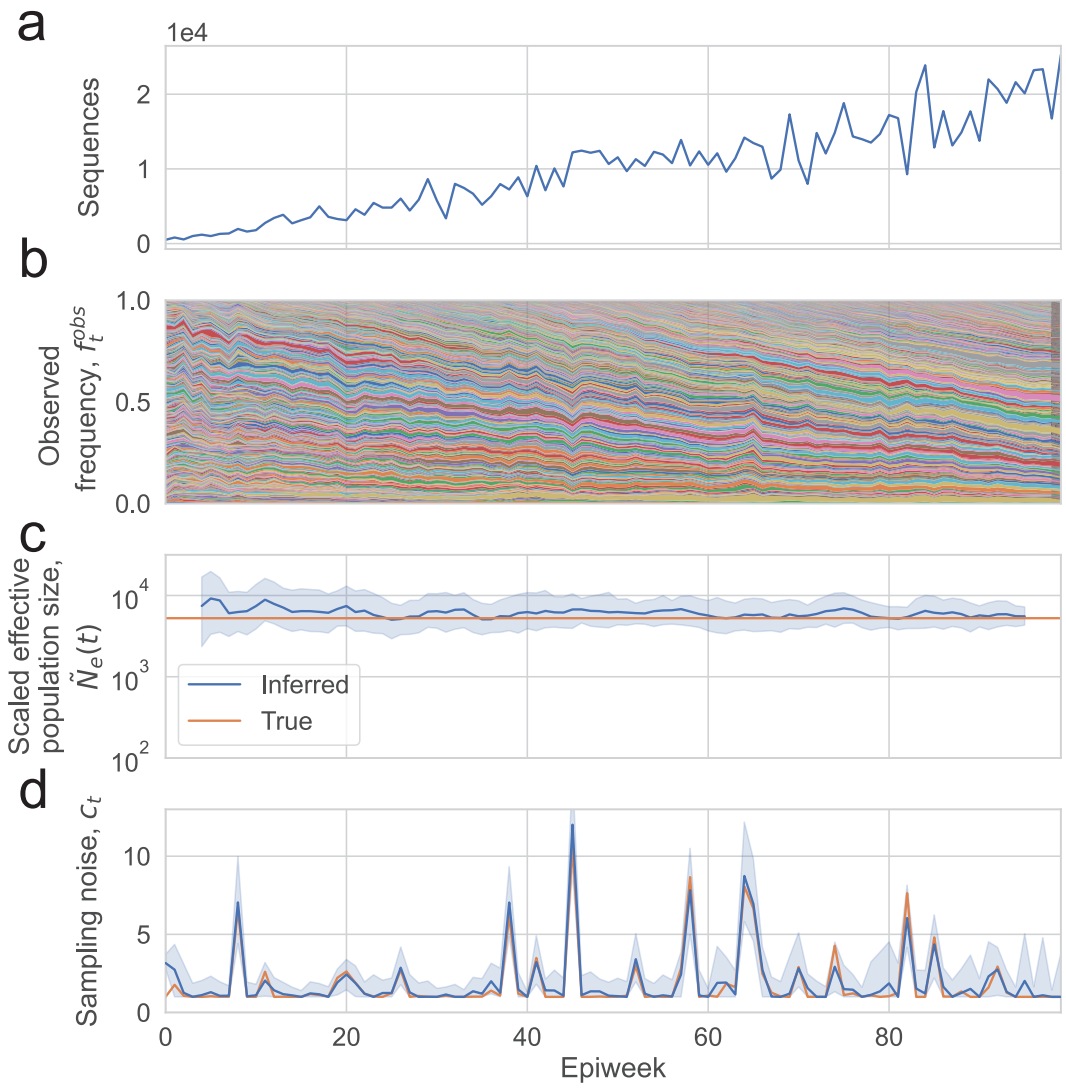

Figure S6: Wright-Fisher simulations where $\tilde{N}_e(t)$ is constant over time, and the inferred $\tilde{N}_e(t)$ and c_t. (a) Number of sequences sampled. (b) Simulated lineage frequency trajectories. (c) Inferred effective population size ($\tilde{N}_e(t)$) on simulated data compared to true values. (d) Inferred measurement noise (c_t) on simulated data compared to true values. In (c) the shaded region shows the 95% confidence interval calculated using the posterior, and in (d) the shaded region shows the 95% confidence interval calculated using bootstrapping (see Methods).

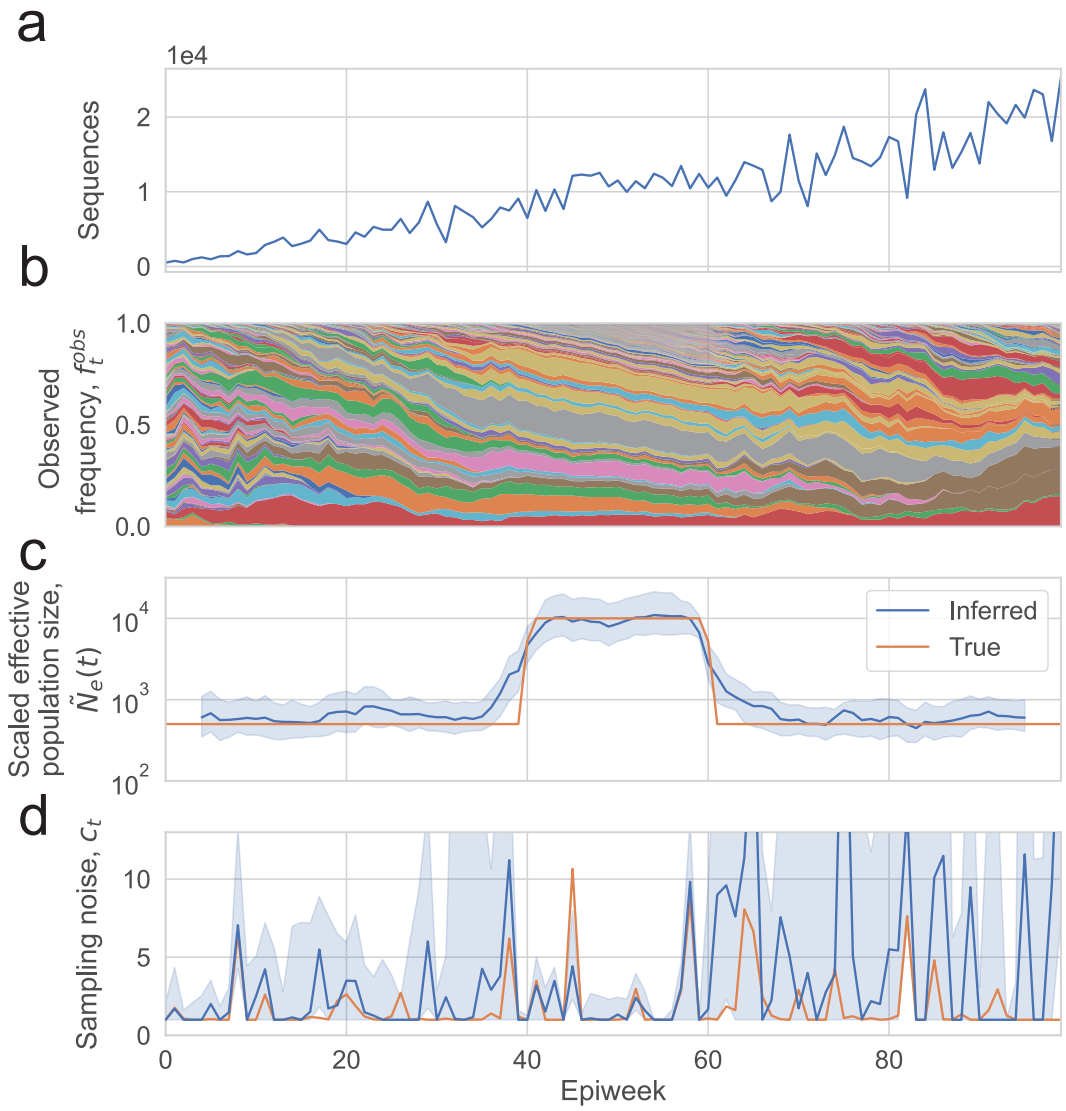

Figure S7: Wright-Fisher simulations where $\tilde{N}_e(t)$ changes over time according to a rectangular function, and the inferred $\tilde{N}_e(t)$ and c_t. (a) Number of sequences sampled. (b) Simulated lineage frequency trajectories. (c) Inferred effective population size ($\tilde{N}_e(t)$) on simulated data compared to true values when c_t is jointly inferred and when c_t is fixed at 1 (uniform sampling). (d) Inferred measurement noise (c_t) on simulated data compared to true values. In (c) the shaded region shows the 95% confidence interval calculated using the posterior, and in (d) the shaded region shows the 95% confidence interval calculated using bootstrapping (see Methods).

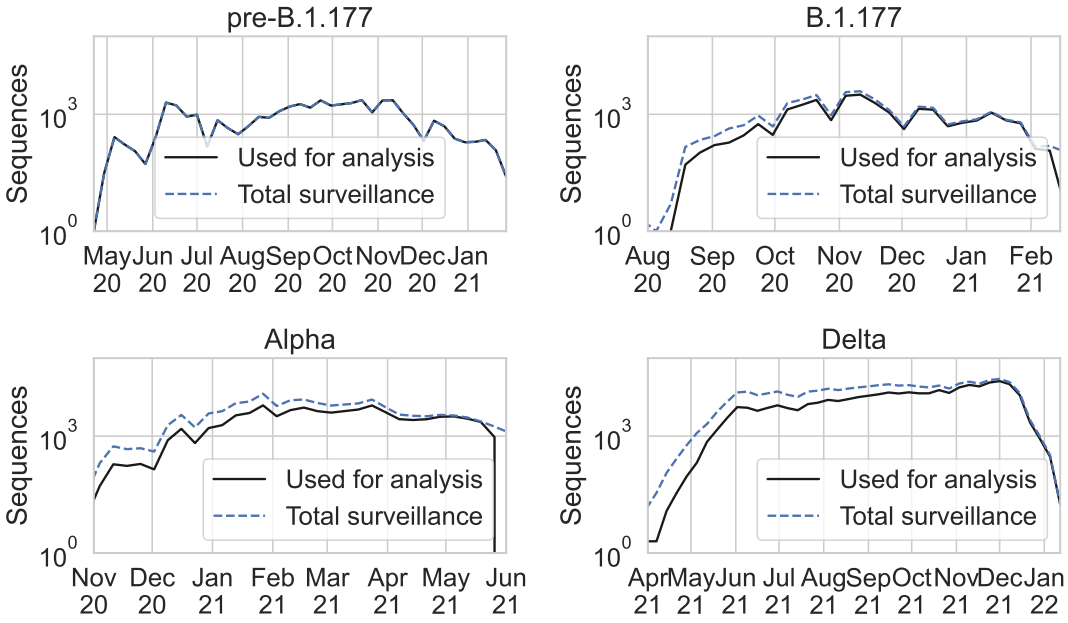

Figure S8: Total number of surveillance sequences of each variant in the metadata from COG-UK downloaded on January 16, 2022 and the number of sequences used in the analysis for each variant or group of lineages (determined by the number of sequences included in the tree, and the number of sequences which could be grouped into sublineages based on the procedure described in the Methods).

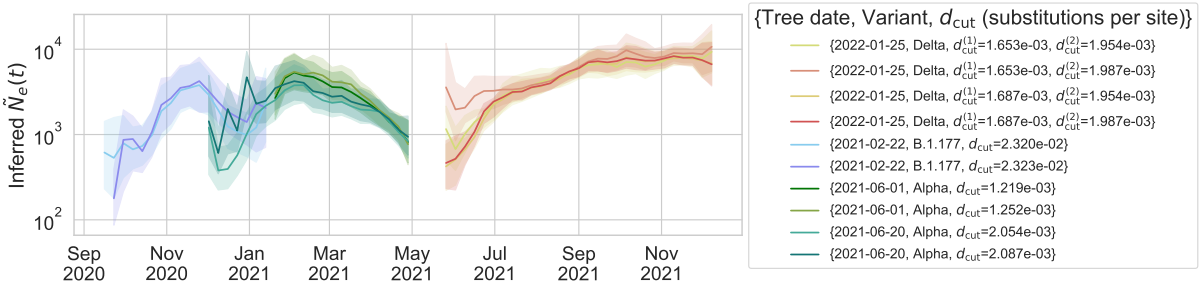

Figure S9: Varying the date of the tree downloaded from COG-UK and the depth at which the tree is cut for creating lineages (d_{cut}, which is defined as the number of mutations from the root of the tree, see Methods) does not substantially change the inferred scaled effective population size. The tree date and depth used in the main text are {2021-02-22, B.1.177, $d_{\text{cut}} = 2.323 \cdot 10^{-2}$}, {2021-06-20, Alpha, $d_{\text{cut}} = 2.054 \cdot 10^{-3}$}, {2022-01-25, Delta, $d_{\text{cut}}^{(1)} = 1.687 \cdot 10^{-3}$, $d_{\text{cut}}^{(2)} = 1.954 \cdot 10^{-3}$}. The color of the lines for the parameters that were used in the main text are the same as those shown in Figure 2.

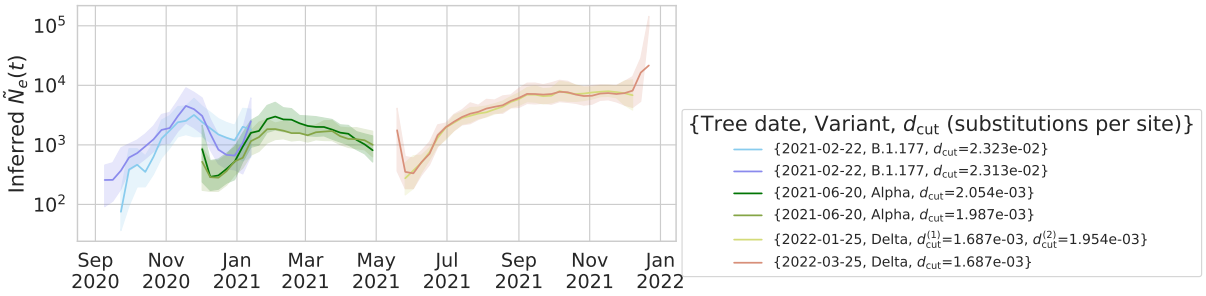

Figure S10: The inferred effective population size when cutting the tree at different depths to test the effect of combining lineages with other more closely related lineages in forming the coarse-grained lineages.

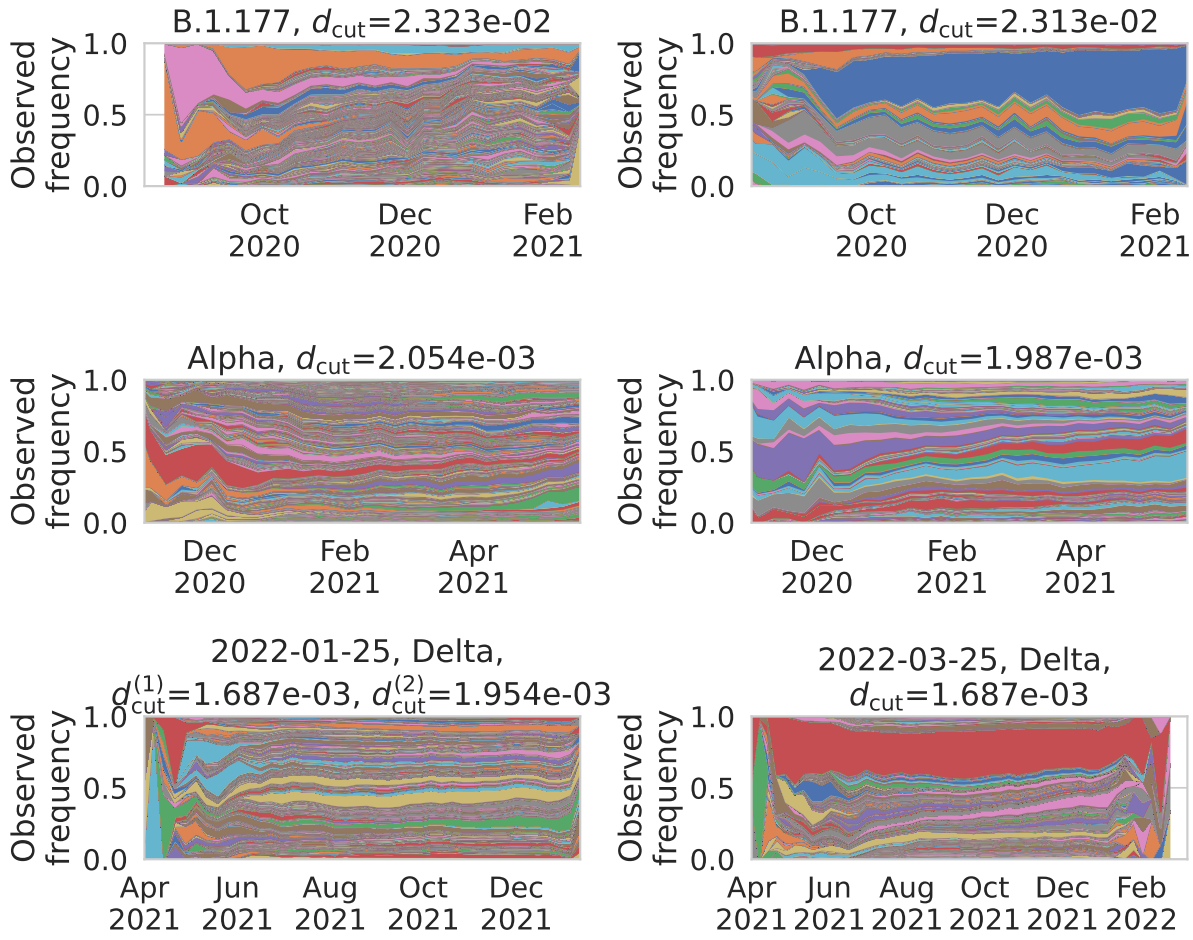

Figure S11: The lineage frequency time series using the tree cut depths shown in Figure S10.

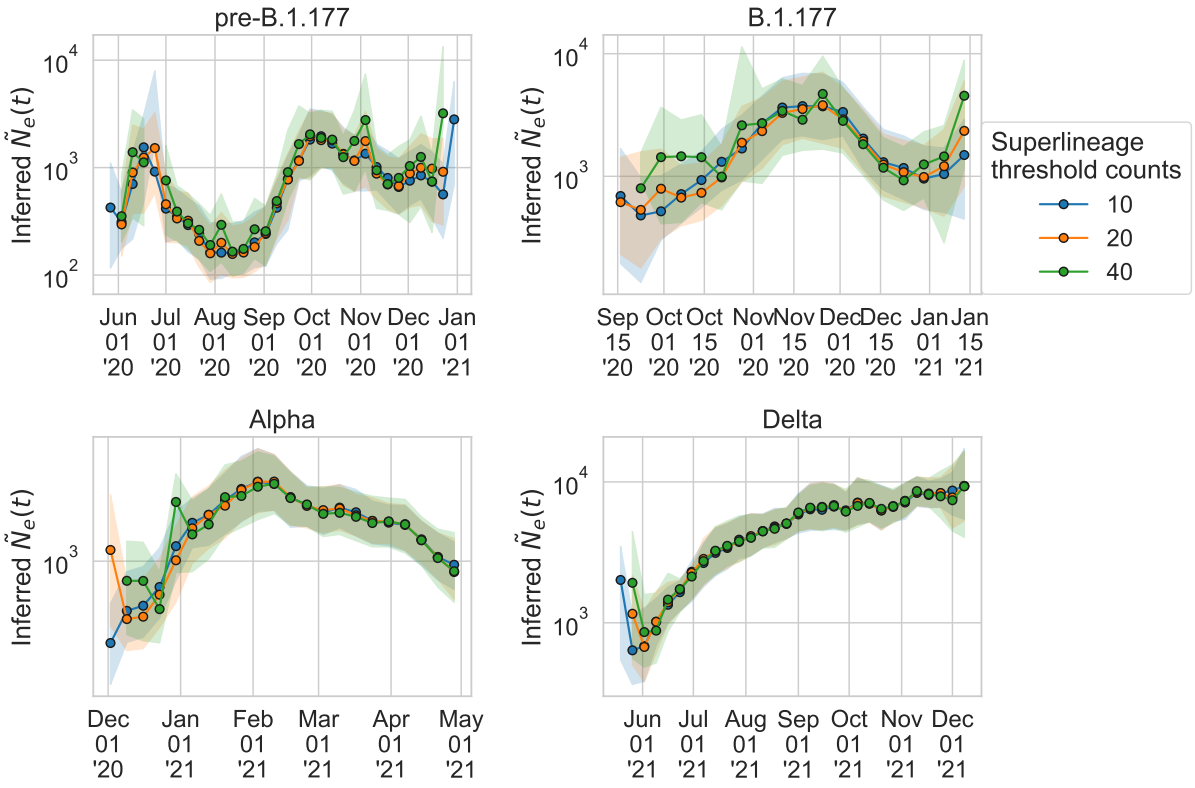

Figure S12: Varying the threshold counts for forming coarse-grained lineages (see Methods) does not substantially change the inferred scaled effective population size. The coarse-grained lineage threshold counts used in the main text is 20.

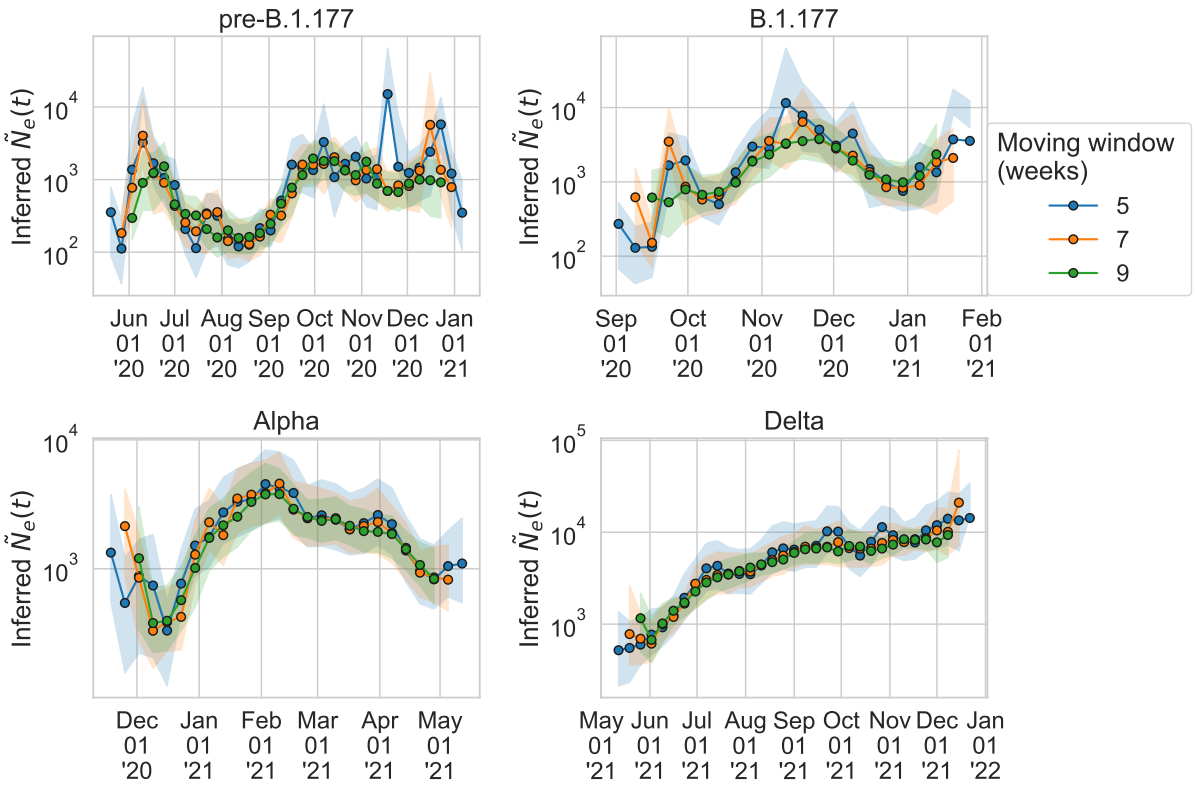

Figure S13: Varying the number of weeks in the moving window does not substantially change the inferred scaled effective population size. The size of the moving window used in the main text is 9 weeks.

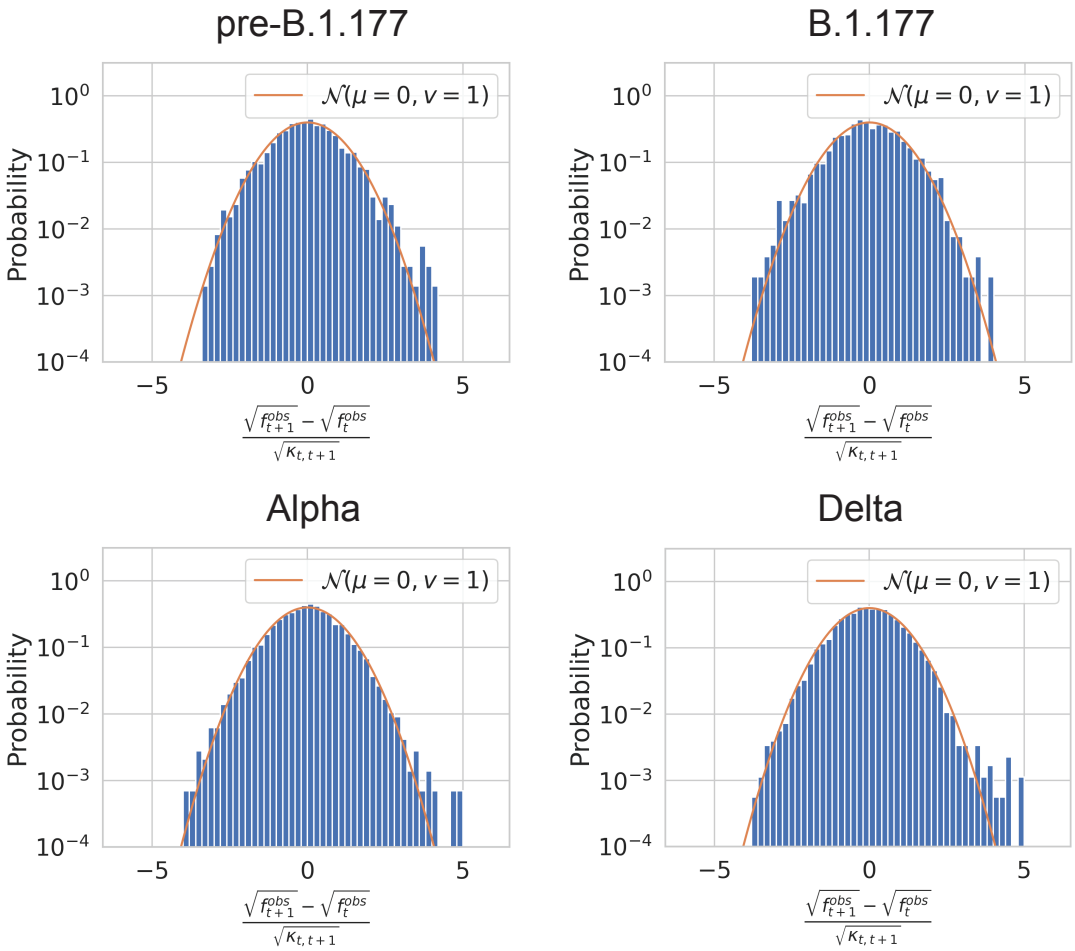

Figure S14: The distribution of square root observed frequency displacements ($\sqrt{f_{t+1}^{obs}} - \sqrt{f_t^{obs}}$) across all time points normalized by the inferred variance due to genetic drift and measurement noise ($\kappa_{t,t+1} = \frac{c_t}{4M_t} + \frac{c_{t+1}}{4M_{t+1}} + \frac{1}{\tilde{N}_e(t)}$, see Equation 24). The orange line is a plot of a normal distribution with mean 0 and variance 1.

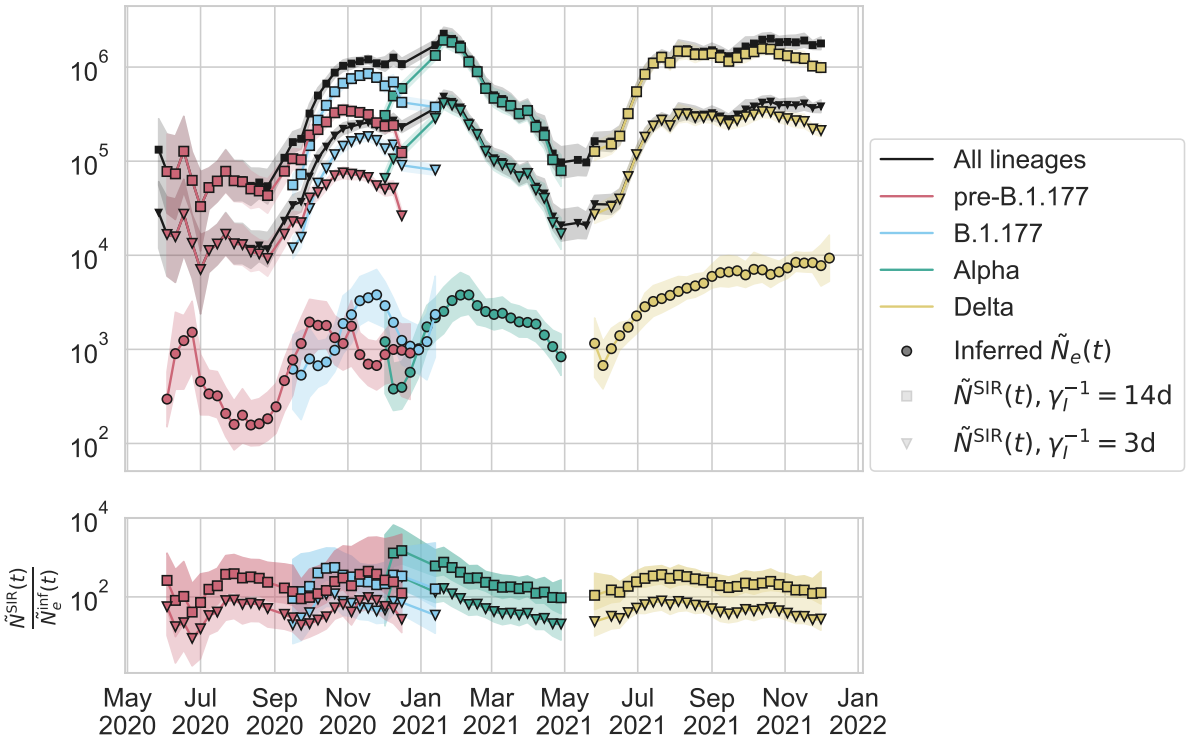

Figure S15: Varying the rate of transitioning from infected to recovered within literature ranges (γ_I =3 to 14 days) used for calculation of the SIR model $\tilde{N}_e(t)$ (Methods) does not substantially decrease the observed ratio $\tilde{N_e}^{\mathrm{SIR}}(t)/\tilde{N_e}^{\mathrm{inf}}(t)$.

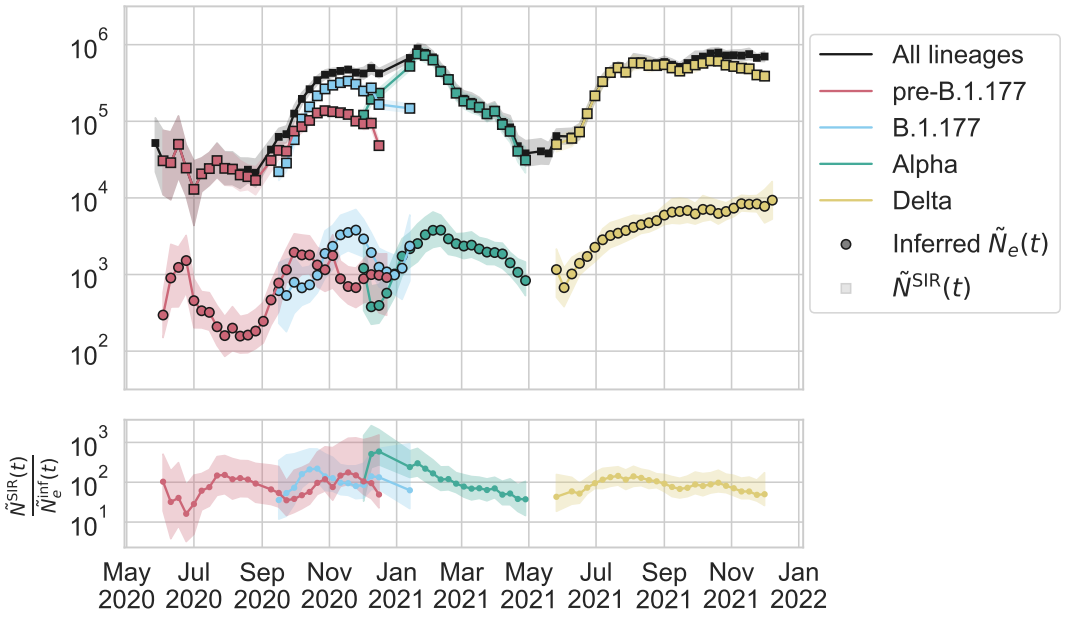

Figure S16: Inferred scaled effective population size compared to the SIR model scaled population size calculated using the observed number of positive individuals in England (see Methods).

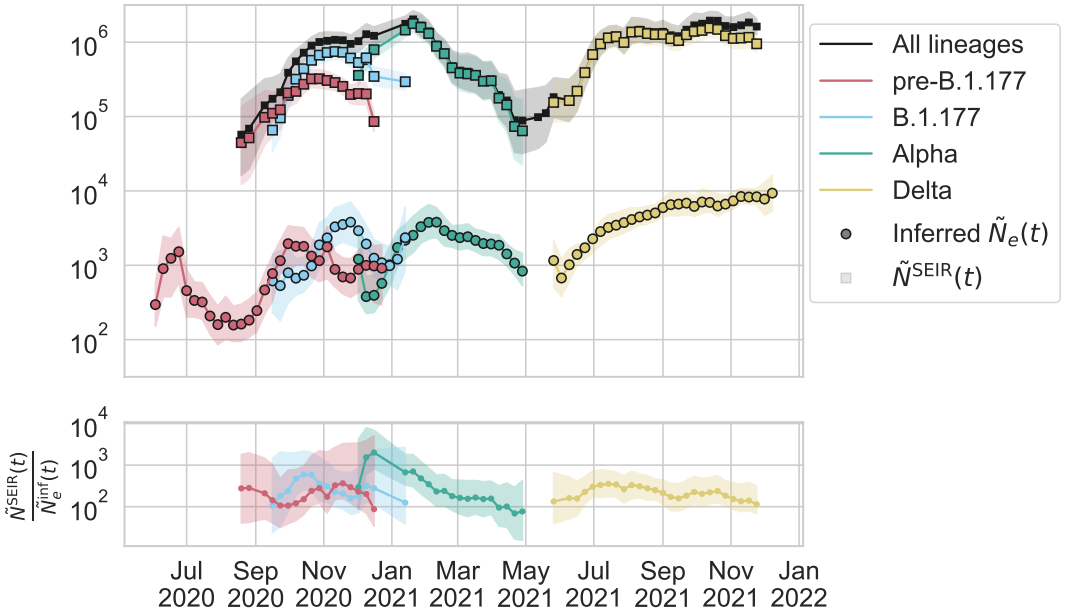

Figure S17: Inferred scaled effective population size compared to the SEIR model scaled population size calculated using the observed number of positive individuals in England (see Methods).

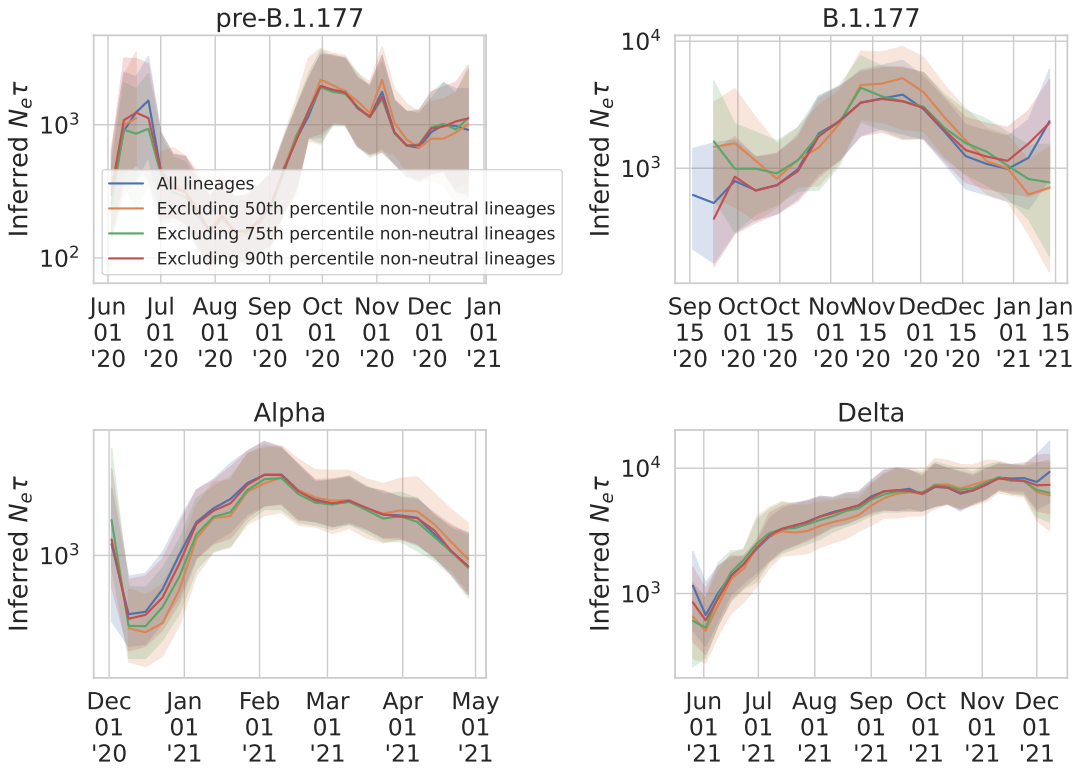

Figure S18: The inferred effective population size when excluding beneficial lineages whose inferred absolute fitness value are above the 50th ($|s| > 0.09$), 75th ($|s| > 0.16$), and 90th ($|s| > 0.27$) percentiles compared to that when all lineages are included.

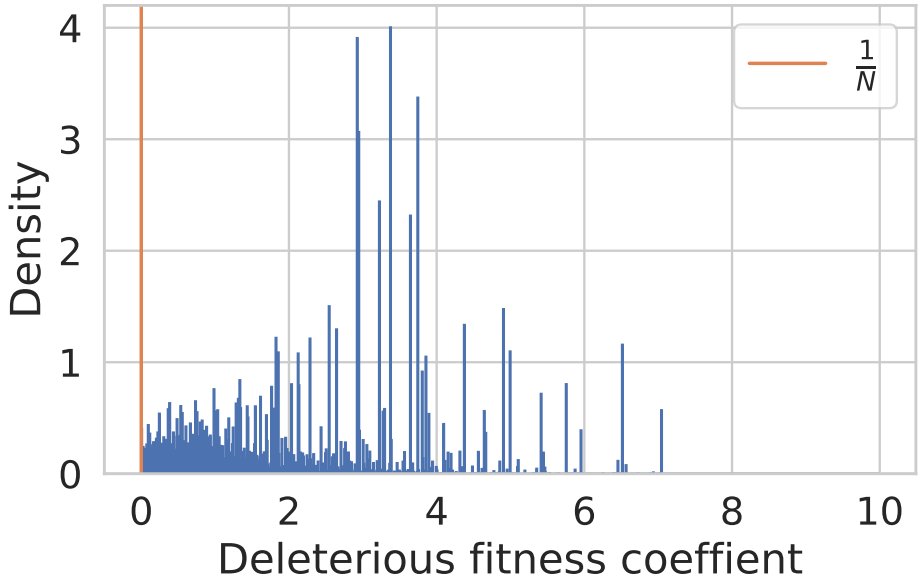

Figure S19: The distribution of deleterious fitness effects from Ref. [46]. The orange vertical line indicates $\frac{1}{N}$, which is the threshold in fitness above which selection dominates over genetic drift. Here, N is set to 10^4, which is the order of magnitude of the census population size of SARS-CoV-2 in England.

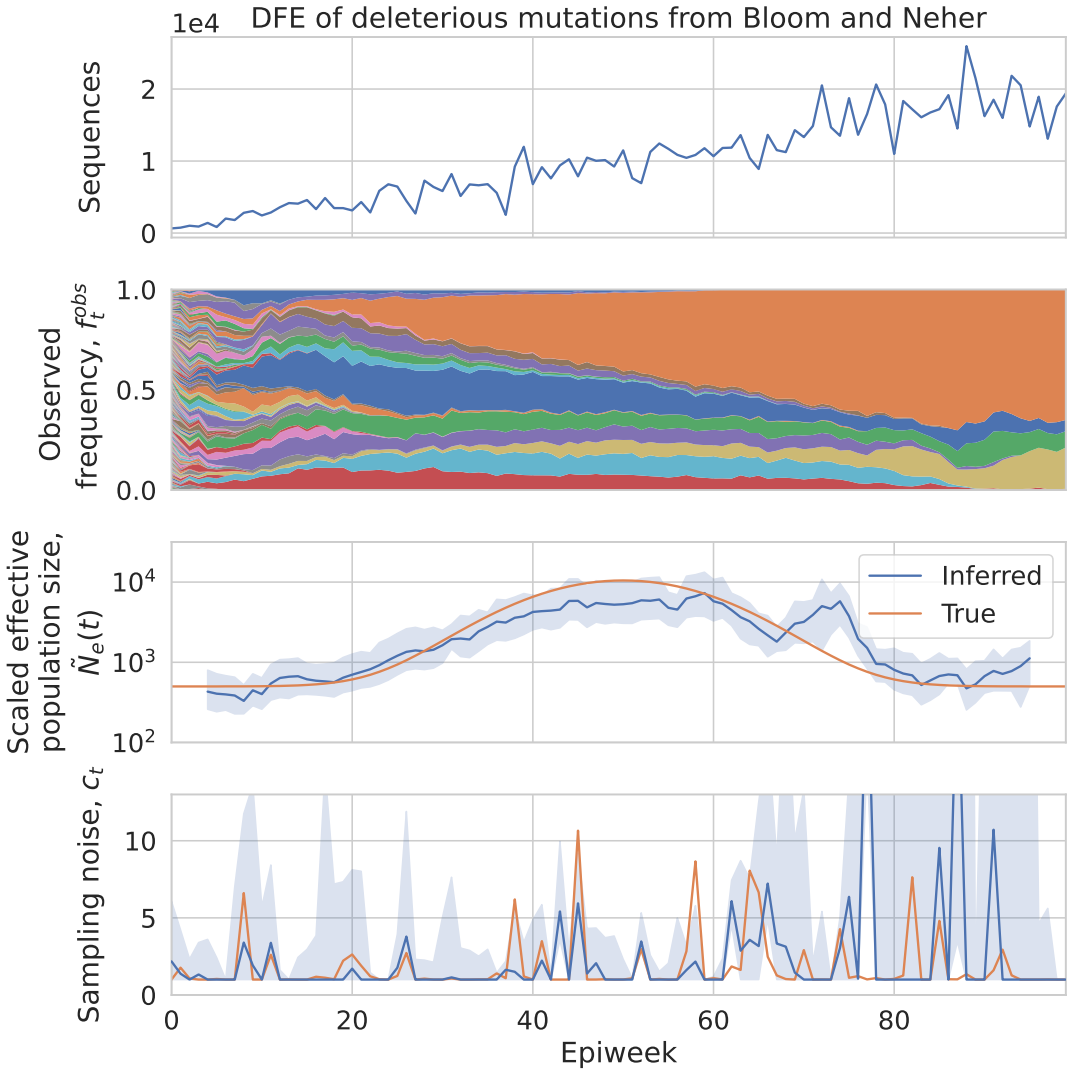

Figure S20: Simulated lineage frequency dynamics where deleterious mutations occur at rate 0.01/genome/generation and the distribution of deleterious fitness effects is taken from the empirically estimated values in Ref. [46]. The inferred effective population size and measurement noise are shown.

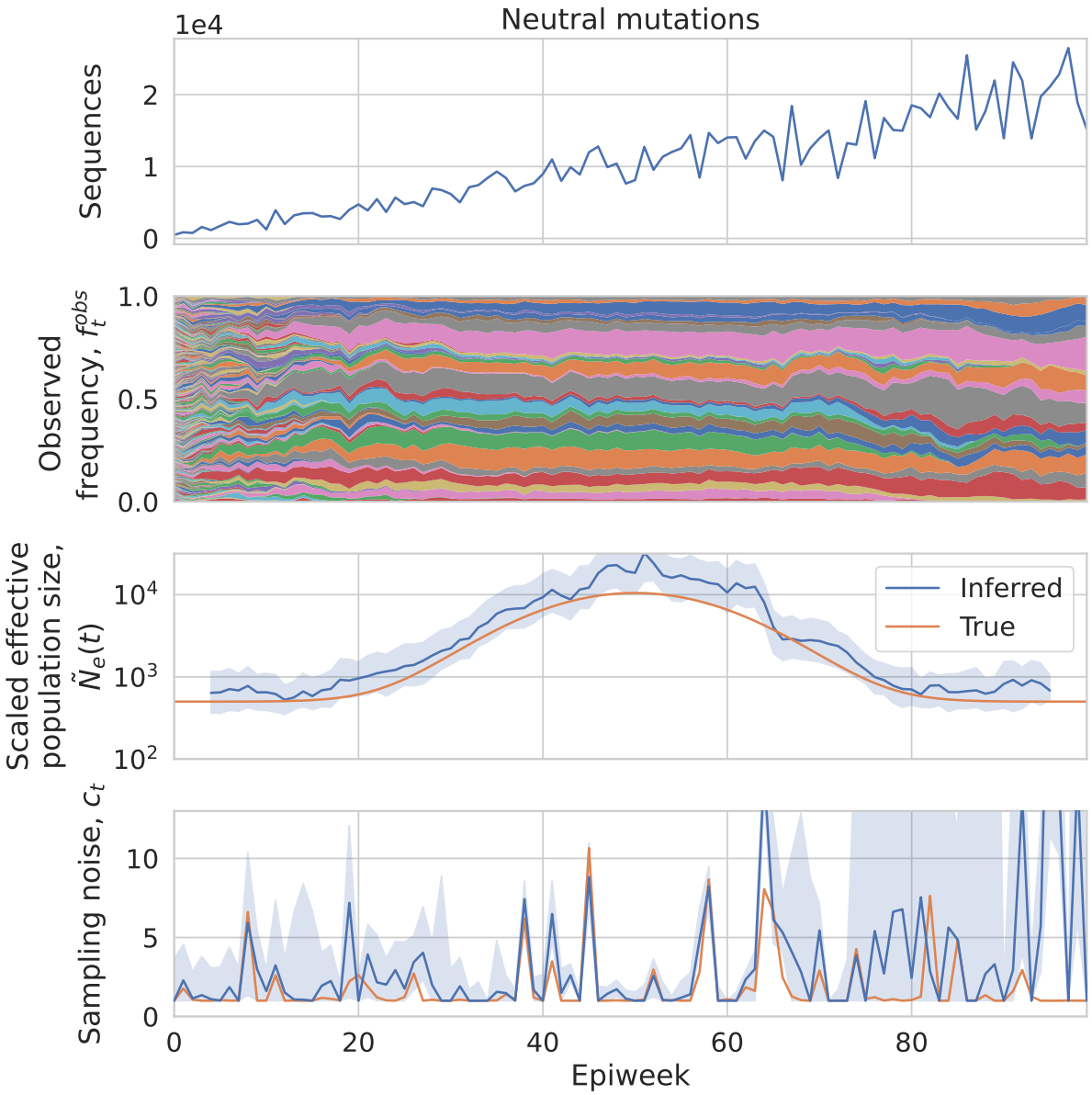

Figure S21: The same simulation as in Figure S20 but as a control, where the fitness of new mutations is always 0. The inferred effective population size and measurement noise are shown.

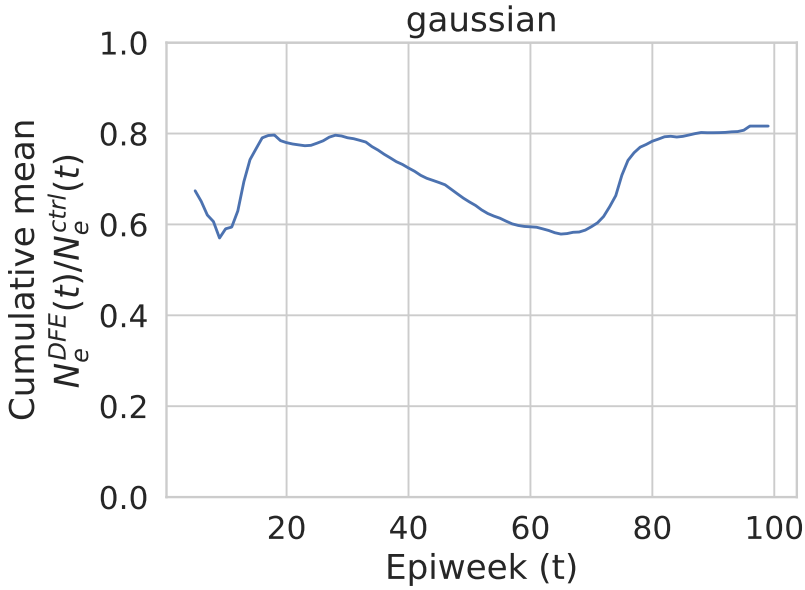

Figure S22: The cumulative mean ratio of the point estimates of the inferred effective population size in the simulations using the empirical distribution of deleterious fitness effects and the neutral simulations.

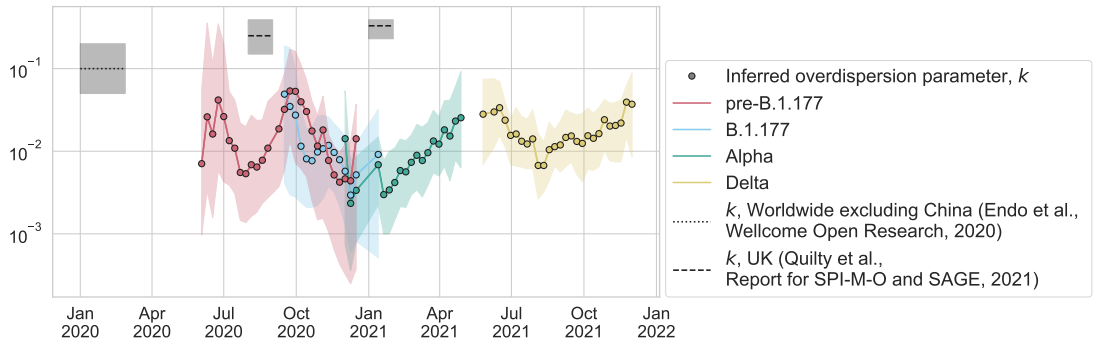

Figure S23: Same as Figure 3c, but plotting the overdispersion parameter, $k = \frac{R_t}{\frac{\sigma^2}{R_t}-1}$, where R_t is the effective reproduction number and σ^2 is the variance in offspring number. The circles show the inferred overdispersion parameter if we assume there is only superspreading and no deme structure. For the inferred overdispersion parameter, the estimated effective reproduction number in England by variant (see Methods) is used for R_t, and the ratio between the SIR model population size and the inferred effective population size is used for σ^2. The shaded area for the inferred overdispersion parameter k gives an estimate of the error and is calculated by combining minimum or maximum values of the individual parameters; note that this does not correspond to a particular confidence interval.

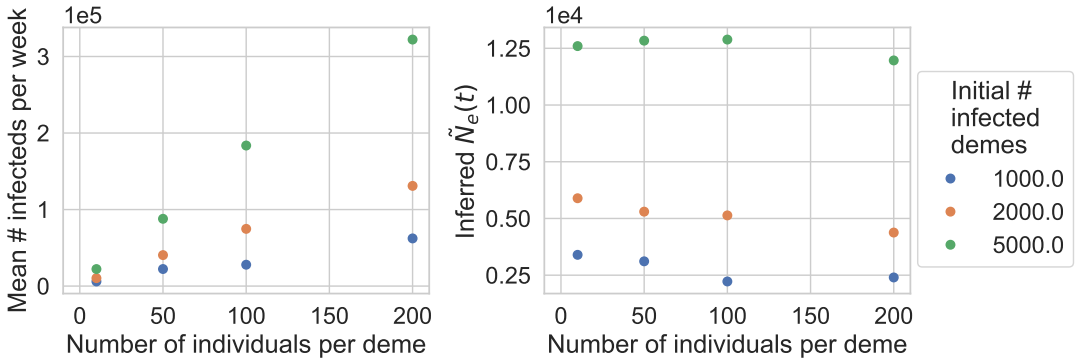

Figure S24: Simulations of deme structure (described in main text and Methods). (a) The mean number of infected individuals per week from Weeks 42 to 50. (b) The inferred $\tilde{N}_e(t)$ using lineage trajectories from Weeks 42 to 50.

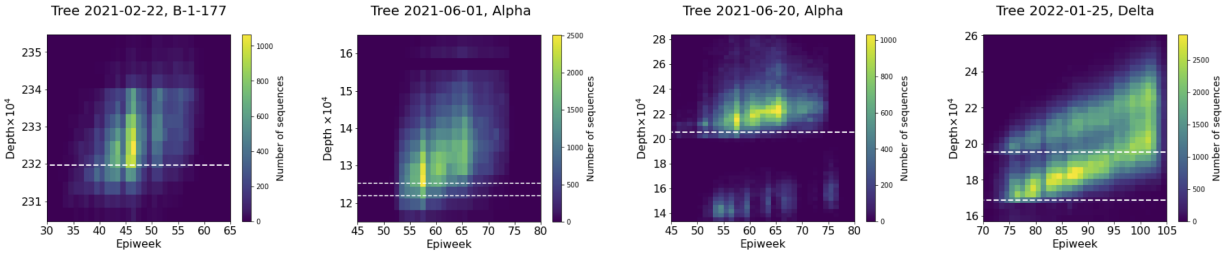

Figure S25: Sample epiweeks versus tree depths. In a phylogenetic tree, the number of sequences (leaf nodes) of a focal variant that fall within specific epiweek and tree depth ranges is counted and summarized as a two-dimensional histogram. The tree depth is the substitution rate measured in units of substitutions per site, with respect to the most recent common ancestor. From left to right, the phylogenetic tree (specified by date created by COG-UK, using the sequences available at the time) and focal variant are {2021-02-22, B-1-177}, {2021-06-01, Alpha}, {2021-06-20, Alpha}, and {2022-01-25, Delta}. Weeks are counted from 2019-12-29. The dashed horizontal lines indicate the values of d_{cut} ($d_{\text{cut}}^{(1)}$ and $d_{\text{cut}}^{(2)}$ for the Delta variant) used for the results presented in the main text, except for the 2021-06-01 Alpha tree, where they indicate the value of d_{cut} tested in the Supplementary Information.

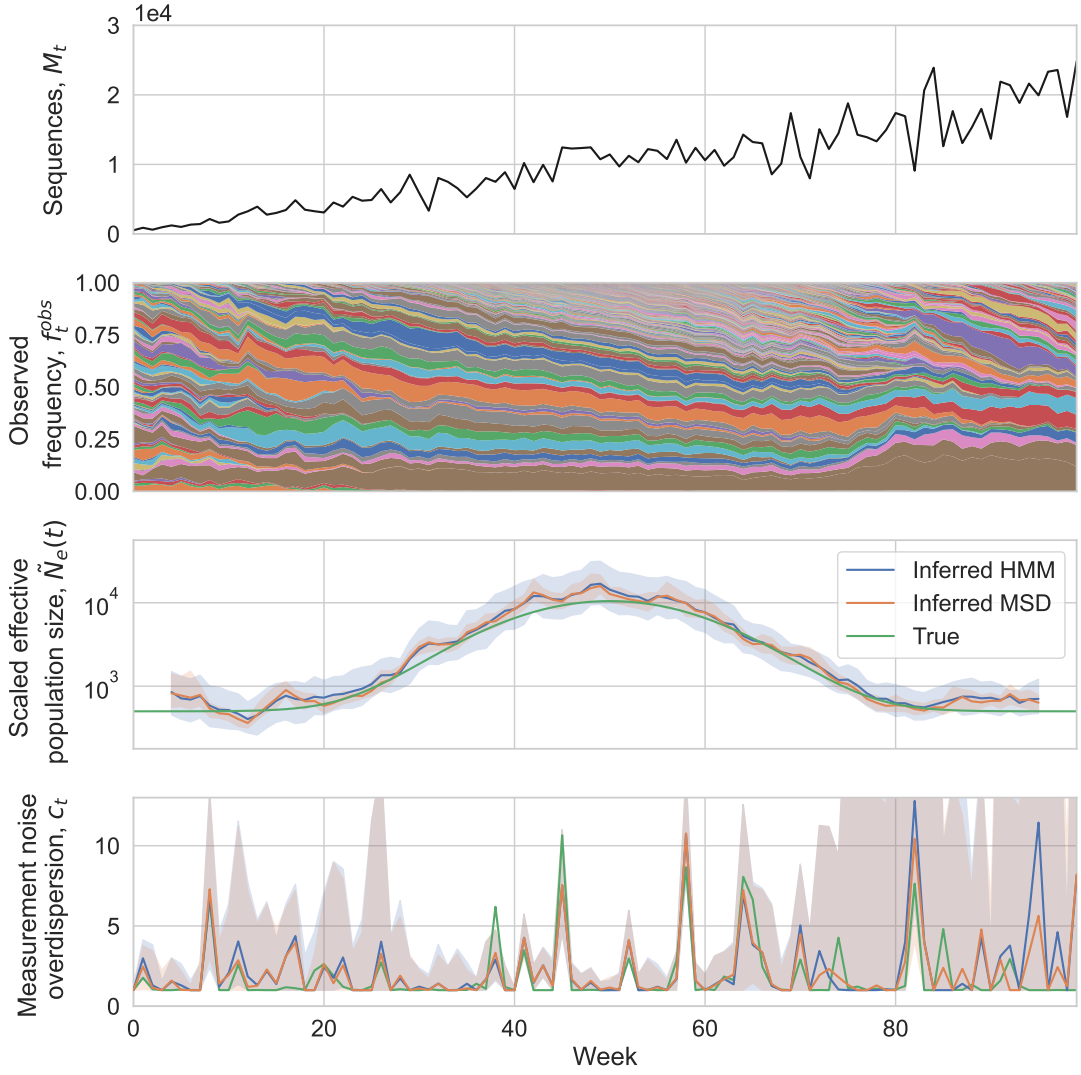

Figure S26: Comparing the inferred $\tilde{N}_e(t)$ and c_t in Wright-Fisher simulations using the method of moments and maximum likelihood estimation approaches (see Methods). (a) Number of sequences sampled. (b) Simulated lineage frequency trajectories. (c) Inferred effective population size ($\tilde{N}_e(t)$) on simulated data using the method of moments (MSD, for mean squared displacement) and maximum likelihood (HMM, for Hidden Markov Model) estimation approaches compared to true values. The shaded region shows the 95% confidence interval of the inferred values. The confidence interval using the method of moments approach was calculated by taking the middle 95% of values when bootstrapping over the coarse-grained lineages. The confidence interval using the maximum likelihood estimation approach was determined using the posterior (see Methods) and takes into account joint errors in c_t and $\tilde{N}_e(t)$. (d) Inferred measurement noise (c_t) on simulated data using the method of moments and maximum likelihood estimation approaches compared to true values. The shaded region shows the 95% confidence interval calculated using bootstrapping (see Methods).

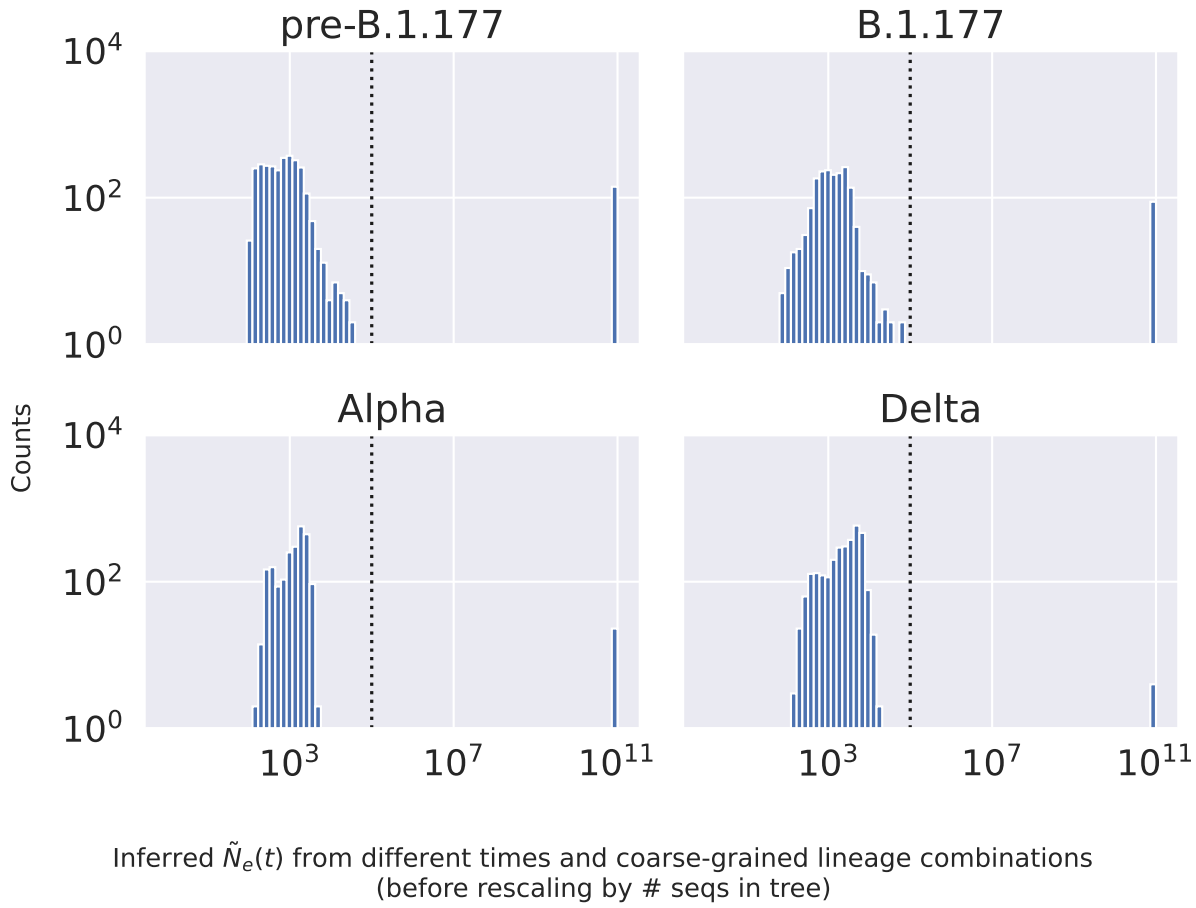

Figure S27: Inferred effective population size from different times and coarse-grained lineage combinations. The vertical dashed line indicates 10^5 which is the value above which results in the text were thrown away due to non-convergence (these only include values at 10^{11}).

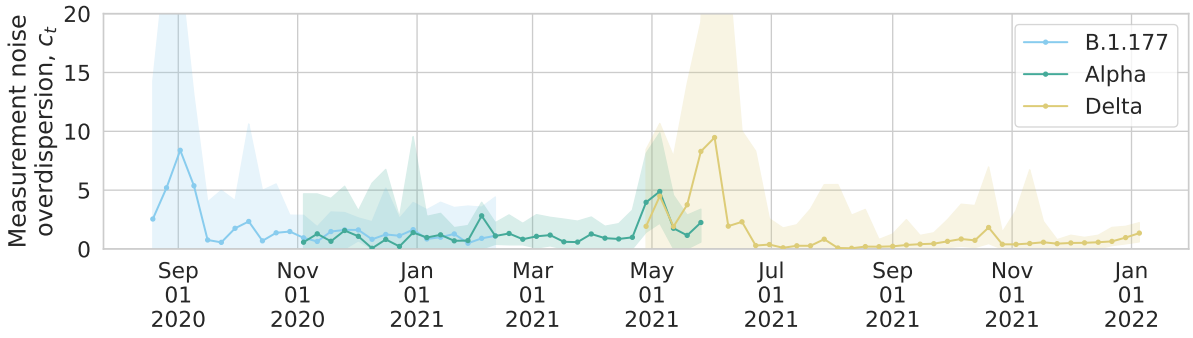

Figure S28: The inferred measurement noise overdispersion parameter for England as a whole when changing the lower bound of the overdispersion parameter from 1 to 0.

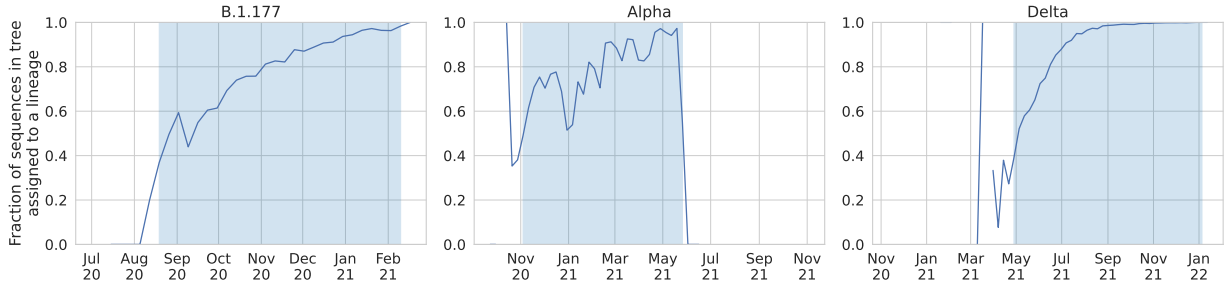

Figure S29: The fraction of sequences in the tree that are assigned to a lineage. The blue shading indicates the period of time in the data that was used for the inference analysis.

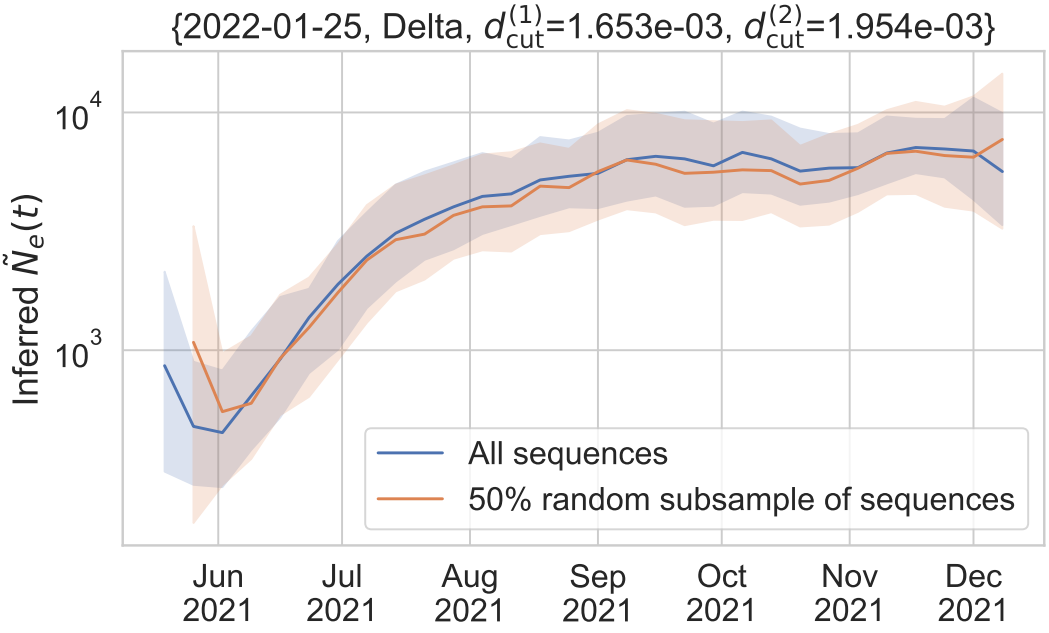

Figure S30: Randomly subsampling half of the Delta sequences used for the analysis does not substantially change the inferred scaled effective population size.

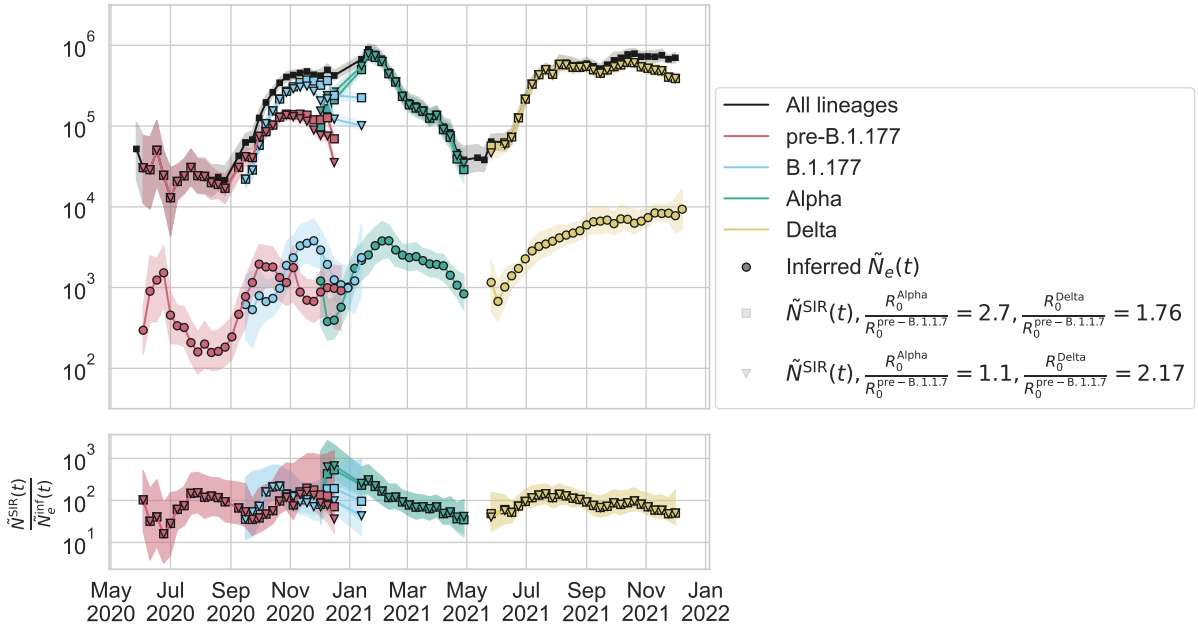

Figure S31: Varying the values of the basic reproduction number within literature ranges ($\frac{R_0^{\mathrm{Alpha}}}{R_0^{\mathrm{pre-B.1.1.7}}} = 1.1-2.7$ [17], $\frac{R_0^{\mathrm{Delta}}}{R_0^{\mathrm{pre-B.1.1.7}}} = 1.76-2.17$ [78]) used for calculation of the SIR model $\tilde{N}_e(t)$ by variant (Methods) does not substantially affect the calculated $\tilde{N}^{\mathrm{SIR}}(t)$.

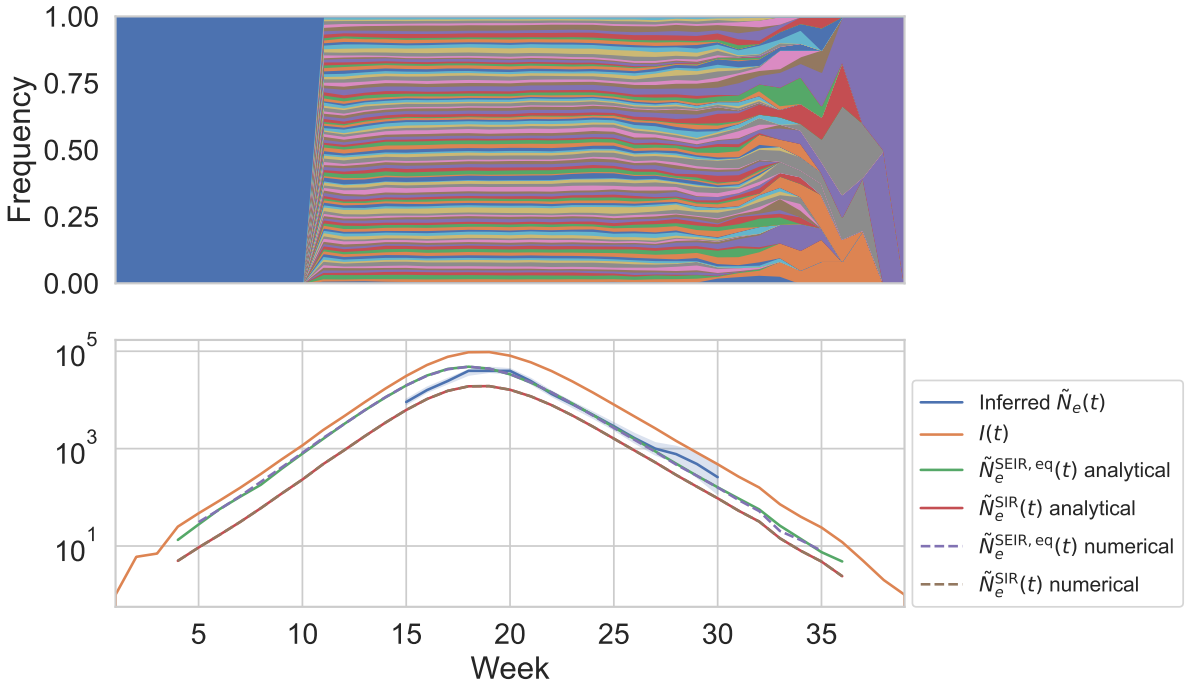

Figure S32: Simulations of stochastic SEIR dynamics without measurement noise, and comparison of the inferred $\tilde{N}_e(t)$ to Equations 1 and 49 when the reported positive individuals include only the infectious individuals. (Top) Muller plot of simulated infectious individuals' lineage trajectories (simulations described in Methods). Infectious individuals are randomly assigned a lineage in week 11, and individuals that they transmit to are infected with the same lineage. The blue lineage before week 11 indicates the infectious individuals that existed before lineages were assigned. (Bottom) Comparison of the inferred $\tilde{N}_e(t)$ using the lineage trajectories shown in the top panel to the number of infectious individuals $I(t)$, Equation 49 (SEIR model $\tilde{N}_e(t)$ at equilibrium), and Equation 1 (SIR model $\tilde{N}_e(t)$) calculated analytically or numerically as described in the Methods. The numerical solutions give the same results as the analytical solutions.

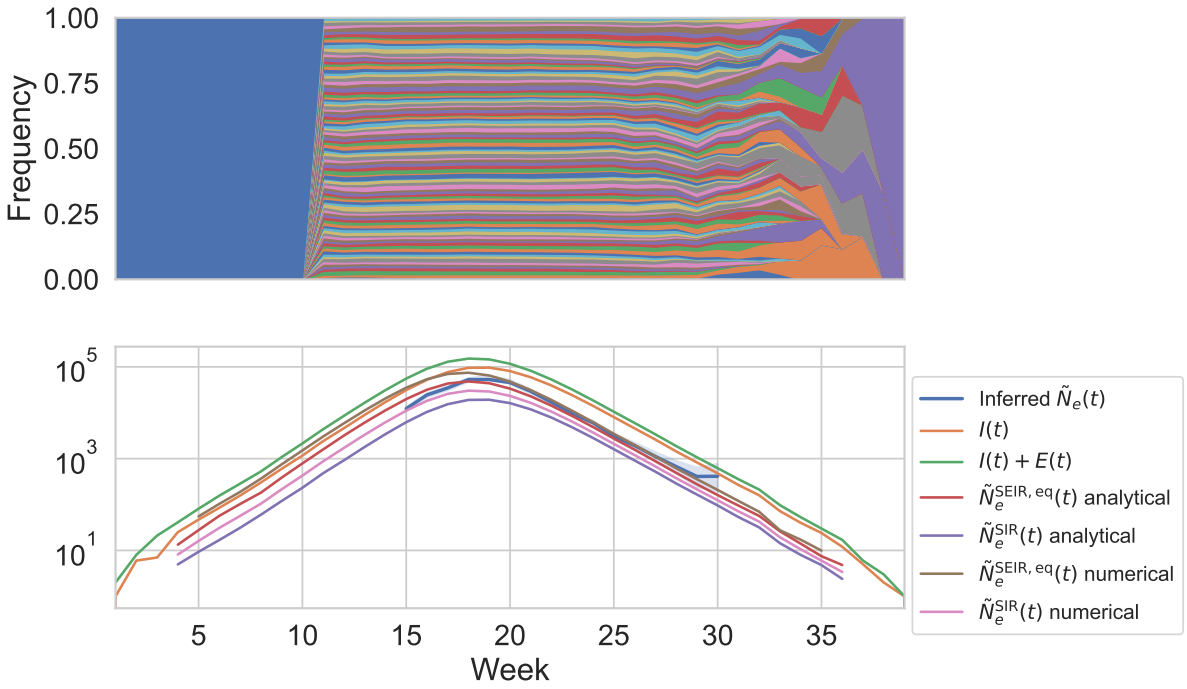

Figure S33: Simulations of stochastic SEIR dynamics without measurement noise, and comparison of the inferred $\tilde{N}_e(t)$ to Equations 1 and 49 when the reported positive individuals include both infectious and exposed individuals. (Top) Muller plot of simulated infectious and exposed individuals' lineage trajectories (simulations described in Methods). Infectious and exposed individuals are randomly assigned a lineage in week 11, and individuals that they transmit to are infected with the same lineage. The blue lineage before week 11 indicates the infectious and exposed individuals that existed before lineages were assigned. (Bottom) Comparison of the inferred $\tilde{N}_e(t)$ using the lineage trajectories shown in the top panel to the number of infectious individuals $I(t)$, the sum of the number of infectious and exposed individuals $I(t)+E(t)$, Equation 49 (SEIR model $\tilde{N}_e(t)$), and Equation 1 (SIR model $\tilde{N}_e(t)$) calculated analytically or numerically as described in the Methods. The numerical solutions give slightly higher $\tilde{N}_e(t)$ as compared with the analytical solutions; however, the numerical solutions to the SEIR and SIR models bound the inferred $\tilde{N}_e(t)$.

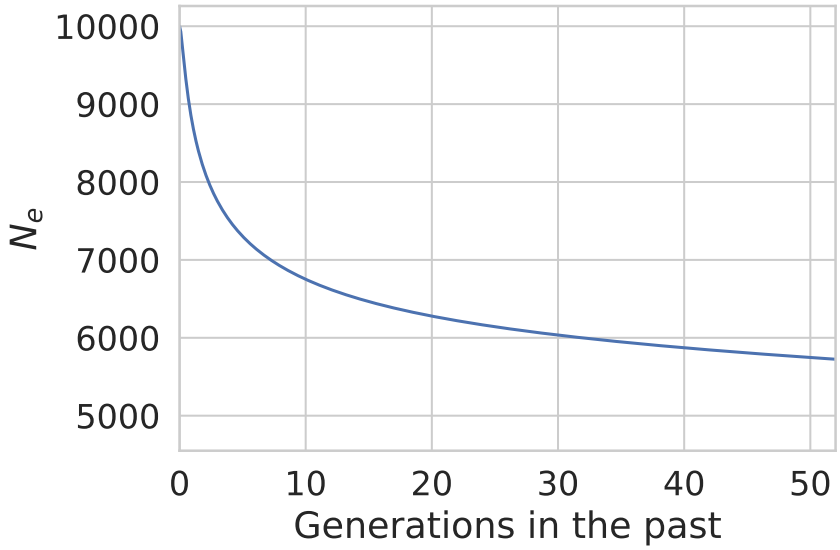

Figure S34: The effect of the empirically estimated distribution of deleterious fitness effects in SARS-CoV-2 [46] on the effective population size using the analytical theory derived in Ref. [87] (Equation 67). In this calculation, the effective population size in the absence of background selection is 10^4, the clock rate is 31 substitutions per year, and the generation time is 5.1 days.